Discovering new alternatives to the standard Higgs boson at the Large Hadron Collider

by

Sandeepan Gupta

A dissertation submitted in partial fulfillment
of the requirements for the degree of
Doctor of Philosophy
(Physics)
in The University of Michigan
2012

Doctoral Committee:

       Professor James D Wells, Chair
       Professor Charles Doering
       Professor Gordon L Kane
       Assistant Professor Junjie Zhu
       Assistant Professor Kathryn Zurek

There is a tingling in the spine, a catch in the voice, a faint sensation, as if a distant memory, of falling from a height. We know we are approaching the greatest of mysteries...

Carl Sagan, Cosmos

To my father, Alok Gupta, but for whose efforts I would never have been a physicist
and my mother, Chhaya Gupta, for her constant love and support.

ACKNOWLEDGEMENTS

I would like to thank, first of all, my two mentors: James D Wells, my thesis adviser, and Christophe Grojean who was my supervisor at CERN. From elucidating theoretical subtleties and advice on making plots to helping me get the big picture in Higgs physics, my mentors have contributed to every aspect of my research outlook, whether conceptual, technical or practical.

My development as a researcher has been deeply influenced by many physicists at Michigan and CERN but especially by conversations with Gia Dvali and Gian Giudice. I would also like to thank my committee members, Charles Doering, Gordon Kane, Junjie Zhu and Kathryn Zurek for their valuable suggestions for improving my thesis. For my different projects I have greatly benefitted from discussions with Aaron Armbuster, Oldrich Kepka, Christophe Royon, Slava Rychkov and Alex Vikman.

I am also indebted to my fellow PhD students at CERN and Michigan many of whom have become much more than colleagues. I thank, in particular, Adish, Adrian, Ahmad, Alessandra, Andrei, Andrea, Dani, Duccio, Ennio, Ionnais, Javi, Julien, Kentaro, Marius, Nishita, Norberto, Somnath, Stefan and Sunghoon. The five years of my PhD were a formative period in my life and the time spent with these friends has been crucial in shaping me as a physicist and as a person. I am also grateful to my brother for his constant encouragement. Finally, I would like to express my special appreciation for Aalo, whose presence made thesis writing an

inspired activity.

TABLE OF CONTENTS

LIST OF FIGURES

LIST OF TABLES

LIST OF APPENDICES

Appendix

CHAPTER I

Introduction

One of the great achievements of modern science is the discovery of the elementary particles that constitute seemingly everything. Laws governing the behavior of these elementary constituents are the laws that underlie all natural phenomena. At present high energy experiments have uncovered laws that are valid up to length scales as small as an attometer (10^{-18} m). Given the complexity and variety of natural phenomena, it is remarkable how simple and elegant these laws are. All the information contained in these laws can be summarized in a single expression,

$$
\mathcal{L} = i \sum_k \bar{\psi}_k \gamma^\mu D_\mu \psi_k - \frac{1}{4} W_I^{\mu\nu} W^{I\ \mu\nu} - \frac{1}{4} B^{\mu\nu} B^{\mu\nu} - \frac{1}{4} G^{\mu\nu} G^{\mu\nu}
$$
$$
\text{(1.1)} \quad + \ m_W^2 W^+ W^- + \frac{m_Z^2}{2} Z^2 - \sum_{ij} m_{ij} \bar{\psi}_i \psi_j + h.c.
$$

where,

$$
W^\pm = \frac{W^1 \pm W^2}{\sqrt{2}},
$$
$$
\text{(1.2)} \quad Z = \frac{-g'B + gW^3}{\sqrt{g^2 + g'^2}}
$$

The equations above give the lagrangian that defines the quantum field theory (QFT) of the known elementary particles[1]. Ignoring the mass terms this is a Yang Mills

---

[1]Note that we have not mentioned gravity because the quantum effects of gravity are negligible at these length scales.

theory with a local SU(3)×SU(2)×U(1) gauge symmetry. The ψ_i are the fermionic matter fields, W^I, B and G are the gauge fields, $D_\mu = \partial_\mu - igT^I W^I_\mu - ig'(Y/2)B_\mu$ is the covariant derivative, the T^I are the SU(2) generators and $Y/2$, the hypercharge, is the charge under the U(1) group. The form of the interactions is completely determined by the gauge symmetry. The matter fields come in three copies or generations. The charge assignments of the matter fields in a generation are fixed by anomaly cancellation requirements.

The mass terms for the vector bosons, $W^\pm$ and Z, and the fermions, however, break the electroweak SU(2)×U(1) invariance. Not only are the masses undesirable from an aesthetic point of view, as we will soon describe, they also lead to serious theoretical problems. The most popular solution to these problems requires the introduction of the yet undiscovered Higgs boson with a mass close to the mass of the weak bosons. While this solution is the one most favored by present experimental data, it is not the only theoretical possibility. This thesis deals with the physics of the Higgs boson and its alternatives and how these different scenarios can be tested at the Large Hadron collider (LHC). In this introductory chapter we will first explain why vector boson masses are problematic and thus motivate the Higgs boson and its alternatives. We will then discuss the latest indirect and direct experimental constraints that favor a light Higgs boson and discuss how the Higgs boson can be detected at the LHC. Finally we will give an outline of the rest of the thesis in the final section.

1.1   The problem of vector boson masses

There are well-know problems associated with high energy scattering amplitudes in a QFT of spin-1 particles. The scattering amplitudes involving the longitudinal

components of vector bosons grow with energy because of the longitudinal polarization vectors,

$$(1.3) \qquad \epsilon_L = \frac{1}{m_W}(k, 0, 0, E) = \frac{p^\mu}{m_W} + \mathcal{O}(m_W/E)$$

that must be included in the amplitude for each external vector boson leg in a scattering process. In the above expression E is the energy and k the magnitude of the momentum of the vector boson. For $E \gg m_W$, the $W_L W_L$ scattering amplitude is,

$$(1.4) \qquad \mathcal{A}(W_L^+ W_L^- \to W_L^+ W_L^-) = \frac{g^2}{4m_W^2}(s + t).$$

Thus the amplitudes have a E^2/m_W^2 dependance. One might naively expect a $E^4/m_W^4 \sim s^2/m_W^4$ dependance because there are four external longitudinal vector bosons. There is however a cancellation in the $\mathcal{O}(E^4/m_W^4)$ term between different diagrams contributing to $\mathcal{A}(W_L W_L \to W_L W_L)$. As we will see in the next section this cancellation is not accidental and is in fact expected. The growth of the above amplitudes violates unitarity which is the requirement that the probability for different possibile final states must add up to unity. This is because, as shown in Appendix F, unitarity requires that each partial wave amplitude a_l must satisfy,

$$(1.5) \qquad |\mathrm{Re}(a_l)| < \frac{1}{2}$$

where,

$$(1.6) \qquad a_l = \frac{1}{32\pi} \int_{-1}^{1} \mathcal{A} \, P_l(\cos\theta) d\cos\theta.$$

In this case from Eq. 1.6 we get,

$$(1.7) \qquad a_0 = \frac{g^2 E^2}{16\pi m_W^2}$$

This implies a violation of unitarity for $\sqrt{s} \geq \Lambda = 1.2$ TeV [4].

Note that care should be taken to interpret the above result. What the above analysis shows is that tree-level amplitudes are unreliable at high energies. This might indicate the presence of new states before these energies are reached or it might mean that higher order and non-perturbative effects can no longer be ignored. In either case it shows the inadequacy of the perturbative description. The fact that higher order corrections become important, also shows that the above tree level number, $\Lambda = 1.2$ TeV, is only a rough estimate and the precise value should not be taken seriously. What the above analysis does show is that, whatever is the mechanism for unitarization of these amplitudes, it is likely to be discovered at the LHC[2] which has a proton-proton center of mass energy equal to 14 TeV.

1.2 The Higgselss Standard Model as a non-linear sigma model

We will now rewrite the theory of the massive vector bosons in a different but equivalent way that makes many of their properties mentioned in the last section more transparent. We introduce some new unphysical degrees of freedom χ_1, χ_2 and χ_3 and define the matrix,

$$(1.8) \qquad \Sigma = \exp(i\chi_i \tau_i / v).$$

where $v = 2m_W/g = 246$ GeV. We now write the mass terms for the gauge bosons and fermions as follows [6],

$$(1.9) \quad \mathcal{L}_m = \frac{v^2}{4}\text{Tr}(D_\mu \Sigma^\dagger D_\mu \Sigma) - \frac{v}{\sqrt{2}}\sum_{ij}\begin{pmatrix} \bar{u}_{Li} & \bar{d}_{Li} \end{pmatrix} \Sigma \begin{pmatrix} y_{ij}^u u_{Rj} \\ y_{ij}^d d_{Rj} \end{pmatrix} + h.c.$$

where we have omitted the lepton masses for simplicity and,

$$(1.10) \qquad D_\mu \Sigma = \partial_\mu \Sigma - ig\frac{\tau^I}{2}W_\mu^I \Sigma + ig'\Sigma \frac{\tau_3}{2}B_\mu$$

---

[2]As shown in Ref. [5], however, some resonances that can unitarize WW scattering amplitudes may escape detection at the LHC.

The matrix Σ transforms under SU(2)$\times$U(1) as,

$$(1.11) \qquad \Sigma \to U_L \Sigma U_Y^\dagger$$

where, $U_L = \exp(i\alpha_i \tau_i/2)$ and $U_R = \exp(i\beta\tau_3/2)$. The equivalence of the lagrangian in Eq. 1.9 and the mass terms in Eq. 1.1 can be made explicit in the unitary gauge where $\Sigma \to 1$. Note that rewriting the mass terms in Eq. 1.1 as in Eq. 1.9 makes the full lagrangian in Eq. 1.1 invariant under the SU(2)$\times$U(1) gauge symmetry.

The introduction of the fields, χ_i, makes many of the properties discusses in the last section transparent. These scalar modes correspond to the longitudinal polarization modes of the W and Z. Thus we can now clearly focus on the problematic modes by studying the behavior of the χ_i. The above statement can be elevated to a theorem, the so-called equivalence theorem, which says that the absorption and emission amplitudes of the scalars χ_i is equal to the absorption and emission amplitudes of the corresponding gauge bosons up to $\mathcal{O}(m_V^2/s)$ terms where $m_V = m_W$, m_Z [7].

Using the equivalence theorem the E^2/m_W^2 dependance of the $W_L^+ W_L^- \to W_L^+ W_L^-$ amplitude discussed in the last section becomes clear. The $\chi^+\chi^- \to \chi^+\chi^-$ amplitude gets a tree level contribution from the $\chi^+\chi^-\chi^+\chi^-$ vertex that can be obtained by expanding the exponential in Eq. 1.9. Clearly we expect a E^2/m_W^2 dependance for the amplitude because the $(v^2/4)\text{Tr}(D_\mu\Sigma D_\mu\Sigma)$ term has two derivatives hence by the equivalence theorem,

$$(1.12) \qquad \mathcal{A}(W_L^+ W_L^- \to W_L^+ W_L^-) = \mathcal{A}(\chi^+\chi^- \to \chi^+\chi^-) + \mathcal{O}(m_W^2/E^2) \sim \frac{E^2}{v^2}.$$

Thus in this approach we easily obtain the E^2/m_W^2 dependance and no seemingly miraculous cancellations occur.

The theory described by the lagrangian in Eq. 1.9 is clearly non-renormalizable as the exponential when expanded gives gives higher dimension terms. Thus the growth

of the amplitude we found in Section 1.1 is no different from the usual growth of amplitudes due to non-renormalizable operators. To find the cut-off of the above theory note that the amplitude will also get a loop contribution because of the diagram $\chi^+\chi^- \to (\chi^+\chi^-)_{loop} \to \chi^+\chi^-$. The loop contribution can be estimated to be of order,

$$(1.13) \qquad \mathcal{A}(\chi^+\chi^- \to \chi^+\chi^-)_{tree} \sim \frac{1}{16\pi^2}\frac{E^4}{v^4}.$$

Thus the loop contribution becomes of the order of the tree level contribution for,

$$(1.14) \qquad E = \Lambda \approx 4\pi v.$$

Thus at this scale the higher order contributions can no longer be ignored. This estimate gives us a cut-off $\Lambda \approx 4\pi v = 3.1$ TeV, which should be compared with the value $\Lambda \approx 1.2$ TeV in the previous section. As we stated then these are only rough estimates, i.e. different ways of estimating the cut-off would give us different numbers, but all would be within the same order of magnitude.

To summarize, we introduced a redundancy into our massive gauge boson lagrangian by introducing the unphysical scalar degrees of freedom, χ_i. We also discovered that with the introduction of these scalar fields, the whole lagrangian in Eq. 1.1, including the mass terms, can be rewritten such that it is invariant under the SU(2)×U(1) gauge symmetry. Using this symmetry the unphysical scalar modes can be gauged away. We thus found that the problem with the high energy amplitudes in Section 1.1 arises out of the non-renormalizability of the underlying theory described by Eq. 1.1. In the next section we discuss possible UV-completions of the theory described by Eq. 1.1.

1.3   The Higgs mechanism and the hierarchy problem

We will see in this section that the scalar degrees of freedom, χ_i, from the last section can be identified with the goldstone bosons that arise upon spontaneous breaking of the SU(2)×U(1) invariance. If the SU(2)×U(1) were a global symmetry these goldstone bosons would be massless modes in accordance with the equivalence theorem. The fact that the invariance is a local symmetry, however, means that the χ_i can be gauged away, and absorbed as longitudinal modes by the gauge bosons W and Z which now become massive. We will see that this gives us a UV completion of the theory described by the lagrangian in Eq. 1.1, that has been discussed in Sections 1.1, 1.2.

To show this in detail we replace the mass terms in Eq. 1.1 with the Higgs lagrangian. We introduce the Higgs field Φ, an SU(2) doublet having hypercharge $Y = 1$, and has the lagrangian,

$$(1.15) \qquad \mathcal{L}_{Higgs} = (D_\mu \Phi)^\dagger D^\mu \Phi - V(\Phi)$$

and a potential,

$$(1.16) \qquad V(\Phi) = -\mu^2 \Phi^\dagger \Phi + \lambda (\Phi^\dagger \Phi)^2.$$

With the mass terms in Eq. 1.1 replaced by the Higgs lagrangian we get the lagrangian of the Standard Model (SM) which is SU(2)×U(1) invariant. The Higgs field, however, gets a vacuum expectation value (VEV) which breaks this invariance. The potential above has the shape of a mexican hat and after electroweak symmetry breaking (EWSB) the Higgs doublet can be parametrized as,

$$(1.17) \qquad \Phi = \exp(i\chi_i \tau_i / v) \begin{pmatrix} 0 \\ (v+H)/\sqrt{2} \end{pmatrix}$$

where $v = \sqrt{-\mu^2/\lambda}$ is the VEV. The prefactor, $\exp(i\chi_i\tau_i/v)$, can be identified with the matrix Σ defined in Eq. 1.8. We can make a gauge transformation and set $\chi_i = 0$. Note that this step would not be possible if SU(2)×U(1) were a global symmetry and the χ_i would remain in the spectrum as massless modes. Also notice that the U(1)$_{em}$ group having the generator,

$$(1.18) \qquad Q = T_3 + \frac{Y}{2}$$

remains unbroken, as one can explicitly check that the vacuum in Eq. 1.17 does not break this group. The radial mode H, is the Higgs boson and it gets a mass,

$$(1.19) \qquad m_H^2 = 2\lambda v^2.$$

As a consequence of the Higgs vacuum expectation value (VEV) the Higgs kinetic term gives masses to the gauge bosons as follows,

$$
\begin{aligned}
(D_\mu\Phi)^\dagger D^\mu\Phi \;\to\; & \frac{1}{8}\left|\begin{pmatrix} g'B + gW^3 & g(W^1 - iW^2) \\ g(W^1 + iW^2) & g'B - gW^3 \end{pmatrix}\begin{pmatrix} 0 \\ v \end{pmatrix}\right|^2 \\
(1.20) \qquad = \; & \frac{g^2v^2}{4}W^+W^- + \frac{(g^2 + g'^2)v^2/4}{2}Z^2.
\end{aligned}
$$

Comparing with Eq. 1.1 we find,

$$(1.21) \qquad m_W = \frac{gv}{2} \text{ and } m_Z = \frac{\sqrt{g^2 + g'^2}}{2}v.$$

The linear combination,

$$(1.22) \qquad A = \frac{gB + g'W^3}{\sqrt{g^2 + g'^2}}$$

is the photon and it gets no mass. This is the gauge boson of the unbroken U(1)$_{em}$ gauge group.

We will now see how the theory described above is a satisfactory UV completion of theory described by Eq. 1.1. Compared to the Sections 1.1, 1.2 we now have an

additional degree of freedom, the Higgs boson H. In the limit of heavy Higgs mass, the Higgs boson decouples and we obtain exactly the theory described in Section 1.1. It can be shown explicitly that the Higgs contribution exactly cancels the growth of $W_L^+ W_L^- \to W_L^+ W_L^-$ scattering. Instead of evaluating all the diagrams we will use the equivalence theorem again but we will now parametrize the goldstone bosons in a different way,

$$(1.23) \qquad \Phi = \frac{1}{\sqrt{2}} \begin{pmatrix} \phi_1 + i\phi_2 \\ (v + H) + i\phi_3 \end{pmatrix}.$$

In this linear parametrization, $\phi^\pm = \frac{1}{\sqrt{2}}(\phi_1 \pm i\phi_2)$ correspond to the goldstone bosons absorbed by the longitudinal $W^\pm$ bosons. Thus according to the equivalence theorem in order to compute the $W_L^+ W_L^- \to W_L^+ W_L^-$ scattering amplitude we must compute the $\phi^+ \phi^- \to \phi^+ \phi^-$ amplitude. There are two contributions to the amplitude: (1) from the contact interaction $\phi^+ \phi^- \phi^+ \phi^-$ and (2) the Higgs mediated process $\phi^+ \phi^- \to H \to \phi^+ \phi^-$ where the vertex $H\phi^+\phi^-$ comes into play. Both the vertices involved are derived from the quartic term $\lambda(\Phi^\dagger \Phi)^2$. A simple evaluation gives [4],

$$(1.24) \qquad \mathcal{A}(W_L^+ W_L^- \to W_L^+ W_L^-) \approx \mathcal{A}(\phi^+ \phi^- \to \phi^+ \phi^-) \approx -4\lambda = -\frac{2m_H^2}{v^2}.$$

in the limit $s \gg m_h^2$. Using the constraint from Eq. F.3 we obtain in this case,

$$(1.25) \qquad m_H < 870 \text{ GeV}$$

A more stringent bound of 710 GeV [8,9] can be derived by considering the $W_L^+ W_L^- \to Z_L Z_L$ process. Again the order of magnitude and not the precise value of these numbers is important. Thus the amplitude does not grow with energy, and provided the Higgs boson is light, we have a consistent QFT up to arbitrarily high energies. For a heavy Higgs the theory would become strongly coupled. This is not surprising

as a heavy Higgs means a large quartic coupling, $\lambda \gg 1$, which makes the theory strongly coupled[3].

Thus we see the introduction of a light Higgs is an economical and elegant way to unitarize $W_L W_L$ scattering. There is, however, still a conceptual problem, the so-called hierarchy problem. There are many reasons to extend the SM like the presence of dark matter, the observed matter antimatter symmetry of the universe, and the most unavoidable reason of all: presence of gravity, which becomes a strong force at the Planck scale. It is hard to embed the SM with a light Higgs in a more fundamental theory with higher mass scales. This is because the Higgs mass term being a relevant operator would be sensitive to these high energy thresholds unless it is protected by a symmetry. Let us consider the case where the Planck scale M_{pl} is the cut-off of the SM. A light Higgs can be obtained only if there is a cancellation between the bare Higgs mass $m_h(M_{pl})$ and the Planck scale quantum corrections,

$$(1.26) \qquad m^2_{H\ phy} = m^2_H(M_{pl}) + \sum_i c_i M^2_{pl}.$$

Thus it is natural to have $m^2_{H\ phy} \approx M^2_{pl}$ and to obtain a light Higgs with mass $m^2_{H\ phy} \approx m^2_W$ a fine-tuning of order m^2_W/M^2_{pl} is required. The most popular solution to this issue is the introduction of Supersymmetry (SUSY) which protects scalar masses. SUSY relates the scalars to chiral fermions. As the masses of chiral fermions are protected by chiral symmetry even the scalar masses in SUSY are protected.

While, the introduction of a light Higgs boson is the most economical way to unitarize $W_L W_L$ scattering it is not the only way. There are theories called Technicolor models that have been developed in analogy with Quantum Chromodynamics

---

[3]Note that even lighter Higgs masses indicate the presence of a strong sector. This is because even if the Higgs quartic coupling is perturbative at the scale m_H it runs to larger values at higher energies and thus the theory becomes strongly coupled at higher energy scales. For $m_H \approx 400$ GeV, for instance, the SM becomes strongly coupled at a scale $\Lambda \approx 10$ TeV [10]. Even lighter Higgs bosons can emerge from a strong sector, if there is a symmetry protecting their mass from corrections of the order of the strong scale. One such possibility is that the Higgs boson is a pseudo Goldstone boson of an approximate global symmetry of the strong sector [6].

(QCD). In QCD pions are pseudo goldstone bosons of chiral symmetry breaking. Low energy pion -pion scattering is also governed by a lagrangian similar to Eq. 1.9 with $\chi_i \to \pi_i$ and $v \to f$, the pion decay constant. Thus even in this case there is a violation of perturbative unitarity near the cut-off $4\pi f$. There is however, no scalar resonance analogous to the Higgs in this case. Pion-pion scattering is unitarized by the exchange of an infinite series of resonances. In Technicolor models EWSB takes place when a scalar condensate of techniquarks gets a VEV. In analogy with pion-pion scattering no Higgs boson is required; instead resonances are expected to be produced in longitudinal WW scattering.

In strong EWSB models there is no hierarchy problem as there is no elementary Higgs boson. Furthermore, the electroweak scale is generated dynamically in such theories. Just as the QCD scale, $\Lambda_{QCD} \approx 1$ GeV, is the scale at which the running QCD coupling becomes large, in theories with strong EWSB the electroweak scale is the scale at which the coupling of the underlying theory becomes large.

1.4 Experimental searches and the case for a light Higgs

In the previous sections we have seen that there are two different paradigms for electroweak symmetry breaking (EWSB): higgsless or heavy Higgs scenarios with strongly coupled EWSB, and the perturbative light Higgs scenario. Theoretically, each scenario is plausible but experimental data seems to favor the light Higgs scenario. In this section we will review these experimental results and discuss the ongoing LHC searches for the Higgs.

1.4.1 Experimental constraints on the Higgs mass

The most important constraints on the Higgs boson come from direct searches at the LEP, Tevatron and LHC. For low Higgs masses, the $ee \to ZH$ process at LEP-2

is the most sensitive process. For a SM Higgs this process puts constraint [11],

$$(1.27) \qquad m_H > 114.4 \text{ GeV}$$

at 95% confidence level (CL). The combined Tevatron data puts the following constraint at 95% CL [12],

$$108 \text{ GeV} < \quad m_H \quad < 147 \text{ GeV}$$

$$(1.28) \qquad \text{or} \quad m_H \quad > 179 \text{ GeV}.$$

The lower limit comes mainly from the associated production processes, WH/ZH followed by the decay $H \to bb$, and the upper bound comes mainly from $H \to WW$ the decay channel.

The strongest constraints at least for high masses comes from the latest LHC searches. We will discuss the LHC searches in more detail in the next section but we summarize the constraints here. The Higgs boson mass ranges from 110-117.5 GeV, 118.5-122.5 GeV, and 129 GeV-539 GeV are excluded at 95 % CL by the ATLAS collaboration [13]. The CMS collaboration excludes the mass range 127.5-600 GeV at 95 % CL [14]. Together these constraints imply for the allowed range of Higgs masses,

$$117.5 \text{ GeV} < \quad m_H \quad < 118.5 \text{ GeV}$$

$$122.5 \text{ GeV} < \quad m_H \quad < 127.5 \text{ GeV}$$

$$(1.29) \qquad \text{or} \quad m_H \quad > 600 \text{ GeV}.$$

All three experiments also see very interesting excesses in their Higgs searches. The Tevatron finds a 2.2 sigma excess that can be interpreted to be coming from a Higgs boson with mass in the range in the 115-135 GeV mass range [12]. An excess of events is observed around $m_H \sim 126$ GeV with a local significance of 2.5 standard

deviations by the ATLAS collaboration [13] and an excess, with a local significance of 2.8 standard deviations, is observed for $m_H \sim 125$ GeV by CMS [14].

The above results seem to favor either a Higgs in the window 115.5 GeV $<$ $m_H < 127$ GeV, or a higgsless/heavy Higgs scenario which would necessarily point to strongly coupled EWSB. There is, however, indirect evidence that favors the former possibility over the latter. The LEP-2 experiment carried out highly precise measurements of observables like the W mass, the weak mixing angle and the partial decay width of the Z boson to leptons. These measurements were sensitive to quantum effects from scales much higher than those LEP-2 could directly probe, and are thus very useful in constraining new physics scenarios. In particular, new states that contribute to vector boson self energies through loops, also change the theoretical predictions for the above observables. The Higgs boson is an example of a new state that modifies vector boson self energies and thus the theoretical values of the electroweak observables are functions of the Higgs mass. To find the Higgs mass value preferred by these measurements a χ^2-fit can be performed where,

$$(1.30) \qquad \chi^2 = \sum_i \frac{(\mathcal{O}_i^{theory}(m_H, ...) - \mathcal{O}_i^{expt})^2}{(\Delta \mathcal{O}_i^{expt})^2}$$

Here $\mathcal{O}_i^{expt}$ is the experimentally measured value of the observable, $\Delta \mathcal{O}_i^{expt}$ is the experimental error and $\mathcal{O}_i^{theory}(m_H, ...)$ is the theory prediction which is a function of the Higgs mass m_H and other known parameters. The best fit value for the Higgs mass ignoring direct search constraints is [15],

$$(1.31) \qquad m_H^{best} = 94^{+25[+59]}_{-22[-41]} \text{ GeV},$$

where the subscript and superscript are the one and two sigma deviations (the value within square brackets being the two sigma deviation) from the central value. Note that the above constraint assumes a SM Higgs. In BSM scenarios the Higgs mass

can be much higher [16].

1.4.2 Higgs searches at the LHC

Now we shall consider in more detail the Higgs searches at the LHC. There are four production mechanisms for the Higgs at the LHC: (i) gluon fusion, i.e. $gg \to H$, (ii)vector boson fusion (VBF), i.e. $qq \to Hqq$, (iii) associated production with gauge bosons, i.e. $qq \to WH, ZH$ and (iv) associated production with a top pair, i.e $qq \to t\bar{t}H$. The last production channel ($t\bar{t}H$) is kinematically suppressed at the 7 TeV LHC. The gluon fusion process is by far the most important process with cross sections an order of magnitude higher than the cross-section of other channels. The ggH coupling in the standard model gets its dominant contribution from top loops. Though VBF and associated production channels (WH/ZH) have a smaller cross-section, these are also very important. This is because one can imagine a situation where the Higgs coupling to the top quark, or fermions in general, is suppressed. In this case VBF and associated production would be the primary Higgs production channels. The associated production channels (WH/ZH) are also important because with high luminosity they can access the predominant decay channel of the Higgs at low masses, the $H \to bb$ channel, through the process $qq \to WH(bb)/ZH(bb)$.

Now we come to the important decay channels. The decay channels being studied by CMS and ATLAS are $H \to \gamma\gamma$, $H \to \tau\tau$, $WH(bb)/ZH(bb)$, $H \to ZZ \to 4l$, $H \to ZZ \to 2l2\nu$, $H \to ZZ \to 2l2b$ and $H \to WW \to l\nu l\nu$. We now discuss the three most important channels, the $H \to ZZ \to 2l2\nu$ channel, the $H \to \gamma\gamma$ channel and the $H \to \gamma\gamma$ channel.

The $H \to WW \to l\nu l\nu$ channel is the most sensitive channel for exclusion in the important mass range $125 - 190$ GeV. This channel is, however, not the ideal for discovery of the Higgs boson. This is because, the presence of missing energy means

that this channel has very poor mass resolution. The only sensitivity of the search
to the Higgs mass comes from studying the transverse mass (m_T) distribution. The
transverse mass, m_T, is defined by [17],

$$(1.32) \qquad\qquad m_T = \sqrt{(E_T^{ll} + E_T^{miss})^2 - (\mathbf{P}_T^{ll} + E_T^{miss})^2}$$

where the transverse momentum of the lepton pair, $\mathbf{P}_T^{ll} = \mathbf{P}_T^{l1} + \mathbf{P}_T^{l2}$, $E_T^{ll} = \sqrt{P_T^{ll\ 2} + m_{ll}^2}$,
E_T^{miss} is the missing transverse energy and m_{ll} is the invariant mass of the leptons.
This kinematic variable is important because for a Higgs decaying to $l\nu l\nu$, m_T is
always less than the Higgs mass.

The other important channel, especially for high mass ranges, is the $H \to ZZ \to$
$4l$ channel. While the cross-section for this channel is not so high, this is a particularly
clean channel with low background. Thus even the presence (absence) of a few excess
events can lead to a discovery (exclusion) with high significance (confidence level).
Unlike the $H \to WW \to l\nu l\nu$ channel, this channel has good mass resolution. The
high Higgs mass exclusion in Eq. 1.29 is mainly due to the the $H \to WW \to l\nu l\nu$
and $H \to ZZ \to 4l$ channels.

Finally we discuss the $H \to \gamma\gamma$ channel which is the most important discovery
channel for a low mass Higgs boson in the region not yet excluded by experiments.
The $H\gamma\gamma$ coupling in the SM gets contributions from W and fermion (mainly top)
loops with opposite signs, the W loop having the larger contribution. A Higgs with
reduced coupling to fermions is thus expected to have a higher cross-section in this
channel. This channel has a high mass resolution, about 1.1 % of the Higgs mass. As
we mentioned in Section 1.4.1 there are hints of a Higgs boson in the 123-127 GeV
mass range in both ATLAS and CMS data. The dominant contribution to these
excesses is from the $H \to \gamma\gamma$ channel.

1.5   Thesis outline

As we have discussed in Sections 1.1, 1.2 of this introduction, electroweak symmetry breaking (EWSB) requires only the goldstone modes of the Higgs doublet field and not the radial mode, the Higgs boson. The quantum field theory of the goldstone modes with the Higgs boson decoupled is, however, non-renormalizable and violates perturbative unitarity near its cut-off, around the TeV scale, where it becomes strongly coupled. The usual approach in such a situation is to find a Wilsonian UV completion, like Technicolor, with no fundamental Higgs boson and thus no hierarchy problem.

In Chapter II we describe an alternative, non-Wilsonian approach called classicalization. This approach is inspired by gravity where it can be argued that perturbative unitarity in $2 \rightarrow 2$ scattering amplitudes is never violated at transplanckian energies, because of formation of classical black holes that decay to many (and not two) particles. This leads to a suppression of $2 \rightarrow 2$ scattering amplitudes. It has been proposed by Dvali et al. [18] that similar classical configurations, called classicalons, can be produced in non-gravitational theories also, if a bosonic field is sourced by derivatively coupled operators that grow with energy. One possibility for this bosonic field is the longitudinal scalar modes of the W/Z fields. We have already seen in Section 1.2, 1.3 that interactions involving these modes grow with energy. It has thus been proposed that longitudinal $WW(ZZ)$ scattering can be unitarized by the formation of classical configurations that decay to multiple Ws and Zs. In order to make collider predictions for such a scenario one needs to have a way to estimate the number of W/Zs that would be produced at a certain energy. In Chapter II we will compute the final decay multiplicity of classicalons by arguing that, like black

holes, they have analogs of thermodynamic properties. By labeling the microstates of a classicalon by the set of four momenta of the decaying particles, we will carry out a statistical mechanical analysis of classicalon decays. We will thus be able to compute the number of decay products and then extract concrete collider predictions for classicalization. We will see that at the LHC classicalons can be produced in the Vector Boson Fusion channel and the collider signals are spectacular multi-W/Z final states that lead to leptons, missing energy and such a high multiplicity of jets that there is virtually no background. This chapter is based on an article written in collaboration with Christophe Grojean that has been submitted to Journal of High Energy Physics [19].

An alternative to such non-perturbative physics is of course to have a light, weakly coupled, Higgs sector that unitarizes longitudinal WW scattering at energies much lower than the perturbative unitarity bound. As we discussed in Section 1.4.1, such a scenario is, in fact, favored by the high precision LEP-2 measurements of electroweak observables. The question then is: Is the Higgs sector realized as the most minimal possibility, a single doublet as in the Standard Model (SM), or is it more complicated? Minimality after all is hardly a convincing requirement for a low energy theory at the TeV scale. Also, non minimal Higgs sectors are generic in many motivated extensions of the SM.

In Chapter III we consider the possibility of adding new Higgs doublets in both supersymmetric and non supersymmetric scenarios. In the supersymmetric case anomaly cancellation requirements dictate that we add these Higgs in generations of up and down pairs. Flavor constraints can be satisfied if the new doublets do not couple to fermions which can be achieved by giving the new doublets a charge under a discrete symmetry. The discrete symmetry is, however, spontaneously broken which

causes problems with flavor constraints at the loop level, in particular the charged Higgs contribution to the $b \rightarrow s\gamma$ process can be large. We will show that a simple way to avoid all the constraints is if the new doublets get small vacuum expectation values. This would, however, suppress the ggH and VVH ($V = W^{+/-}, Z$) couplings making the discovery of these new states difficult at colliders. The ZAh coupling (A being the pseudoscalar and h being the non SM-like CP-even Higgs boson) is however not suppressed even in this limit, so that, as we will show that a process like $pp \rightarrow Z \rightarrow A(Zh)h \rightarrow Z + 4b$ would be a possible signature. This chapter is based on an article written in collaboration with James D Wells that has been published in the journal, Physical Review D [20].

In Chapter IV we consider a model with a singlet scalar added to the SM. In this case we get two Higgs bosons which share the SM couplings according to the strength of their wave-function overlap. The most sensitive search channel for masses in the range 130-180 GeV is the $H \rightarrow WW \rightarrow l\nu l\nu$ channel. As discussed in Section 1.4.2, because of the presence of missing energy in this channel, the mass resolution is poor and it is hard to distinguish two such Higgs states if the masses are close to each other. We will see that in such a scenario it becomes crucial to analyze the shape of the significance vs m_H profile and that deviations in the shape may be the first sign of the second Higgs. The results of this study were published in Physics letters B with James D Wells as a co-author [21].

One may also take the view that a generic non-minimal Higgs sector violates existing constraints in general. Not only are there problems with flavor constraints, if one is not careful in choosing the parameters of the scalar potential, it might lead to other complications like the photon getting a mass (discussed in Chapter III). A single light Higgs doublet, as in the SM, is not only the most minimal option but

also the easiest way to satisfy all existing constraints. In such a scenario, flavor and precision constraints favor a mass gap between the light Higgs doublet and the new physics that stabilizes its mass. A general model independent description can be achieved in this case by supplementing the SM with higher dimensional operators suppressed by the scale of new physics. In Chapter V we will use such an approach to study quartic couplings involving the neutral gauge bosons, i.e. the photon and the Z boson, by listing all possible operators contributing to these couplings both in the light Higgs case and the higgsless case where electroweak symmetry is non-linearly realized. A particularly clean way of experimentally probing these couplings is through the diffractive photon fusion process, $pp(\gamma\gamma \rightarrow \gamma\gamma/ZZ)pp$, where the intact protons in the final state can be detected by forward proton detectors that would be installed by ATLAS and CMS. While measurements like these would not lead to the first discovery of new physics, many such complementary measurements would be necessary for understanding the nature and details of the new physics discovered. This study was published in the journal Physical Review D [22].

The text of each chapter is mainly that of the corresponding research publication cited above. Although some publications were written in collaboration with my co-authors, my contributions to the technical work were always primary, and my contributions to the writing were substantial and infused throughout the entire text of the articles. It is for this reason the text of the chapters closely resemble that of the research publications.

CHAPTER II

Classicalization, a Higgsless alternative

2.1 Introduction and motivation

As explained in Chapter I, to find out how longitudinal WW-scattering is unitarized is the *raison d'être* for the LHC. If the LHC keeps delivering data at the present rate we may know the ultimate fate of the most popular candidate, the Higgs boson, very soon. With the 2012 LHC data, the SM Higgs would be either discovered or conclusively excluded. As we discussed in Chapter I an elementary Higgs boson has its own problems if it exists as one must then explain the hierarchy between its mass and the cut-off scale. This suggests the existence of new TeV-scale physics even if the Higgs boson exists. Thus, whether or not a Higgs exists, the standard argument goes that that a Wisonian UV completion is required with new states needing to be integrated in at the TeV scale.

A non-Wilsonian alternative has been proposed in Ref. [18]. For this the authors have taken inspiration from the other major problem of high energy physics, that of finding a UV-completion for quantum gravity. It has been argued in Refs. [18,23–26] that in transplanckian 2→2 scattering in gravity there is no violation of perturbative unitarity because of black hole formation. Black holes are classical objects that decay to many particles and decays to two particles are suppressed leading to a

suppression of the 2→2 scattering amplitudes. As we go to higher energies we get larger black holes and the amplitudes are even more suppressed. In Refs. [18,23–26] it has been proposed that formation of classical objects, called classicalons, is possible in high energy scattering also in non-gravitational theories. This happens if there is a bosonic field (the classicalizer field) which is sourced by derivatively coupled operators that grow with energy. At high enough center of mass energy $\sqrt{\hat{s}}$, the source leads to formation of classical configurations of the classicalizer field. As the classicalon would in general decay into many particles, the usual problem of perturbative unitarity violation in 2→2 scattering in non-renormalizable theories is thus avoided without a usual Wilsonian UV completion.

In the case of WW-scattering the bosonic field can be the longitudinal goldstone modes of the W. As is well known interactions involving these modes grow with energy so that an appropriate non-linear interaction can be used for self-sourcing these modes. This way of unitarizing WW-scattering is thus arguably even more economical than having a single Higgs. As we will discuss in more detail later, around the classicalization scale the classicalons should be thought of as a tower of quantum resonances and only at energies much higher than this scale do they become truly classical. Thus, whereas around the classicalization scale, such a theory would resemble standard Wilsonian UV completions, like technicolor, with resonances appearing at this scale, a theory with classicalization would be very different in the deep UV. For instance, the inclusive cross-section in classicalizing theories would grow geometrically as the squared classicalon radius, r_*^2, at energies above the classicalization scale, unlike any Wilsonian UV-completion where the cross-section eventually decreases with energy. Classicalization can have an application even if the Higgs boson exists provided appropriate classicalizing interactions are also present. Classical con-

figurations of the Higgs field itself, called Higgsions, can be sourced by the energy of the other SM particles in high energy scattering. The classicalization scale where Higgsion formation starts would then become the scale at which the loop contributions to the Higgs mass get screened, thus solving the hierarchy problem. The collider signals for these models would be the spectacular production of multiple Ws and Zs in the first case of goldstone classicalization and multi-Higgs final states from Higgsion decays in the second case.

In this work we want to tackle the important question of classicalon decays. We want to address questions like: How many particles does a classicalon decay to? What is the energy distribution of these decay products? These questions are important for understanding both the theory and phenomenology of classicalons. From the theoretical point of view, the most important feature for unitarization of the amplitudes is that a classicalon decays, in general, to many particles and decays to a few particles are suppressed. Thus understanding classicalon decays is very important. From the experimental point of view this is the important ingredient that will allow us to make LHC predictions. This is because while the production cross-section can be estimated from geometric arguments to be πr_*^2, a collider analysis is impossible without knowledge of the multiplicity of the classicalon decay products. We will argue, as was already pointed out in Ref. [25], that classicalons, like black holes, have properties analogous to entropy and temperature and they decay thermally. This will give us completely model independent predictions about how classicalons should decay. Before giving the broad argument that tells us why classicalons should have thermodynamic properties we will briefly describe how classicalization takes place.

We take the simple example of a massless scalar theory with a single non-linear,

non-renormalizable interaction,

$$(2.1) \qquad \mathcal{L} = \partial_\mu \phi \partial^\mu \phi + \frac{(\partial_\mu \phi \partial^\mu \phi)^2}{M_*^4}.$$

A non-linear interaction of a similar form will be used for classicalization of longitudinal Ws and Zs later. We know that the non-renormalizable term $(\partial_\mu \phi \partial^\mu \phi)^2 / M_*^4$ above would become important at length scales smaller than the quantum length cut-off, $L_* = 1/M_*$. This term can actually become important at even larger length scales, as shown in Refs. [18, 23], if ϕ takes a large classical value. An analysis in Ref. [23] shows that this is precisely what happens in a scattering process with initial energy bigger than the cut off, i.e. $\sqrt{\hat{s}} > M_*$.[1] The authors solve classical equations of motion to show that if we start with free spherical wave-packet ϕ_0 there would be a correction due to the non-linear term,

$$(2.2) \qquad \phi = \phi_0 + \phi_1$$

that becomes important (i.e $\phi_1 \sim \phi_0$) at a length scale,

$$(2.3) \qquad r_* = \frac{\sqrt{\hat{s}}}{M_*^{1+\alpha}}^\alpha$$

where α (always ≤ 1) is a positive number that depends on the choice of non-linear term, and is $1/3$ in this example. We can see from the expression above that for $\sqrt{\hat{s}} > M_*$ we get $r_* > L_* = 1/M_*$ so that r_* is in fact a classical length. At distances smaller than r_* the non-linear term becomes important leading to a formation of a classical configuration of radius r_*. As is clear from Eq.(2.3) with increasing energy the source due to the non-linear term becomes bigger and bigger in magnitude and the radius r_* of the classical object increases. This means that with higher energy we do not probe shorter distances in these theories. Black holes are seen as a special

---

[1]For recent work on the dynamics of classicalization see Refs. [27, 28].
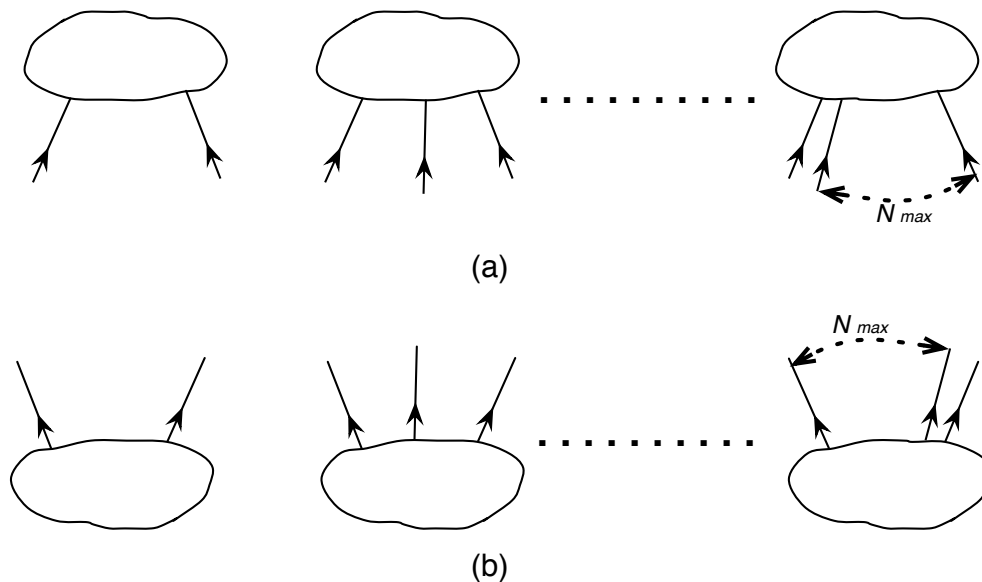
Figure 2.1: (a) Different ways of forming classicalons. Any scattering process with 2,3 ... N initial particles would form a classicalon if the total energy of these particles. $\sqrt{\hat{s}}$, is larger than M_*. (b) We show the time reverse of the processes shown in Fig. 1 (a). By time reversal symmetry, all these processes should also be allowed decays.

case of classicalization where r_* is the Schwarzschild radius, M_* is M_{pl}, the planck mass, and $\alpha = 1$. As shown in Ref. [18] the phenomenon is insensitive to higher order terms in the Lagrangian as these operators give a smaller r_*.

We will now motivate why classicalons must have analogs of thermodynamic properties. One way to see how an effective notion of entropy can arise for a classicalon is by noting that there are many ways of forming a classicalon. Any scattering process with 2,3 ... N initial particles shown in Fig. 2.1(a) would form a classicalon if the total energy of these particles, $\sqrt{\hat{s}}$, is larger than M_*. There is, however, an upper limit on the number of initial particles. This is because we want the wavelength of the particles λ to be smaller than r_*, so that the energy of the particles can be localized within the classicalon radius. Assuming massless quanta, the energy of each particle, $1/\lambda$, must be then at least $1/r_*$. This puts an upper bound on the number

N in Fig. 2.1(a) which is given by,

$$(2.4) \qquad\qquad N_{max} \sim M/(1/r_*) \sim Mr_*.$$

where M is the mass of the classicalon. The only restriction on the initial state is the conservation of energy and momentum and ensuring that all the energy of the particles is localized inside the radius r_*. We expect from combinatorics that there would be many more ways of distributing the required energy among many particles than among a few particles, implying that there should be many more ways of forming a classicalon with many particles in the initial state than with a few particles. Assuming classical time reversal symmetry $(t \to -t)$ we can now argue that the time reverse of each of the possible processes shown in Fig. 2.1(a) is an allowed decay as shown in Fig. 2.1(b). Thus it follows that a classicalon would in general decay to many particles just because of combinatorics. It is also true, however, that just as a classicalon can be formed from two initial particles it can also decay to only two particles but this would be combinatorially suppressed.

In this chapter we will find a quantitative formulation of the above picture which will lead to an evaluation of the analogs of thermodynamic properties of a classicalon like entropy and temperature and also a computation of the number of its decay products. We will then use these results to make predictions for signals at the LHC. As we will see, like black holes, classicalons decay to give high multiplicity final states. Unlike black holes, however, the classicalons do not couple universally to all SM particles. In particular, there is no direct coupling to light quarks so that classicalons have a much lower production cross-section than black holes of the same energy. For the same reason, classicalon production, unlike black hole, production is not the dominant scattering process at energies above the classicalization scale with other SM scattering processes having a higher cross section. In Section 2, we carry

out the statistical mechanical analysis of classicalon decays and use the results we find to make LHC predictions in Section 3. Finally we make concluding remarks in Section 4.

2.2 Classicalon statistical mechanics

We will now describe a more precise formulation of the intuitive picture in Fig. 2.1 and obtain quantitative results. In theories that exhibit classicalization, in addition to the free lagrangian there are non-linear self-sourcing terms which are important only if the energy $\sqrt{\hat{s}}$ gets localized in a radius r_* given by Eq.(2.3). This leads to the formation of a classical configuration of mass $M = \sqrt{\hat{s}}$ which decays into many particles.

We will assume that the only requirements for forming a classicalon are

- conservation of energy and momentum, that is,

$$(2.5) \qquad\qquad |\vec{k_1}| + |\vec{k_2}|.... + |\vec{k_N}| = M$$

$$(2.6) \qquad\qquad \vec{k_1} + \vec{k_2}.... + \vec{k_N} = 0$$

where k_i are the four-momenta of the incoming particles,

- localization of the energy of the incoming particles inside the classical radius r_*.

As we will see later, the conservation of the 3-momentum does not lead to any constraint as it is automatically satisfied for $N \gg 1$. As the time reverse of every classicalon formation process is a classicalon decay process, this implies that every possible way of choosing a final state respecting the above conditions gives us an allowed classicalon decay. We will think of the set of four momenta of the incoming/outgoing particles in a particular formation/decay process of a classicalon of a given mass, M, as a *microstate*. The combinatoric exercise of counting the number

of ways of choosing these four vectors such that the energy adds up to the classicalon mass would be very similar to the statistical mechanical analysis of ideal Bose gasses or blackbody radiation. As we will see, however, unlike the case of an ideal gas or blackbody radiation, the particles here are not in general represented by waves confined to a box. The wave-packets must have a size and shape such that the second condition is satisfied and this leads to a density of states function different from the blackbody radiation case. The statistical mechanics of classicalons will thus be very different from blackbody radiation resulting in different thermodynamic relations. We will now see what the condition for localization of the energy inside the radius r_* tells us about the geometry of the incoming wave-packets.

2.2.1 Geometry of wave-packets

We will see in this section that in order to localize most of their energy inside the classicalon radius, r_*, the incoming wave-packets in a classicalon formation process (and thus the outgoing wave-packets in a classicalon decay process) can have a longitudinal width at most of the order of r_*, but are allowed to have a much bigger transverse length, $\sqrt{N}r_*$, where N is the number of incoming particles. We will consider a massless classicalizer field ϕ and discuss later how our results can be generalized to the massive case. We will not have to take into account the effect of the classicalizing interaction as we will assume that if the wave-packets are able to localize their energy inside the radius r_*, in the absence of a classicalizing interaction, they would form a classicalon in the presence of one.

We consider the formation of a classicalon from N incoming particles where $1 \ll N \leq N_{max}$ as shown in Fig. 2.2 (left), propagating freely such that they all reach the origin at the same time, $t = 0$. As $N \gg 1$ we can think of these wave-packets to be distributed approximately isotropically in all directions, giving rise to
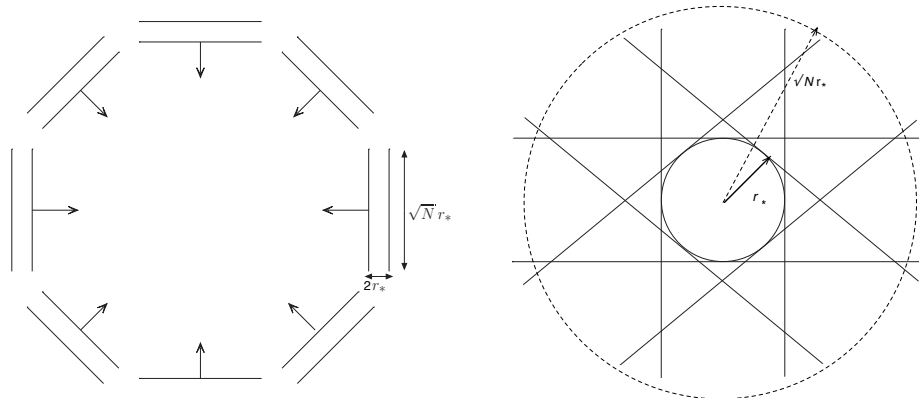
Figure 2.2: Classicalon formation from many incoming wave-packets which superpose to give an incoming spherically symmetric disturbance. We show the situation at $t \leq 0$ (left) and at $t = 0$ (right) when the wave-packets reach the origin. We show that at the moment $t = 0$ when all the wave-packets reach the origin, a field exists outside the classicalon radius because the wave-packets have transverse length bigger than r_*. The field outside, however, drops off as $\phi \sim 1/r$ so that most of the energy is still localized inside r_*. As we discuss in the text, these wave-packets have transverse length, $\sqrt{N}r_*$ so that the $\phi \sim 1/r$ tail exists as far as $r = \sqrt{N}r_*$, that is, as far as the dashed circle shown above.

a spherically symmetric incoming disturbance (for $t < 0$) when they are superposed with each other. In Ref. [23] it has been discussed how classicalons can be formed from the collapse of a spherical wave-packet of finite width. The spherical wave-packet collapses according to the free wave equation when its radius $r > r_*$. As the wave-packet collapses to a radius smaller than r_*, the non-linear classicalizing term in the lagrangian becomes important and it does not allow the energy to be localized at distances shorter than r_*. This leads to the formation of a classical configuration of radius r_* even if the original width of the wave-packet is much smaller. Clearly the spherical wave-packet cannot have width bigger than the classicalon diameter $2r_*$ otherwise its energy cannot be localized within the radius r_* and a classicalon would not be formed.

In our picture, such a spherical disturbance corresponds to a superposition of many incoming 'plane' wave-packets of longitudinal width $2r_*$ as shown in Fig. 2.2 (left). Hence we will take for each wave-packet the boundary conditions for modes

confined in a one dimensional box of size $2r_*$. For an incoming wave-packet with a definite squared energy, $\omega^2 = k^2$, we, therefore, take the following functional form in the longitudinal coordinate l,

$$(2.7) \qquad\qquad \phi(l) = \sin k(l + r_*)$$

with the k quantized as,

$$(2.8) \qquad\qquad k = n\pi/2r_*.$$

Here l is the longitudinal displacement from the center of the wave-packet and we are not writing the time dependance. Note that the above function satisfies $\phi(l = -r_*) = \phi(l = r_*) = 0$. As any function with compact support in the width of the wave-packet can be decomposed as a superposition of the above modes, this means that we are considering all possible wave-packet profiles which go to zero outside the width of the wave-packet. In particular we are considering wave-packets with widths smaller than $2r_*$.

What about the transverse length of the wave-packets? In the transverse direction the wave-packets can actually have a length much bigger than r_*. This leads to the existence of a field outside the classicalon radius r_* when the wave-packets superpose at the origin at $t = 0$, as is clear from Fig. 2.2(right), but, as we show in Appendix A, the field outside the classicalon radius drops off as $\phi \sim 1/r$ so that most of the energy is still inside the classicalon radius r_*. The $1/r$ behavior is expected because we are superposing solutions of the free wave equation which becomes Poisson's equation in the static limit. For $t > 0$, the classicalon decays and it is clear that the field at any point outside r_* remains unchanged from its $t = 0$ value until the information of the classicalon decay reaches it. Hence if there is a $\phi \sim 1/r$ tail at $t = 0$, we expect such a tail to remain at points outside the spherical wave-packet which it has not

yet reached. Similarly there exists a $\phi \sim 1/r$ tail outside the incoming wave-packets for $t < 0$. The appearance of the $\phi \sim 1/r$ tail outside the classicalon is interesting because such a tail in fact exists in the static solutions discussed in Ref. [18]. It is necessary because it leads to the flux of the gradient $\nabla\phi$ that must exist because of the source. We will show in Appendix A that $\phi \sim Q/r$, where $Q = \sqrt{N}$ matches with the 'charge' of the classicalizing source at the parametric level.

So far we have been assuming that the wave-packets are infinitely large in the transverse direction. This would, however, create a problem unless we have a superposition of an infinite number of wave-packets. This is because, as it is clear from Fig. 2.2(right), if there are a finite number of wave-packets, at large distances the wave-packets will not overlap anymore and thus we would not get the superposition leading to the $1/r$ fall off of the field. For a finite number of wave-packets with infinite transverse dimensions most of the energy of the wave-packets would be localized at large distances where there is no overlap between the different wave-packets. Thus our wave-packets must have large but finite transverse dimensions. We show in Appendix A that the distance at which the wave-packets stop overlapping is given by,

$$(2.9) \qquad\qquad L = \sqrt{N}r_*.$$

Thus we see that the incoming/outgoing particles in a classicalon formation/decay process, can be represented by wave-packets of size $2r_*$ in the longitudinal direction and size $\sqrt{N}r_*$ in the transverse direction.

Before going into our quantitative derivations, we will describe what happens qualitatively. At times $t < 0$ and distances from the origin much larger than r_*, the wave-packets travel freely and the number of quanta is conserved. As the wave-packets approach distances closer than r_*, the non-linear classicalizing term becomes

important, the number of particles is no longer conserved and can increase or decrease from the initial number. As we said earlier, we will think of the set of four-momenta in a particular formation/decay process of a classicalon of a given radius as a microstate. Whereas the initial number of particles and their momenta can be arranged to be anything by us, we would expect the classicalon to decay to a number of particles and with an energy distribution for the decay particles that corresponds to the maximum number of microstates. We want to find this distribution function which corresponds to maximum number of microstates. The first ingredient we need is the density of states function.

2.2.2 Density of states function

We want to find out the density of states for the wave-packets we described, that is the number of wave-packets of the kind described above that have energy in the range ω to $\omega + d\omega$. We will obtain such wave-packets by superposing free wave modes confined in a box of volume $V = L^3$ where L is given by Eq.(2.9). To get a wave-packet with momentum $\vec{k}$ and width $2r_*$ we would have to superpose many waves with momentum in the same direction as $\vec{k}$ and magnitude around $|\vec{k}|$.[2] For waves confined in a box all values of (k_x, k_y, k_z) are not allowed, instead only a lattice of points in k-space is allowed. Another way of saying this is that in a shell in k-space between the radii ω and $\omega + d\omega$ all possible directions are not allowed. We want to find the number of states that lie within this shell. For the modes confined in the box we know that the density of states is given by,

(2.10)
$$g_{\vec{k}} d^3 k = \frac{V}{8\pi^3} d^3 k.$$

---

[2]Note that this way of constructing our wave-packets ensures that any two wave-packets traveling in different directions are linearly independent. The functional form in Eq.(2.7) ensures that two wave-packets in the same direction, but with different $\omega = k$, are also linearly independent.

Going to spherical coordinates, $d^3k \to 4\pi k^2 dk = 4\pi\omega^2 d\omega$, this gives,

$$(2.11) \qquad\qquad g_\omega d\omega = \frac{V\omega^2}{2\pi^2} d\omega = \frac{1}{8\pi^3} L d\omega \times L^2 (4\pi\omega^2)$$

Up to factors of π the first term here is the number of box modes in a particular direction having energy in the range ω to $\omega + d\omega$ and the second term is the number of allowed directions. As we are considering wave-packets of width $2r_*$ and not L in the longitudinal direction, the number of wave-packets in a particular direction with energy in the range ω to $\omega + d\omega$ will be smaller by a factor $2r_*/L$ so that we get,

$$(2.12) \qquad\qquad g_\omega d\omega = \frac{1}{8\pi^3} (2r_*) d\omega \times (\sqrt{N}r_*)^2 (4\pi\omega^2) = \frac{Nr_*^3 \omega^2}{\pi^2} d\omega$$

where we have substitutes L from Eq.(2.9). One must also keep in mind that there are no wave-packets with energy less than $\pi/2r_*$ (see Eq.(2.8)). It is useful to write the density of states function also in cartesian coordinates,

$$(2.13) \qquad\qquad g_{\vec{k}} \, d^3k = \frac{Nr_*^3}{4\pi^3} \, d^3k.$$

Note that the existence of the extra factor of N in Eqs.(2.12) and (2.13), as compared to the case of a particle confined in a box, is crucial and leads to thermodynamic relations for a classicalon different from ideal Bose gasses or blackbody radiation.

2.2.3 Number of N particle decays for $1 \ll N \ll N_{max}$

We want to count the number of ways a classicalon of mass M can decay to N particles which is the same as the number of ways of forming a classicalon from N particles. We want to show that the number of ways is higher for larger N, thus proving that a classicalon prefers to decay to many particles. We will now evaluate $\Gamma(M, N)$, the number of ways in which N incoming particles, where $1 \ll N \ll N_{max}$, can form a classicalon of a given mass, M. Note that for our derivation here we will

assume that in each energy state there is at most one particle which is a very good approximation for $N \ll N_{max}$. The total number of ways of forming a classicalon would be,

$$(2.14) \qquad \Omega(M) = \sum_{N=2}^{N_{max}} \Gamma(M, N).$$

We try to find all possible set of four vectors of the N outgoing wave-packets with the only constraint that energy and momentum are conserved,

$$(2.15) \qquad |\vec{k_1}| + |\vec{k_2}|.... + |\vec{k_N}| = M$$

$$(2.16) \qquad \vec{k_1} + \vec{k_2}.... + \vec{k_N} = 0$$

For large N, the momentum conservation constraint is not important simply because the sum $\vec{k_1} + \vec{k_2}.... + \vec{k_{N-1}}$ is completely unconstrained as we can always fix $\vec{k_N}$ to ensure that the sum $\vec{k_1} + \vec{k_2}.... + \vec{k_N} = 0$. For $N \gg 1$, $|\vec{k_N}|$, which is the energy of a single particle is negligible compared to M, so that the two conditions above can be reduced to a single energy conservation condition $|\vec{k_1}| + |\vec{k_2}|.... + |\vec{k_{N-1}}| = M$ on the $N - 1$ particles. For large N, however we can always replace $N - 1$ by N. Using Eq.(2.13) we thus get the following phase space integral with only the energy conservation constraint,

$$(2.17) \quad \Gamma(M, N) = \frac{((N/4)(r_*/\pi)^3)^N}{N!} \int d^3k_1 d^3k_2 ... d^3k_N \delta(|\vec{k_1}| + |\vec{k_2}|.. + |\vec{k_N}| = M).$$

The $N!$ in the denominator appears because the particles are indistinguishable and all possible permutations result in the same state. The integral above is a well-known integral in statistical mechanics that appears in the evaluation of entropy of an ideal ultra-relativistic gas. For $N \gg 1$, the result is (see for instance Pg. 153 of Ref. [29]),

$$(2.18) \qquad \Gamma(M, N) = \frac{2^N(\sqrt{3})^{3N} N^N (r_* M/\pi)^{3N}}{N!(3N)!} = \frac{2^N(\sqrt{3})^{3N} N^N N_{max}^{3N}}{\pi^{3N} N!(3N)!}.$$

It is easy to check that $\Gamma(M, N)$ is an increasing function of N, which shows that a classicalon would prefer to decay to many particles and not a few.

2.2.4 Classicalons as Bose-Einstein systems

In this subsection we will try to find the most probable energy distribution of the particles a classicalon decays to. In other words we will try to find the distribution with the maximum number of microstates, $\tilde{\Omega}(M)$. As is usually assumed in statistical mechanics we will assume that the total number of ways of forming the classicalon, $\Omega(M)$ in Eq.(2.14), is approximately equal to the total number of ways of forming the most probable distribution, that is,

$$(2.19) \qquad\qquad \Omega(M) \approx \tilde{\Omega}(M).$$

Parts of the discussion here will be very similar to the standard derivation of the Bose-Einstein distribution for a massless system although the density of states function here is different.

We want to find the most probable value of N_ω, the number of particles in the energy state with energy ω. In the continuum limit, N_ω becomes $N(\omega)$, the distribution function. As explained in the previous subsection, the only constraint is the energy conservation constraint in Eq.(2.15) which we rewrite as,

$$(2.20) \qquad\qquad \sum_\omega N_\omega g_\omega \omega \; d\omega = M.$$

We first need to find $\Omega(M)$, the number of ways of choosing the four momenta of the decaying particles while satisfying the constraint in Eq.(2.20). As we review in Appendix B, this is given by the well known expression,

$$(2.21) \qquad\qquad \Omega(M) = \Pi_\omega \frac{(N_\omega + g_\omega)!}{N_\omega! g_\omega!}$$

We can define the entropy of the system as,

$$(2.22) \qquad\qquad S = \log(\Omega(M)).$$

We want to maximize S respecting the constraints in Eq.(2.20). As shown in Appendix B, using the method of Langrange multipliers, this leads to the Bose-Einstein distribution,

$$(2.23) \qquad\qquad N_\omega = \frac{g_\omega}{e^{\beta\omega} - 1}.$$

Here β is the Lagrange multiplier related to the constraint in Eq.(2.20) and effectively plays the role of inverse temperature. To obtain β and the number of particles in the most probable distribution, N_*, we now go to the continuum limit replacing the summations above by integrals and solve the equations,

$$(2.24) \qquad N_* = \int_{\omega=\pi/2r_*} g(\omega)d\omega = \frac{N_* r_*^3}{\pi^2} \int_{\omega=\pi/2r_*} \frac{\omega^2 d\omega}{e^{\beta\omega} - 1}$$

$$(2.25) \qquad M = \int_{\omega=\pi/2r_*} \omega g(\omega)d\omega = \frac{N_* r_*^3}{\pi^2} \int_{\omega=\pi/2r_*} \frac{\omega^3 d\omega}{e^{\beta\omega} - 1}.$$

Note that the lower limit in the integral is not zero but the minimum allowed frequency for our wave-packets $\pi/2r_*$ (see Eq.(2.8)). To obtain β make the substitutions $\beta\omega = x$ in Eq.(2.24) to obtain,

$$(2.26) \qquad\qquad \int_{x=\beta\pi/2r_*} \frac{x^2 dx}{e^x - 1} = (1/\pi)(\beta\pi/r_*)^3.$$

Both the LHS and RHS of the above equation depend on $\beta\pi/r_*$. While the RHS obviously increases with $\beta\pi/r_*$ the integral in the LHS decreases as the lower limit is raised so it decreases with $\beta\pi/r_*$ and we find a unique solution at $\beta\pi/r_* \approx 1.9$. The precise numerical coefficients should not be taken seriously and only the parametric relationships are important. We get,

$$(2.27) \qquad\qquad \beta \sim r_* \Rightarrow T \sim \frac{1}{r_*}.$$

Now to find N_* we use Eq.(2.25), again substituting $\beta\omega = x$, to get,

$$(2.28) \qquad \frac{N_* r_*^3}{\pi^2} \beta^{-4} \int_{x=\beta\pi/2r_*} \frac{x^3 dx}{e^x - 1} = M.$$

Now substituting the solution of Eq.(2.26), $\beta \sim r_*$, we get,

$$(2.29) \qquad N_* \sim M r_* \sim N_{max}.$$

The above expression shows that the typical energy of a quanta is $M/N_* \sim 1/r_*$, so that the typical wavelength is r_*. This is what we expect from the dynamics of classicalization as r_* is the length scale at which classicalization takes place [25]. Now we can also evaluate the entropy,

$$S = \int \beta dM \sim \int r_* dM \sim \int \frac{M^\alpha}{M_*^{1+\alpha}} dM \sim \left(\frac{M}{M_*}\right)^{1+\alpha} \sim M r_*$$

$$(2.30) \qquad \Rightarrow \quad S \sim N_* \sim N_{max}$$

where we have substituted r_* using Eq.(2.3) taking $\sqrt{\hat{s}} = M$. Thus we have found that the classicalon decays to the maximum number of particles it can, N_{max}, with a blackbody spectrum having $T \sim 1/r_*$. We see that the total number of decays is $\Omega(M) = e^S$, so that probability of decays to a few particles, which is a small number compared to e^S, would be exponentially suppressed,

$$(2.31) \qquad P(Classicalon \rightarrow few) \sim \frac{1}{\Omega(M)} \sim e^{-S} \sim e^{-N_*}.$$

in accordance with Ref [25] .

We now consider the special case of a black hole for which $\alpha = 1$, $M_* = M_{pl}$ and r_* is the Schwarzschild radius. As a black hole does not decay classically, the above analysis for the distribution of the decay products cannot be applied to a black hole. As argued in Ref. [25], however, classicalization is the first step to the formation of a black hole and this takes place before the horizon emerges. Thus

our calculation of the entropy which is basically a counting of the number of ways in which a classicalon can be formed should give us the correct black hole entropy. Indeed, we find for $\alpha = 1$,

$$(2.32) \qquad\qquad S \sim N_* \sim M r_* \sim M_{pl}^2 r_*^2$$

in agreement with the Bekenstein-Hawking formula.

We want to emphasize that obtaining the parametric relationships above is far from assured based only on dimensional grounds. For instance if we had taken wave-packets of size $2r_*$ in both the longitudinal and transverse directions we would have found the usual density of states for an ideal gas, $g(\omega)d\omega \sim r_*^3 \omega^2 d\omega$ without the factor N. This would lead to the usual relationships $M \sim r_*^3 T^4$ and $S \sim r_*^3 T^3$ for blackbody radiation. The fact that the wave-packets are of size $\sqrt{N} r_*$ in the transverse direction is thus crucial in obtaining the final result we have derived. As we discussed earlier in Section 2.2.1 (and show in detail in Appendix A) a transverse length much greater than r_* is in fact necessary for generating the $\phi \sim 1/r$ tail of the field outside the classicalon.

We want to mention some modifications that we will make in our expressions before using them for experimental predictions The first issue is regarding the lower limit $\omega = \pi/2r_*$ in the integrals. It is not true that energies smaller than $\omega = \pi/2r_*$, or larger wavelengths, $\lambda \gg r_*$, are not present. This is because the distribution function we have derived is for wave-packets of size of the order of r_* in the longitudinal direction. A detector, however, would detect plane waves much larger in size and the wave-packets of size r_* are themselves composed of plane waves of much have larger wavelengths. Note that this does not have any effect on the distribution function for higher energies (smaller wavelengths). We will not attempt to find the correct distribution at lower energies (longer wavelengths) as our assumption that the dis-

tribution function suddenly drops to zero for wave-packets with width larger than r_* is a simplifying approximation and is not accurate. It is reasonable to expect that a more precise analysis would yield the Planck distribution over the whole energy range. Even in this case the lower frequencies would be suppressed due to the phase space factor $\omega^2 d\omega$. Therefore from here onwards we will get rid off the lower limit $\omega = \pi/2r_*$ in the integrals and take the lower limit to be the lowest kinematically allowed value, $\omega = m$, m being the mass of the ϕ-quanta. We need to make a second modification because we have been assuming so far, a classicalizer field that is massless, whereas it is massive in the models we are going to consider. While deriving our density of states function we made in Eqs.(2.11) and (2.12) the substitution $k^2 dk = \omega^2 d\omega$ which assumes that the ϕ-quanta are massless. Using $k^2 = (\omega^2 - m^2)$ instead, m being the mass, we get the correct density of states expression in the massive case,

$$(2.33) \qquad\qquad g(\omega)d\omega \sim Nr_*^3 k^2 dk \sim Nr_*^3 \omega\sqrt{\omega^2 - m^2} \; d\omega.$$

Finally, in order to make experimental predictions, we will fix the unknown numerical coefficients in the parametric form of the density of states function above by using the black hole example where the exact expressions are well known. We will describe this in more detail in the next section.

2.3   Classicalons at the LHC

Now that we know how to compute the number of decay products in a classicalon decay, we are ready to perform a collider study of classicalization in the phenomenological models introduced in the Section 2.1. Along with the decay multiplicity expression, the other important fact that we will use for our study is that classicalon production has a geometric cross-section πr_*^2. The two models we are going to con-

sider are the classicalization of longitudinal Ws and Zs and the classicalization of Higgs bosons. The LHC signal would be multi-W/Z production in the first case and multi-Higgs production in the second case. As in the case of black hole production in TeV-scale quantum gravity models [30–33], this would finally lead to production of leptons and many jets. Unlike black holes, though, classicalon production would not be a universal phenomenon in hard scattering processes at energies above the cut-off scale.[3] This is because the light quarks and gluons would not have a strong coupling to the classicalon in both the cases we will consider. This is the main difference of classicalization signals from black hole signals. Thus even at energies higher than the classicalization scale, normal SM $2 \rightarrow 2$ hard scattering processes would continue in other channels with cross-sections larger than classicalon production. Another result of the absence of any direct coupling between classicalons and light quarks or gluons is that classicalon production would have a much smaller cross-section compared to black hole production at the same scale, so that classicalons would be harder to discover/exclude at colliders.

Before going into the details, there is a caveat that must be emphasized. The phenomenon of classicalization is well understood only for energies much higher than the classicalization scale. In particular the quantitative expressions that we will use, for instance, the expressions for the radius, cross-section and decay multiplicity, strictly hold only in the limit of large number of quanta, i.e. for $N_* \gg 1$ or equivalently for energies much higher than the cut-off, $\sqrt{\hat{s}} \gg M_*$. This is the classical limit as well as the thermodynamic limit where our statistical assumptions are true. As the energies accessible at the LHC are not so high, we will be forced to consider processes where

---

[3]In gravitational high energy scattering above the Planck scale, black hole formation is expected for impact parameters smaller than the Schwarzschild radius or equivalently for large scattering angles. For impact parameters much larger than the Schwarzschild radius and transplanckian energies elastic $2 \rightarrow 2$ scattering should take place which is well described by the eikonal approximation ($t/s \ll 1$) [34, 35].

$N_* \sim 6$. Many would consider these energies to be still part of the 'quantum regime' around the classicalization scale. The same problem exists in collider analyses of black hole formation and decays in TeV-scale quantum gravity scenarios [36]. Black holes can be reliably tackled by theory only at energies much higher than the Planck scale. In the regime around the classicalization (Planck) scale, it is more appropriate to think of classicalons (black holes) as a tower of quantum resonances than as classical objects [37]. There is, however, no theoretical model for this quantum regime that can be used to make reliable experimental predictions. Thus in the absence of a better alternative the only choice we have is to use the expressions for the classical regime, as has been done in studies of black holes so far. We will, however, incorporate in our analysis the fact that classicalon masses are quantized.

2.3.1 Classicalization of longitudinal Ws and Zs

As is well known, in the absence of the Higgs boson the scattering of the longitudinal components of W and Z bosons violates tree-level unitarity at energies of the order of a TeV [4]. In Ref. [18] it was proposed that classicalization can unitarize these amplitudes. In this proposal the longitudinal (goldstone) modes of the vector bosons classicalize and form a configuration of Ws and Zs that finally decay into many Ws and Zs.

For our anlysis we will take the classicalizing interaction proposed in Ref. [18],

$$(2.34) \qquad \frac{c}{2}(\text{Tr}\left(D^\mu U D_\mu U^\dagger\right))^2$$

where U is the SU(2) matrix $\exp(i\pi_a\tau_a/v)$ containing the goldstones π_a. Here $v = 246$ GeV is the Higgs vacuum expectation value (VEV) and τ_a are the Pauli matrices. The covariant derivative above is defined as follows,

$$(2.35) \qquad D_\mu U = \partial_\mu U + ig\frac{\tau_a}{2}W^a U - ig'U B_Y\frac{\tau_3}{2}.$$

When expanded the operator in Eq.(2.35) gives the following classicalizing interaction,

$$(2.36) \qquad \frac{c}{v^4}(\partial_\mu \chi_a \partial^\mu \chi^a)^2$$

For this particular operator the classicalon radius is given by [18, 23],

$$(2.37) \qquad r_* \sim c^{1/3}\frac{M^{1/3}}{v^{4/3}} \sim \frac{M^{1/3}}{M_*^{4/3}},$$

where, $M_* = v/c^{1/4}$, is the classicalizing scale. Note that the above relationship is valid only until r_* reaches the Compton wavelength of the Z-boson, $1/m_Z$. Beyond this point the radius would freeze at the value $1/m_Z$ [18]. The experimental constraints on the coupling c come from electroweak precision measurements. Only the T parameter gets a contribution from this operator and the other electroweak parameters (the S parameter and the six electroweak parameters U-Z as defined in Ref. [38] for instance) get no contribution. The contribution to the T parameter is given by [39],

$$(2.38) \qquad \Delta T = \frac{-c}{4\pi^2 \alpha_{em}}\left(\frac{3g^2 g'^2}{2} + \frac{3g'^4}{4}\right)\log\frac{M_*}{m_Z}.$$

As $c = (v/M_*)^4$, we see that the ΔT contribution is small for $M_* \gtrsim 500$ GeV. For $M_* = 246$ GeV the contribution is appreciable and, as we are considering a higgsless theory, we see that a negative c is preferred. From Eq.(2.38) we see that for $c = -1$(and hence $M_* = v$) we get $\Delta T = 0.3$ which is acceptable in a higgsless theory. For higher values of M_* the contribution to ΔT would be much smaller. There would, however, be additional contributions to electroweak precision observables from the quantum resonances that exist in such a theory around the classicalizing scale, M_*. These contributions are unfortunately not calculable without a knowledge of

the precise dynamics at the classicalizing scale. All we can do is make the general statement that a higher classicalization scale will mean smaller contributions to electroweak precision observables from these resonances.

We will absorb the unknown numerical coefficient in Eq.(2.37) in a redefinition of the coupling c to obtain,

$$(2.39) \qquad\qquad r_* = c^{1/3} \frac{M^{1/3}}{v^{4/3}} = \frac{M^{1/3}}{M_*^{4/3}}.$$

Note that the classicalization scale, $M_* = v/c^{1/4}$, cannot be much higher than the TeV scale as WW-scattering needs to be unitarized before these energies are reached. We will make computations for the three choices of the classicalization scale, $M_* = 246$ GeV, $M_* = 600$ GeV and $M_* = 1$ TeV.

Multiplicity of gauge bosons in the final state

We want to find the total number of W/Zs a classicalon of a given mass, M, would finally decay into. We are not allowed to use the massless limit of the expressions we derived (Eqs.(2.24) and (2.25)) in this case. One way of seeing that the massless approximation is not valid here is that the expression for multiplicity in the massless limit would give us multiplicity greater than the kinematic bound $M/m_{W/Z}$. The reason we need to consider the mass is that, in this case, the kinetic energy $k \sim 1/r_*$ does not dominate the energy of the individual quanta as the mass of the quanta is comparable, that is $m_{W/Z} \sim 1/r_*$. This is in turn because of the small separation between the mass $m_{W/Z}$ and the classicalization scale $M_* = v/c^{1/4}$. Thus we use the the density of states for the massive case given previously in Eq.(5.39),

$$(2.40) \qquad\qquad g(\omega)d\omega = \gamma N_* r_*^3 \omega \sqrt{\omega^2 - m^2} d\omega,$$

where γ is an unknown numerical coefficient that we will fix by demanding that we get the exact result in the black hole case. We will not consider here the effects of

the difference in W and Z mass which is small compared to the classicalon mass. To be conservative we will take the mass of all the quanta forming the classicalon, $m = 91.2$ GeV the Z-mass. We find the number of decay particles by solving for β and N_*, the Eqs.(2.24) and (2.25) but with the modified density of states function in Eq.(5.39) and a different lower limit,

$$(2.41) \qquad \gamma N_* r_*^3 \int_m^M \frac{\omega \sqrt{\omega^2 - m^2} d\omega}{e^{\beta\omega} - 1} = N_*$$

$$(2.42) \qquad \gamma N_* r_*^3 \int_m^M \frac{\omega^2 \sqrt{\omega^2 - m^2} d\omega}{e^{\beta\omega} - 1} = M.$$

We have explained at the end of Section 2.2.4 why the lower limit in the integrations above has been changed from the lower limit in Eqs.(2.24) and (2.25). We fix the factor γ above by requiring that for $m = 0$ we get from Eq.(2.41), the exact black hole result,

$$(2.43) \qquad \beta^{-1} = T = \frac{1}{4\pi r_*}.$$

This gives[4],

$$(2.44) \qquad \gamma = \frac{(4\pi)^3}{2\zeta(3)} \approx 825,$$

where $\zeta(n)$ is the Riemann zeta function.

The results of our evaluation are shown in Table 2.1 and Fig. 2.4 (left) for our three choices, $M_* = 246$ GeV, $M_* = 600$ GeV and $M_* = 1$ TeV. We see that instead of the dependence $N_* \sim Mr_* \sim M^{4/3}$ expected in the massless limit, we find an almost linear dependence $N_* \sim M$ (the dependence is not exactly linear as can be seen from the values in Table 2.1). For comparison we also show the N_* vs M dependence for extra-dimensional black holes in Fig. 2.4 (left). We have used the expression for N_*

---

[4]Note that the analytical expression strictly holds only in the limit that the upper limit (after the substitution $\beta\omega = x$) of the integration in Eq.(?2.41) , $\beta M \to \infty$. We, however, find it to be a very good approximation in the examples we consider.
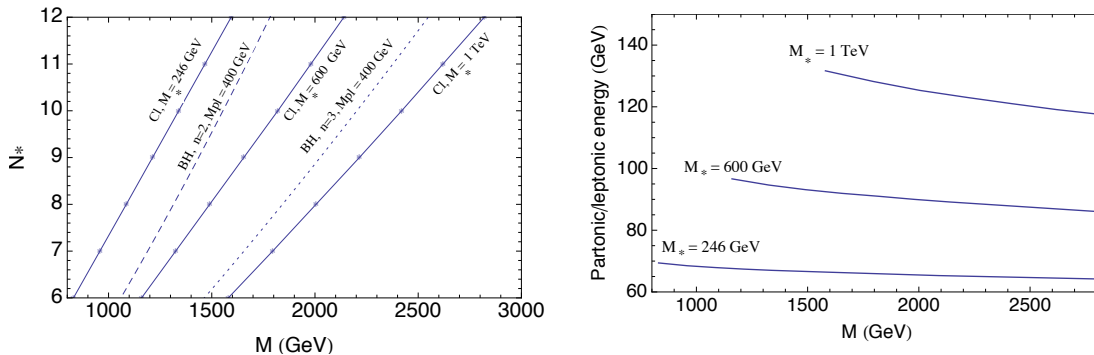
Figure 2.3: In the model of classicalization of longitudinal Ws and Zs we show the number of quanta N_* as a function of the classicalon mass M in the figure on the left. In the figure on the left, we also show the N_* vs M curves for some black hole examples. Classicalon states exist only at the points where values of N are integers. In the figure on the right, we show the typical energy, $M/2N_*$, of a lepton or parton emerging from one of the W/Zs produced in the classicalon decay, in the rest frame of the classicalon.

in Ref. [33],

$$(2.45) \qquad N_*^{BH} = \frac{2\sqrt{\pi}}{n+1} \left(\frac{M}{M_{pl}} \right)^{\frac{n+2}{n+1}} \left(\frac{8\Gamma(\frac{n+3}{2})}{n+2} \right)^{\frac{1}{n+1}} .$$

Here n is the number of extra dimensions and M_{pl} is the fundamental Planck scale in the $4+n$ dimensional space-time. We have taken $n = 2, 3$ and $M_{pl} = 400$ GeV. Note that the value $M_{pl} = 400$ GeV has been chosen close to the classicalization scale only for comparison and such low values of M_{pl} have already been ruled out [40]. Higher values of M_{pl} will give much lower N_* values. As one can see in the figure, for the $n = 2$ case, the N_* vs M curve is clearly not linear whereas for the $n = 3$ case the non-linearity due to the $N_* \sim M^{\frac{n+2}{n+1}}$ dependence is not noticeable. As n is increased (note that larger n values are preferred because of astrophysical bounds [41]) the curve would become more and more linear and N_* would decrease. Note that whereas N_* is the final decay multiplicity in the case of black holes, in the case of classicalons the multiplicity of final decay products is actually bigger than (about twice) N_*, because N_* is just the number of the primary decay products, the Ws and Zs, which decay further giving rise to more leptons and jets. Keeping this in mind one can from see from Fig. 2.4 (left) that the multiplicity of final decay products is larger
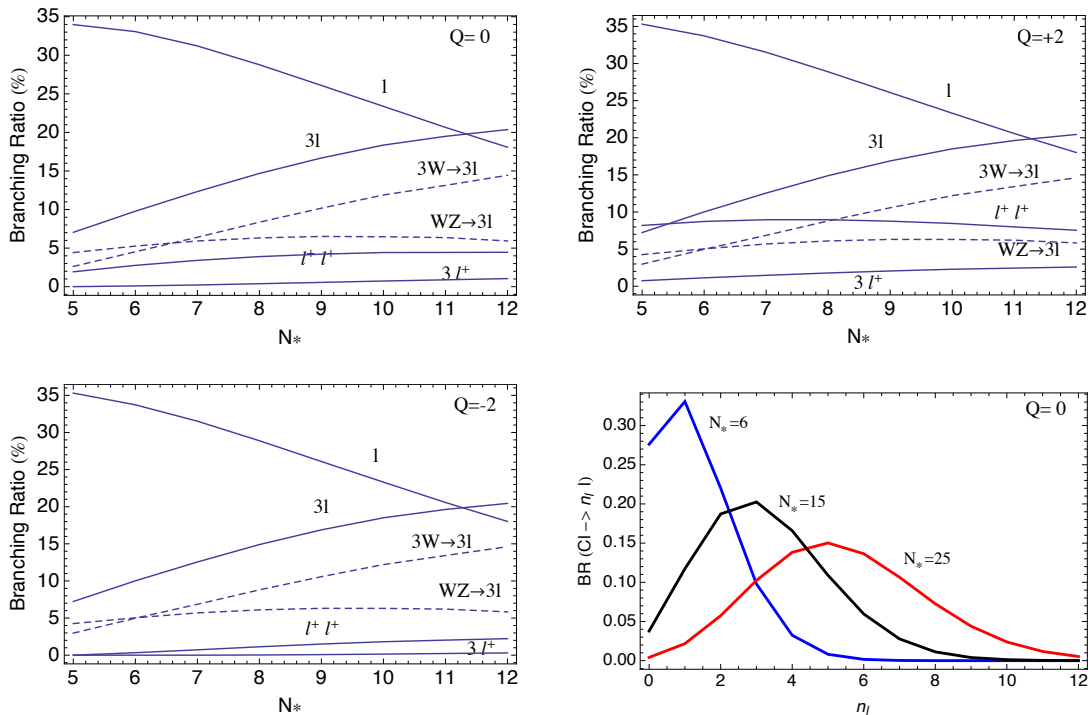
Figure 2.4: In the model of classicalization of longitudinal Ws and Zs we also show the branching fractions for a neutral classicalon (top left) and for classicalons with electric charge, $Q = \pm 2$ (top right/bottom left). In the figure on the bottom right, we show the classicalon branching ratio to n_l leptons for a neutral classicalon. In the decay channels shown above we require exactly (and not at least) the number of leptons mentioned.

for these classicalons when compared to black holes of the same mass even for such small values of n and M_{pl} as $n = 2$ and $M_{pl} = 400$ GeV. In the figure on the right, we show the typical energy, $M/2N_*$, of a lepton or partonic jet emerging from one of the W/Zs produced in the classicalon decay, in the rest frame of the classicalon. An experimental measurement of the typical energy would tell us about the N_* vs M dependance for the classicalon. We will discuss this measurement in more detail later.

It is important to note that classicalons must have a discrete mass spectrum as was shown in Ref. [37]. The allowed masses are precisely the points marked in Fig. 2.4 (left), that is masses that give an integer value for N_*. At intermediate energies in between two allowed masses, a classicalon with a lower mass would be formed along

with some SM particle(s) [37] that carries the rest of the energy and momentum. We will assume in our analysis that at these intermediate energies the closest classicalon with a lower mass, say M_{N_*}, is formed with the cross-section $\pi r_*^2(M_{N_*})$. As the spacing between the masses that we have found is greater than the Z-mass, the additional SM particle emitted can even be a W/Z boson. This would mean that we may be able to get $(N_* + 1)$ W/Zs in the final state even at energies lower than M_{N_*+1}. We will avoid this complication as by ignoring this effect, which enhances the signal, we are only being conservative.

Branching ratios

In order to derive the classicalon branching ratio to a particular number of W^+, W^- and Zs, we will assume that a classicalon decays democratically and randomly to the three Goldstone components π_+, π_- and π_3, the only constraint being electrical charge conservation. By the Goldstone boson equivalence principle, we will thus get in the unitary gauge a number of longitudinal W^+, W^- and Zs equal to the number of π_+, π_- and π_3s in the final state. Thus the unnormalized probability of a particular N_*-particle classicalon composition with number of W^+ bosons equal to N_{W^+}, number of W^- bosons equal to N_{W^-} and number of Z bosons equal to N_Z, must be proportional to the number of possible ways of exchanging the identical particles amongst themselves to give the same final state, that is,

$$(2.46) \qquad P'(N_{W^+}, N_{W^-}, N_Z) = \frac{N_*!}{N_{W^+}!N_{W^-}!N_Z!}.$$

So for instance for a neutral classicalon with energy and radius such that we get $N_* = 5$ using Eqs.(2.41) and (2.42), the possible compositions are: $ZW^+W^-W^+W^-$, $ZZZW^+W^-$ and $ZZZZZ$. Computing probabilities as described above we get for

these different possibilities,

$$
\begin{aligned}
P'(ZW^+W^-W^+W^-) &= \frac{5!}{2!2!1!} \\
P'(ZZZW^+W^-) &= \frac{5!}{1!1!3!} \\
P'(ZZZZZ) &= \frac{5!}{0!0!5!}.
\end{aligned}
$$

(2.47)

Finally these probabilities must be normalized,

(2.48)
$$
P(N_{W+}, N_{W-}, N_Z) = \frac{P'(N_{W+}, N_{W-}, N_Z)}{\sum P'(N_{W+}, N_{W-}, N_Z)}.
$$

The sum in the above equation runs over all N_{W+}, N_{W-} and N_Z respecting $N_{W+} + N_{W-} + N_Z = N_*$ and $N_{W+} - N_{W-} = Q$, Q being the electric charge of the classicalon.

To find the branching fraction to leptons, jets and missing energy that the Ws/Zs decay to, we need to consider still more combinatoric possibilities. We discuss this in detail in Appendix C, where we provide expressions for the branching ratio to final states with varying number of leptons.

In Fig. 2.4 we show the branching ratio of classicalons with charge, $+2, 0$ and -2. Note that the branching ratio for decay channels with higher number of leptons rise with N_* whereas the branching ratio of the single lepton channel falls. This is so because classicalons with higher N_* decay to more leptons. This is clear from Fig. 2.4 (bottom right) where we show the classicalon branching ratio to n_l leptons. We see that an N_*-particle classicalon decays with maximum branching ratio to $n_l \sim N_*/5$ leptons. Note that the branching ratios in Fig. 2.4 have been computed at the theoretical level and do not include any experimental effects.

Signals at the LHC

At the LHC these classicalons can be produced in the vector boson fusion (VBF) process, $pp \to jj(W_L W_L \to Cl)$ (see Fig. 2.5). To compute the cross section for

M(GeV)	N*	Total Cross-section (fb)			Signal Cross-section			
		Q=+2	Q=0	Q=-2	l(fb)	l⁺l⁻(fb)	3l(3W → 3l, WZ → 3l) (fb)	3l⁺ (fb)
$M_* = 246$ GeV, LHC energy = 7 TeV								
830	6	8.3	7.6	1.7	5.9 [2.7]	0.9 [0.5]	1.7 (0.8, 0.9) [1.0 (0.5, 0.5)]	0.1 [0.06]
958	7	4.7	4.1	0.9	3.0 [1.2]	0.6 [0.3]	1.2 (0.6, 0.6) [0.6 (0.3,0.3)]	0.07 [0.04]
1086	8	2.7	2.3	0.5	1.6	0.3	0.8 (0.5, 0.3)	0.05
1213	9	1.6	1.3	0.2	0.8	0.2	0.5 (0.3, 0.2)	0.04
1340	10	1.0	0.7	0.1	0.4	0.1	0.3 (0.2, 0.1)	0.03
1467	11	0.6	0.4	0.07	0.2	0.07	0.2 (0.1, 0.07)	0.02
1594	12	0.4	0.3	0.04	0.1	0.04	0.2(0.1, 0.05)	0.01
$M_* = 246$ GeV, LHC energy = 14 TeV								
830	6	74	84	23	60 [28]	8.9 [4.8]	18 (8.6, 9.3) [11 (5.5, 5.0)]	0.9 [0.6]
958	7	50	55	15	38 [15]	6.4 [3.0]	15 (8.0, 6.9) [7.5 (4.3, 3.2)]	0.9 [0.5]
1086	8	33	35	9.2	22	4.4	11 (6.6, 4.8)	0.7
1213	9	23	24	5.9	14	3.1	8.9 (5.5, 3.4)	0.6
1340	10	16	16	3.9	8.4	1.9	6.6 (4.3, 2.3)	0.5
1467	11	12	11	2.7	5.3	1.5	5.0 (3.4, 1.6)	0.4
1594	12	8.8	8.3	1.9	3.4	1.1	3.9 (2.8, 1.1)	0.3
$M_* = 600$ GeV, LHC energy =14 TeV								
1160	6	3.1	3.2	0.8	2.4 [1.1]	0.6 [0.2]	0.7 (0.3, 0.4) [0.4 (0.2, 0.2)]	0.04 [0.02]
1325	7	2.0	1.9	0.5	1.4 [0.5]	0.2 [0.1]	0.5 (0.3, 0.2) [0.3 (0.2, 0.1)]	0.03 [0.02]
1490	8	1.3	1.2	0.3	0.8	0.2	0.4 (0.2, 0.2)	0.03
1655	9	0.9	0.8	0.2	0.5	0.1	0.3 (0.2, 0.1)	0.02
1820	10	0.6	0.5	0.1	0.3	0.07	0.2 (0.1, 0.07)	0.02
1980	11	0.4	0.4	0.08	0.2	0.05	0.2 (0.1, 0.06)	0.01
2140	12	0.3	0.3	0.05	0.1	0.04	0.1 (0.09, 0.04)	0.01
$M_* = 1$ TeV, LHC energy =14 TeV								
1580	6	0.3	0.3	0.07	0.2 [0.1]	0.03 [0.02]	0.07 (0.03,0.03) [0.04 (0.02,0.02)]	-
1795	7	0.2	0.2	0.03	0.1 [0.05]	0.02 [0.01]	0.05 (0.03,0.02) [0.03 (0.02,0.01)]	-
2005	8	0.1	0.1	0.02	0.06	0.01	0.03 (0.02,0.01)	-
1215	9	0.1	0.1	0.01	0.05	0.01	0.03 (0.02, 0.01)	-
2420	10	0.05	0.04	0.01	0.02	0.01	0.02 (0.01, 0.01)	-
2620	11	0.03	0.03	0.01	0.01	-	0.01 (0.01, -)	-
2820	12	0.02	0.02	0.01	-	-	0.01 (0.01, -)	-

Table 2.1: Cross-section for classicalon production by weak boson fusion in the model with goldstone classicalization. We give the total cross-section as well as the cross-section in the different channels. The number of leptons mentioned in each channel is the exact number of leptons in the final state. The values in the square brackets are the cross-section values assuming no invisible Z decays and no W decays to hadronically decaying τs, which ensures the maximum number of partonic jets. Note that no effect of showering, hadronization, experimental cuts or detector acceptances has been included here. For a discussion of these, see the text.
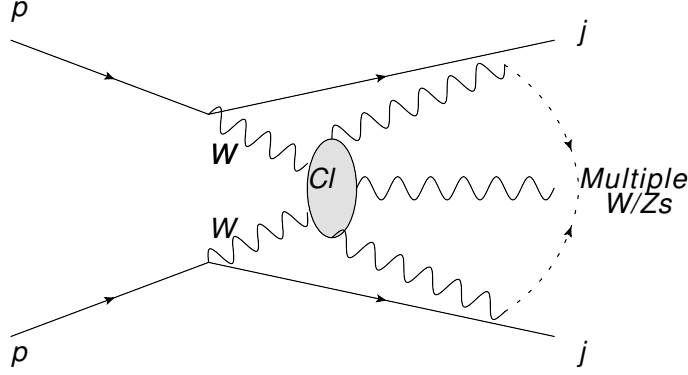
Figure 2.5: Production of a classicalon by weak boson fusion in the model with goldstone classicalization.

their production we use the effective W approximation. In this approximation the luminosity of longitudinal W bosons is given by [42],

$$(2.49) \qquad \frac{dL}{d\tau} = \left(\frac{g^2}{16\pi^2}\right)^2 \frac{1}{\tau}[(1+\tau)\ln(1/\tau) + 2(\tau - 1)]$$

where $\tau = \hat{s}/s_q$ is the ratio of the squared center of mass energy of the W-pair, $\hat{s}$, to the squared center of mass energy of the initial quarks, s_q. The cross-section for production of an N_*-particle classicalon is found by convoluting the geometric cross-section with this luminosity function and the parton density functions as follows,

$$(2.50) \qquad \sigma_N = \sum_{ij} \int_{M_{N_*}^2/s}^{M_{N_*+1}^2/s} d\tau \; \pi r_*^2(M_{N_*}) \int_\tau^1 \frac{d\tau'}{\tau'} \int_{\tau'}^1 \frac{dx}{x} f_i(x, q^2) f_j(\tau'/x, q^2) \frac{dL}{d\xi}$$

where now $\tau = \hat{s}/s$, s being the proton-proton center of mass energy squared, $\tau' = s_q/s$ and $\xi = \tau/\tau'$. We have taken the factorization scale $q^2 = m_W^2$. As we stated already, we have assumed that for energies $M_{N_*} < \hat{s} < M_{N_*+1}$, an N_*-particle classicalon is formed along with other SM particles with a cross-section $\pi r_*^2(M_N)$. For our computations we have used the MSTW parton density functions (PDF) [43]. In the summation above both i and j run over all positively charged quarks for W^+W^+ fusion which leads to production of classicalons with charge $+2$, and run over all negatively charged quarks for W^-W^- fusion which leads to production of

classicalons with charge -2. For production of neutral clasicalons from W^+W^- fusion i and j run over quarks with opposite electric charge. As we are considering only $W^\pm$ in the initial state, the classicalons produced can have charge only $-2, 0$ and $+2$. The contribution of initial states with a Z boson has been neglected here as the Z boson luminosity is much smaller compared to the W boson luminosity. For instance, the ZZ luminosity is an order of magnitude smaller than the W^+W^- luminosity [42].

The final states that would be seen in colliders are leptons plus multijets and missing energy. We will provide cross-sections for the final states, $l+\not{E}_T + jets$, $l^+l^+ + \not{E}_T + jets$, $3l+ \not{E}_T + jets$ and $3l^+ + \not{E}_T + jets$ where l can be an electron, muon or leptonically decaying τ and we consider hadronically decaying τs as jets. In the final states above we require exactly (and not at least) the number of leptons mentioned. While the $l+ \not{E}_T + jets$ channel would be the discovery mode with the highest cross-section a simultaneous observation of a signal in the other more striking channels, $l^+l^+ + \not{E}_T + jets$, $3l+ \not{E}_T + jets$ and $3l^+ + \not{E}_T + jets$, would provide confirmation that the phenomenon is indeed classicalization. The fact that missing energy must be present in these channels is an important difference from the black hole case where the probability of neutrino emission is small ($< 5\%$) and one can have final states with leptons and jets but no missing energy (this is the final state discussed in Ref. [33] for instance). As we said earlier, when we go to higher N_* values channels with even more leptons will become important.

The production cross-section for classicalons, however, decreases as N_* increases because of the falling longitudinal W luminosity in Eq.(2.50).[5] We will, therefore, not study channels with larger number of leptons. The production cross-section for

[5]As we will soon see, another issue for channels with greater number of leptons is that there is a greater reduction in cross-section for these channels when experimental requirements like lepton isolation are taken into account.

classicalons is given in Table 2.1 for $M_* = 246$ GeV and $M_* = 600$ GeV and LHC energies 7 and 14 TeV. We have provided contributions only for $N_* \geq 6$.[6] Using the branching ratios evaluated in the previous section, we give in Table 2.1 the cross-sections of the four channels, l, l^+l^+, $3l$ and $3l^+$, that we are interested in. For the $3l$ channel there are two different ways in which three leptons can be produced, from three Ws or from the decay of a W and Z. In Table 2.1 we provide the individual contribution from both these channels as these two modes can be experimentally distinguished by checking if a lepton pair reconstructs the Z-mass. Also, the number of partonic jets is higher for the $WZ \rightarrow 3l$ mode than the $3W \rightarrow 3l$ mode. The number of partonic jets in an event is maximum if all the Zs that do not decay leptonically, decay hadronically (and not invisibly) and all the Ws decay to quarks pairs and not to τ-jets. In Table 2.1 we have given in square brackets for $N_* = 6$ and $N_* = 7$, the cross-section values assuming the maximum possible number of jets are produced. As one can see from these values for $N_* = 6$ and $N_* = 7$ about half of the time the classicalon does decay to the maximum number of jets possible.

The number of jets produced is very large and this ensures that the background is negligible. Including the two forward jets produced in the WBF process, for $N_* = 6(10)$ as many as 12 (20) partonic jets in the single lepton channel, 10 (18) partonic jets in the l^+l^+ and $3l$ channels, and 8 (16) partonic jets in the $3l^+$ channel, can be produced. In Fig. 5.6 we add up contribution from classicalons with $N_* \geq 6$ and show the inclusive cross-section for l plus at least 12 partonic jets, l^+l^+ plus at least 10 partonic jets, $3l$ plus at least 10 partonic jets and the cross-section for the $3l^+ + \not{E}_T + jets$ channel. We do not require a minimum number of jets in the last

---

[6]The energy regime close to the classicalization scale that we have not considered, that is $\sqrt{\hat{s}} \sim M_*$ and $N < 6$, would phenomenologically resemble strong electroweak symmetry breaking (EWSB) theories like technicolor with the appearance of quantum resonances at this scale. Final states with as many as five final W/Zs have already been mentioned in the literature as signatures for strong EWSB [44].

case as the background is absent even without this requirement.[7] Whereas the $3l^+$ channel is virtually background free (the background cross-section is of the order of 0.01 fb at 14 TeV LHC [45]) the other channels also have negligible background if we require so many jets. The $l+\ \not{E}_T + jets$ background gets its major contribution from the $t\bar{t}+jets$ production and for more than 10 jets the background, with appropriate cuts, is negligible [46]. The $l^+l^++\ \not{E}_T + jets$ background has been discussed in detail in Ref. [47] and Ref. [48] and again cuts can be applied to reduce this background to a negligible value for high jet multiplicities (8 or more jets). As all the major SM processes that contribute $3l+\ \not{E}_T + jets$ background, like the $WZ + jets$ process, would also contribute to the single lepton channel, if the $l+\ \not{E}_T + jets$ background is negligible, this background can also be neglected at high jet multiplicities.

It should be noted that the cross-section values in Table 2.1 and Fig. 5.6 do not include any effect of parton showering, experimental cuts or detector acceptances. Let us discuss the important experimental effects not taken into account here. The experimental cut that is expected to have a substantial effect in the presence of so many jets is the requirement for lepton isolation. For instance if we consider 15 partonic jets having a cone radius $\Delta R = \sqrt{\Delta \eta^2 + \Delta \phi^2} = 0.4$, we can roughly estimate the fraction of times an isotropically emitted lepton would remain isolated by finding the fraction of area of in $\eta - \phi$ space that is still unoccupied by the jets assuming conservatively that the jets do not overlap. To take into account the fact that the leptons and jets are produced centrally we limit their η-range to $-1.5 < \eta < 1.5$, which gives a total allowed area $\Delta \eta \Delta \phi = 6\pi$. This estimate gives us about 60% probability that a lepton would be isolated for 15 non-overlapping

---

[7]For evaluation of the exclusive contribution to the cross-section of $l + 12\ jets$ from $N_* = 6$ classicalon decays, $l^+l^+ + 10\ jets$ from $N_* = 6$ classicalon decays, $(WZ \to 3l) + 10\ jets$ from $N_* = 6$ classicalon decays and $(3W \to 3l) + 10\ jets$ from $N_* = 7$ classicalon decays we have to use the cross-section values allowing no invisible decays of the Z boson and no tau decays of W bosons, as such decays would lead to fewer jets than the required number. Decay of two or more Zs invisibly is relatively unlikely and has been ignored here.
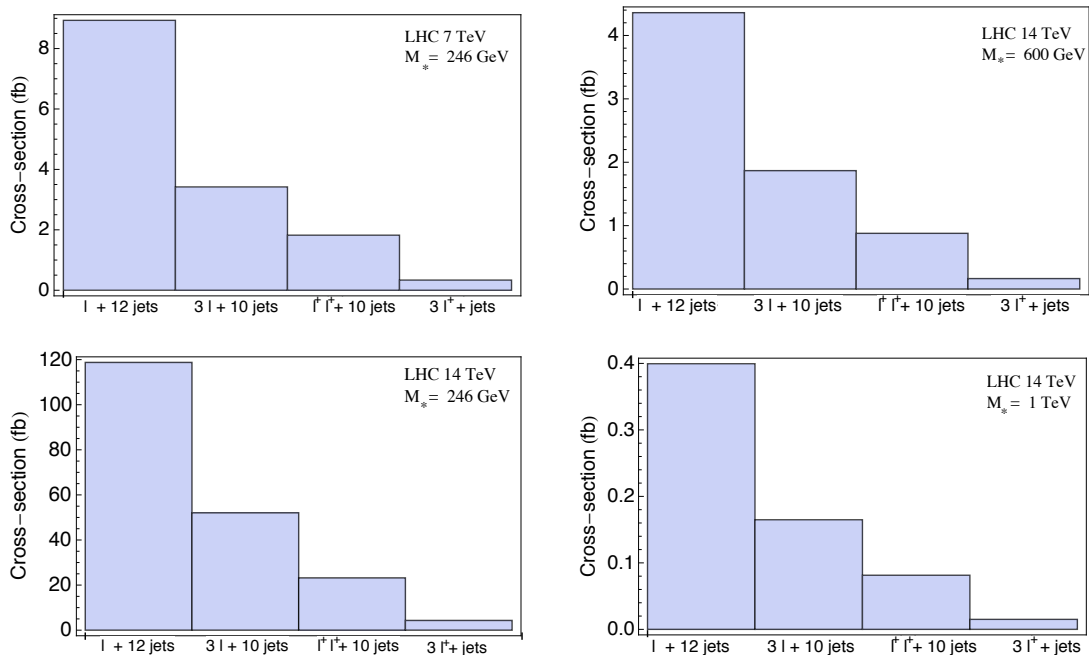
Figure 2.6: Cross-section for production of a lepton plus at least 12 partonic jets, two same sign leptons plus at least 10 partonic jets, three leptons plus at least 10 partonic jets and for three same sign leptons from the decay of classicalons formed by longitudinal Ws and Zs. Missing transverse energy is present in all the cases mentioned above and the number of leptons mentioned in each case is the exact number of leptons in the final state. Note that the number of jets mentioned above is at the partonic level and no effect of showering, hadronization, experimental cuts or detector acceptances has been included here. For a discussion of these effects see the text.

jets. It should also be kept in mind that that the lepton identification rate is about 90% [49]. Thus, this estimate tells us, due to the requirement of all the leptons being isolated and getting identified, the cross-section would be reduced to about 54% of the theoretical value in the $l + \not{E}_T + jets$ channel, to about 29% of the theoretical value in the $l^+ l^+ + \not{E}_T + jets$ channel and to about 16% of the theoretical value in the channels with three leptons. At the same time, the $3l$ ($l^+ l^+$) channel would contribute about 35%(50%) of the time to the single lepton channel when not all but only two (one) of the leptons are lost due to lepton isolation/identification requirements. A similar contribution from the $3l$ channel to the $l^+ l^+$ channel would be relatively small. As the leptons are produced isotropically, p_T and η cuts are not expected to have a big effect. Now we come to the experimental cuts related to the

jets. A limitation of our analysis that it has been carried out at the partonic level only. Whereas the number of jets would increase from the number at the partonic level because of parton showering, other experimental effects like p_T and η cuts and most importantly the jet isolation cut requiring a minimum ΔR separation between any two jets, would decrease the number of jets from the partonic level. The ΔR cut is important because if the number of jets is very large and it is likely for two or more partonic jets to merge thus reducing the number of jets experimentally observed. The number of jets produced in a classicalon decay is so large, however, that even after a possible reduction due to the above factors we would expect many jets. Finally, an experimental cut requiring a minimum missing transverse energy should not reduce the signal cross-section appreciably.

Keeping these issues in mind we see from Fig. 5.6 that whereas for $M_* = 246$ GeV, classicalization should be seen in the $l+ \not{E}_T + jets$ channel (with hints seen in the other channels also) in the present run of the LHC with about 10 fb^{-1} data, a thorough confirmation with observation in all the channels would require data at 14 TeV. On the other hand for $M_* = 600$ GeV about 10 fb^{-1} data at 14 TeV would be needed for both discovery and confirmation in the different channels. The cross-section for $M_* = 1$ TeV is about ten times smaller than that for $M_* = 600$ GeV and this is the maximum classicalization scale that can be probed with about 100 fb^{-1} LHC data at 14 TeV.

Another important measurement would be the dependence of N_* on the total energy of the decay products shown in Fig. 2.4 (left). It is theoretically equivalent to measure the average energy of a lepton/partonic jet, $M/(2N_*)$, in the classicalon rest frame[8] as a function of the total invariant mass. Experimentally, however, the

---

[8]The typical energy measured in the lab frame would not be so different from the typical energy in the classicalon rest frame because we expect, as is the case in black hole production [32], that the classicalons produced would not be highly boosted.

average energy of a lepton/partonic jet is a more tractable quantity than the total multiplicity as it is not affected even if there is missing energy. We plot the average energy of a lepton/partonic jet as a function of the mass in Fig. 2.4 (right). We see that the average energy decreases very gradually. As far as leptons are concerned it should be straightforward to measure the typical energy. An interesting feature to be checked would be that the typical lepton energy should be same in all the different channels $l + \not{E}_T + jets$, $l^+ l^+ \not{E}_T + jets$, $3l + \not{E}_T + jets$ and $3l^+ + \not{E}_T + jets$. To find the typical energy of a jet in an event as a function of the total energy and confirming that this is same as the typical lepton energy would be much more complicated. This is again because the energy of a jet at the partonic level is not the same as the final energy measured in the detector. The typical jet energy would decrease due to parton showering and increase if two jets get merged. Another error in the measurement would come from the fact that two of the jets in the event would be the WBF jets which would not have the typical energy in Fig. 2.4, but this would not be a large effect because of the large number of jets present. Simulations including parton showers, hadronization and jet algorithms are needed in order to trace back the energy at the partonic level from the final energy measured in the detectors.

2.3.2 Higgs as the classicalizer

The second application of classicalization we want to consider is a model where the classicalizing field is the Higgs itself and the classicalons (called Higgsions in this case) are configurations of the Higgs field. The motivation for this model comes from the hierarchy problem. Indeed, the radiative corrections to the Higgs mass in this model are screened by the classization scale itself and not by the highest possible UV scale. In other words, the loop contributions to the Higgs mass get classicalized and cut-off at the classicalization scale M_*. As the biggest contribution to the Higgs

mass comes from the top, the top loop must get classicalized at the lowest scale, that is for the Higgs mass to be natural we must have,

$$(2.51) \qquad \frac{y_t}{16\pi^2}M_*^2 \sim m_h^2$$

where M_* is the classicalization scale. This gives the condition $M_* \lesssim 4\pi m_h$. We will consider the case where only the right handed top has a classicalizing interaction of the form,

$$(2.52) \qquad \frac{\kappa}{M_*^2}(\Phi^\dagger\Phi)\bar{t}_R\partial_\mu t_R,$$

Φ being the SM Higgs doublet. It is reasonable to consider the possibility of a universal classicalization scale for all SM particles, in which case Higgsions would be produced at low scales directly from the light quarks. This scenario, however, would be far more constrained by existing flavor and LHC data. Here we will consider the minimal case required for naturalness with only the right handed top having a low scale classicalizing interaction. In this case the radius of the classicalon is given by the expression [18],

$$(2.53) \qquad r_* \sim \frac{\kappa v M}{M_*^3} \text{ for } \kappa > 0$$

$$(2.54) \qquad r_* \sim \frac{\kappa M}{M_*^2} \text{ for } \kappa < 0$$

where v is the Higgs VEV. Again the above relationships is valid only until r_* reaches the compton wavelength of the Higgs, $1/m_h$ and beyond this point the radius freezes at the value $1/m_h$ [18]. Again we will absorb any numerical coefficient present in the above expressions for r_* and also the numerical value of κ in a redefinition of M_* to obtain,

$$(2.55) \qquad r_* = \frac{v M}{M_*^3} \text{ for } \kappa > 0$$

$$(2.56) \qquad r_* = \frac{M}{M_*^2} \text{ for } \kappa < 0.$$
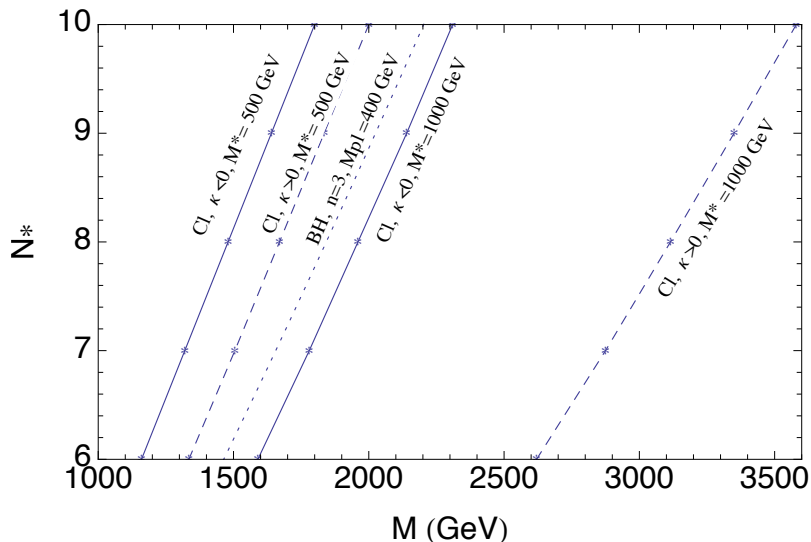
Figure 2.7: In the model with Higgs as the classicalizer we plot the number of Higgs bosons produced, N_*, in a classicalon decay as a function of the classicalon mass and compare it with the multiplicity curve for a black hole in $n = 3$ extra dimensions with $M_{pl} = 400$ GeV.

Again, experimental constraints due to quantum resonances around M_* are unfortunately incalculable.

The number of quanta is again found using Eqs.(2.41) and (2.42) using the same value for the normalization factor, γ, given in Eq.(2.44). We take $m_H = 130$ GeV here and in the rest of this section. We plot the number of quanta as a function of the classicalon mass in Fig. 2.7 for the two different choices, $M_* = 500$ GeV and $M_* = 1$ TeV for both positive and negative κ. The curves are again almost linear as in the previous case of goldstone classicalization. We also show for comparison the N_* vs M curve for a black hole in $n = 3$ extra dimensions with $M_{pl} = 400$ GeV. Once again, for comparison with the black hole multiplicity, it must be kept in mind that the final decay multiplicity, in the classicalon case, is bigger than N_*, the number of Higgs bosons, as the Higgs bosons decay further to leptons and jets.

We will consider the possibility of producing Higgsions in the top fusion process $gg \rightarrow (t\bar{t} \rightarrow Cl)t\bar{t}$ (see Fig. 2.8). To find the cross-section for classicalon production form top fusion we introduce a dimension-5 $tthh$ operator in CALCHEP [50],

N_*	Branching ratio to $l+$ jets(%)	Cross-section for $\kappa < 0$			Cross-section for $\kappa > 0$		
		M (GeV)	All channels (fb)	$l+$ jets(fb)	M (GeV)	All channels (fb)	$l+$ jets(fb)
$M_* = 500$ GeV							
6	29	1160	26(0.5)	7.5(0.2)	1335	8.4(0.08)	2.4(0.03)
7	26	1320	17(0.3)	4.4(0.08)	1505	5.4(0.04)	1.4(0.01)
8	23	1480	13(0.2)	3.0(0.05)	1670	4.0(0.01)	0.9(-)
9	21	1640	8.0(0.1)	1.7(0.02)	1835	3.2(0.01)	0.7(-)
10	18	1800	6.0(0.06)	1.1(0.01)	2000	2.1(-)	0.4(-)
Total cross-section:			70(1.2)	18(0.4)		23(0.1)	5.8(0.04)
$M_* = 1$ TeV							
6	29	1590	1.0	0.3	2620	0.02	-
7	26	1780	0.6	0.2	2875	0.01	-
8	23	1960	0.4	0.09	3115	0.01	-
9	21	2140	0.2	0.04	3350	-	-
10	18	2310	0.2	0.04	3580	-	-
Total cross-section:			2.4	0.7		0.04	-

Table 2.2: Cross-section for classicalon production by top fusion in the model with the Higgs as the classicalizer. We give the total cross-section as well as the cross-section for only the $l+jets$ channel. We have considered the cases $M_* = 500$ GeV and $M_* = 1$ TeV. The cross-sections for 7 TeV LHC energy, when not negligible (<0.01 fb), are given in parentheses. All other numbers are for 14 TeV LHC energy. For evaluating the branching ratio to the $l+jets$ channel we have used the SM numbers for $m_H = 130$ GeV, that is, $BR(H \to q\bar{q}) = 0.55$, $BR(H \to gg) = 0.06$, $BR(H \to \tau\tau) = 0.05$, $BR(H \to WW) = 0.29$ and $BR(H \to ZZ) = 0.04$. We have considered hadronically decaying τs to be jets and leptonically decaying τs to be leptons. Note that no effect of showering, hadronization, experimental cuts or detector acceptances has been included here. For a discussion of these, see the text.
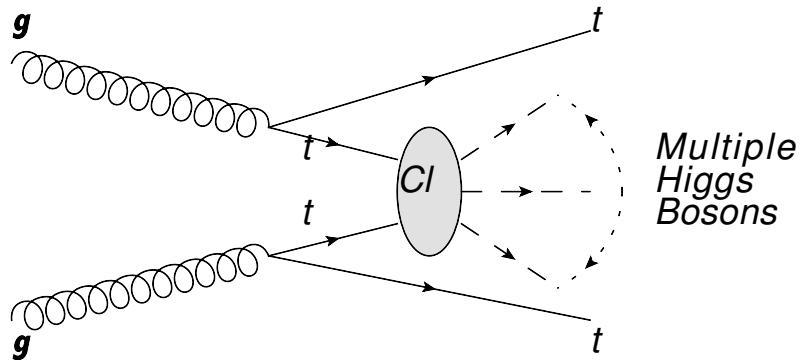
Figure 2.8: Production of a classicalon by weak boson fusion process in the model with goldstone classicalization.

$(\bar{t}tH^\dagger H/\Lambda)$ and find the cross-section for the top fusion process $pp \to gg \to t\bar{t}hh$. At high energies the $tt \to hh$ cross-section due to this operator is a constant as a function of the $t\bar{t}$-energy; this is also true for production of N_*-particle classicalons $(tt \to Cl)$ the cross-section in this case being fixed at $\pi r_*^2(M_{N_*})$. Thus we find the cross-section of the top fusion process $pp \to gg \to t\bar{t}hh$ (taking into account only the contribution of the $tthh$ operator and not other SM processes) and rescale this cross-section by the ratio of the $t\bar{t} \to Cl$ cross-section to the $tt \to hh$ cross-section to obtain the $pp \to gg \to t\bar{t} + Cl$ cross-section. Finally we would have to multiply by a factor of $1/2$ as the $tt \to Cl$ process would take place only if both the tops are right handed whereas for the $tt \to hh$ process to take place the tops need to have opposite chiralities. Note that we are assuming that the total cross-section can be factorized into a hard part and $(t\bar{t} \to Cl)$ and a 'top parton density function (PDF)' and this is not expected to be accurate unless the partonic center of mass energy $\sqrt{\hat{s}} \gg m_t$. For this reason our cross-section estimates would be approximate.

We show the results for the cross-sections for $M_* = 500$ GeV and $M_* = 1$ TeV in Table 2.2. We also give branching ratios and cross-sections for the $l + \not{E}_T + jets$ channel (again requiring exactly, and not at least, one lepton) where the lepton comes from a real or virtual W boson emerging form either a Higgs or one of the final

tops (decay channels with greater number of leptons have a much smaller branching fraction in this case). Again, unlike black holes, missing energy must necessarily be present in this channel. The number of jets is even larger here and a classicalon with $N_* = 6$ would give rise to about 16 jets including the jets from the top decays, so that the background is again negligible [46]. A similar estimate to the one done in the previous subsection tells us that for 16 jets at least about 50% of the theoretical cross-section should survive after the lepton identification and isolation requirements are taken into account. It is clear from Table 2.2 that discovery would not be possible in the 7 TeV run of the LHC. For $M_* = 500$ GeV discovery should be possible with about 10 fb^{-1} at 14 TeV LHC energy for both the $\kappa < 0$ and $\kappa > 0$ cases. Much higher integrated luminosities, about 100 fb^{-1}, would be required for $M_* = 1$ TeV and $\kappa < 0$ whereas the $\kappa > 0$ case would be out of reach even with high luminosities.

2.4 Conclusions

In this chapter we have argued that classicalons must have analogs of thermodynamic properties and we have carried out a model-independent statistical mechanical analysis of classicalons. By taking the set of four momenta of the incoming (outgoing) particles that form a classicalon (that a classicalon decays to) as a microstate of the classicalon, we count the number of such microstates imposing only the condition of energy-momentum conservation and the condition that the incoming wave-packets should be able to localize their energy inside the classicalon radius, r_*. We find that the particles a classicalon decays to will have a Planck distribution with an effective temperature $T \sim 1/r_*$ in the case of a massless classicalizer field. The final thermodynamic relations obeyed by a classicalon are different from those obeyed by an ideal relativistic Bose gas in spite of the fact that both have the same distribution

function. This is because incoming/outgoing wave-packets in a classicalon forma-
tion/decay process have a different density of states than the particles in an ideal
gas. Our results confirm the expectations of Ref. [25] and we find the entropy scales
like, $S \sim N_* \sim Mr_*$, when the classicalizer field is massless. This implies that clas-
sicalon decays to a few particles should be combinatorially suppressed by a factor
$e^{-S} \sim e^{-N_*}$. For the specific case of a black hole, the classicalon radius is propor-
tional to its mass, and the well known proportionality of the black hole entropy to
its area follows from the general scaling of the classicalon entropy.

We use our results, in particular the computation of the number of classicalon
decay products, N_*, to make LHC predictions. For computing the rate of production,
we use the fact that classicalons are expected to be produced with a geometric cross-
section, πr_*^2. The important difference from black hole production is that even at
energies higher than the classicalization scale, other SM processes involving particles
without a strong classicalizing interaction go on unaffected with a larger cross-section
than classicalon production. In the models we consider, light quarks have no direct
classicalizing interactions and, as a result, the classicalon production cross-sections
are much smaller than black hole production cross-sections at the same energy. On
the other hand, we find the multiplicity of final decay products of the classicalons to
be larger than the decay multiplicity of extra-dimensional black holes, in the cases
we consider.

The first model we look at is a model where longitudinal WW scattering is uni-
tarized in the absence of a Higgs by classicalization of longitudinal Ws and Zs. The
classicalon in this model decays to multiple Ws and Zs which lead to signals in var-
ious channels like $l + \not{E}_T + jets$, $l^+ l^+ + \not{E}_T + jets$, $3l + \not{E}_T + jets$ and $3l^+ + \not{E}_T + jets$
where the number of partonic jets is typically larger than ten. Our results for the

different channels are well summarized in Fig. 5.6. We find that, for this model, discovery would be imminent in the $l + jets$ channel in the present 7 TeV run of the LHC, if the classicalization scale is as low as $M_* = v = 246$ GeV and that we would have to wait for about 10 fb^{-1} integrated lumiosity at 14 TeV, if the scale is higher, around $M_* = 600$ GeV. The maximum classicalization scale that can be probed with 100 fb^{-1} data at 14 TeV is about $M_* = 1$ TeV.

For the model to address the hierarchy problem with the Higgs itself as the classicalizer, we consider the minimal case where only the right handed top has a classicalizing interaction. The classicalon radius in this case depends on the sign of the non-renormalizable coupling κ. We explore the prospect of discovery of such classicalons in the top fusion process $gg \rightarrow (t\bar{t} \rightarrow Cl)t\bar{t}$ by looking at the $l + \not{E}_T + jets$ final state where the number of partonic jets is very high (at least 15). We find that for $M_* = 500$ GeV, discovery should be possible with about 10 fb^{-1} at 14 TeV LHC for both the $\kappa < 0$ and $\kappa > 0$ cases. For $M_* = 1$ TeV and $\kappa < 0$ much higher integrated luminosities, about 100 fb^{-1}, would be required whereas the $\kappa > 0$ case would be out of reach even with high luminosities if $M_* = 1$ TeV.

CHAPTER III

Higgs generations

3.1 Generations of Higgs Bosons

Chiral matter comes in three generations. The simplest hypotheses of electroweak symmetry breaking and fermion mass generation assumes the existence of one Higgs boson in the case of the Standard Model and a pair of Higgs bosons in the case of supersymmetry. We ask here what the consequences are of having more generations of Higgs bosons in analogy to fermion matter content. We are not the first to ask this question and investigate answers (see for eg. Refs. [51], [52] and [53]). Some of our discussion will be known to readers, but that is only to set the stage for describing further material we have developed and in particular detailing Large Hadron Collider (LHC) implications for next generation Higgs boson ideas that survive scrutiny.

The question is of increased interest of late for two reasons. One, the LHC has entered the prime real estate of Higgs boson phenomenology, and we should be prepared to discover all reasonable and viable ideas. The physical particle spectrum of the Higgs sector, if it exists, is speculation at present. Investigating various scenarios that may yield phenomenology that is different from the simplest Standard Model (SM) approach is needed in order to develop more interpretive power over the data when it comes.

A second reason to consider a next generation of Higgs bosons is from recent developments in string phenomenology. Some approaches to particle physics model building from string theory suggest that further copies of Higgs bosons may be generic among solutions. For example, in the work of [51] a second Higgs generation is generic among the heterotic vacua, and may even be more copious than single generation Higgs boson theories. It is also typical in this approach that there is a selection rule that allows only the first generation of Higgs bosons to couple to the fermions. We will review later why this aspect is very helpful for the viability of a next generation of Higgs bosons.

Next generation Higgs bosons are motivated in other theories as well. For example, in theories with branes at singularities bifundamental states come from the same quivers, and multiplicities of Higgs pairs are generic just like multiplicities of other representations. In intersecting D-brane theories, the chiral content is constrained by topological intersection numbers, but the vector-like states can be many-fold. Usually only our self-imposed restrictions in seeking solutions results in one generation. In heterotic orbifold models exotics are generic. Restrictions to three families of fermions rarely necessarily restricts Higgs bosons to one pair. Some approaches, such as Z_3 orbifolds with two Wilson lines [52], naturally provide three generations of Higgs bosons, for example.

Most physicists nowadays carry the vague suspicions that additional Higgs bosons are disastrous unless introduced into very restricted frameworks. They give the photon a mass, or result in unacceptable tree-level flavor changing neutral currents. This is to a large degree correct, but there are interesting viable limiting cases, touched on above, that are supported by theory model building. We set out to elucidate some general conditions for the viability of next generation Higgs bosons.

We detail a formalism for the analysis, including determining the mass matrices and mixing angles in both the SM and Supersymmetry. This culminates in a study of a key process at the LHC that is signal for next generation Higgs bosons.

3.2 Overcoming Tree-Level Flavor Changing Neutral Currents

Let us begin by considering an extra Higgs doublet Φ_{extra} that is added to the SM Higgs doublet Φ_{sm}. The vacuum expectation values (VEV) of each are $\langle\Phi\rangle = v_{sm}$ and $\langle\Phi_{extra}\rangle = v_{extra}$, subject to the condition that $v^2 = v_{sm}^2 + v_{extra}^2 = (246\,\text{GeV})^2$. We assume that both Higgs doublets couple to the SM fermions. From these two doublets, three degrees of freedom are eaten and become longitudinal components of $W_L^\pm$ and Z_L^0, and five degrees of freedom are left: the scalar mass eigenstates $\{H, h\}$, the pseudoscalar A, and the charged Higgs bosons $H^\pm$.

It is always possible to write the Yukawa Lagrangian terms as,

$$
\begin{aligned}
\mathcal{L}_Y = \; & \frac{\sqrt{2}m_i^U}{v}\delta_{ij}\bar{Q}_{iL}\tilde{\Phi}_{VEV}U_{jR} + \frac{\sqrt{2}m_i^D}{v}\delta_{ij}\bar{Q}_{iL}\Phi_{VEV}D_{jR} + \frac{\sqrt{2}m_i^E}{v}\delta_{ij}\bar{L}_{iL}\Phi_{VEV}E_{jR} \\
& + \sqrt{2}\,\xi_{ij}^U\bar{Q}_{iL}\tilde{\Phi}_\perp U_{jR} + \sqrt{2}\,\xi_{ij}^D\bar{Q}_{iL}\Phi_\perp D_{jR} + \sqrt{2}\,\xi_{ij}^E\bar{L}_{iL}\Phi_\perp E_{jR} + c.c.
\end{aligned}
$$

(3.1)

where E_i, U_i and D_i are mass eigenstates of leptons, up type and down type quarks and $\xi_{ij}^{U,D}$ are *a priori* arbitrary. The definition of Φ_{VEV} is the linear combination that contains the full VEV,

$$
\Phi_{VEV} = \frac{v_{extra}}{v}\Phi_{extra} + \frac{v_{sm}}{v}\Phi_{sm}, \text{ and}
$$
(3.2)

$$
\Phi_\perp = \frac{v_{extra}}{v}\Phi_{sm} - \frac{v_{sm}}{v}\Phi_{extra}
$$
(3.3)

is the perpendicular state with no VEV associated to it. In general, there is nothing to forbid the off-diagonal elements of $\xi_{ij}^{U,D,E}$ from being $\mathcal{O}(1)$. This is the origin of the tree-level Flavor Changing Neutral Curent (FCNC) problem of extra Higgs bosons.
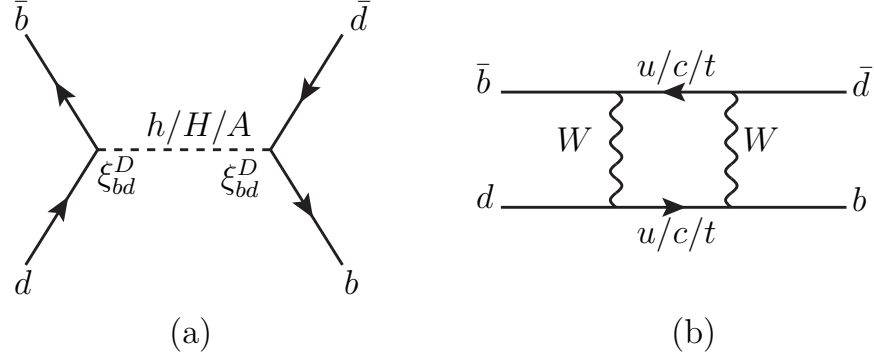
Figure 3.1: Flavor changing neutral current contributions to $B_d^0 - \bar{B}_d^0$ mixing from (a) Higgs exchange diagrams in an arbitrary 2HDM (there are also t-channel diagrams that we have not shown here), and (b) SM gauge contributions. Note that the SM diagrams are one-loop whereas the competing Higgs exchange is tree-level. Experiment is consistent with SM results, which implies severe constraints on the Higgs flavor-changing neutral current couplings $\xi_{ij}^F \ll 1$.

To estimate the experimental upper bound on the off diagonal elements of $\xi_{ij}^{U,D}$ let us assume that the matrices $\xi^{U,D}$ are real and symmetric. We then obtain the following Feynman rules for the scalar and pseudoscalar mass eigenstates (the vertex factor being $-i$ times the expressions below),

$$(3.4) \qquad H\bar{U}_i U_j, H\bar{D}_i D_j \;=\; c_{\alpha'} \frac{m_i^{U,D}}{v} \delta_{ij} + s_{\alpha'} \xi_{ij}^{U,D}$$

$$(3.5) \qquad h\bar{U}_i U_j, h\bar{D}_i D_j \;=\; -s_{\alpha'} \frac{m_i^{U,D}}{v} \delta_{ij} + c_{\alpha'} \xi_{ij}^{U,D}$$

$$(3.6) \qquad A\bar{U}_i U_j, A\bar{D}_i D_j \;=\; i\gamma_5 \xi_{ij}^{U,D}.$$

Here the mixing angle α' is the one that rotates from $\{\Phi_{VEV}, \Phi_\perp\}$ to the mass eigenstates $\{H, h\}$. The most stringent constraints on $\xi_{ij}^{U,D}$ come from $F^0 - \bar{F}^0$ mixing (where $F = K, B_d, D, B_s$). In a two-Higgs doublet model (2HDM) with arbitrary Yukawa couplings there is a tree-level contribution to the $F^0 - \bar{F}^0$ mass splitting because of diagrams like Fig. 3.1(a). For $\alpha' = 0$ using the expressions derived in [54]

Meson (quarks)	B_F	f_F (GeV)	ΔM_F^{expt} (GeV)
K^0 $(d\bar{s})$	$0.79 \pm 0.04 \pm 0.08$	0.159	$(3.476 \pm 0.006) \times 10^{-15}$ [55]
D^0 $(\bar{u}c)$	0.82 ± 0.01	0.165	$(0.95 \pm 0.37) \times 10^{-14}$
B_d^0 $(d\bar{b})$	$1.28 \pm 0.05 \pm 0.09$ [56]	0.216 ± 0.022	$(3.337 \pm 0.033) \times 10^{-13}$ [55]
B_s^0 $(s\bar{b})$	$-$	0.281 ± 0.021	$(117.0 \pm 0.8) \times 10^{-13}$ [55]

Table 3.1: Data associated with the neutral mesons K^0, B_d^0 and D^0. Values have been obtained from [3] unless mentioned otherwise. The value in the last row and third column is actually the value of the product $f_{B_s}\sqrt{B_{B_s}}$.

we get in the vacuum insertion approximation,

$$(3.7) \qquad M_F \Delta M_F = \xi_{ij}^{U,D\,2} \left(s_{\alpha'}^2 \frac{S_F}{m_H^2} + c_{\alpha'}^2 \frac{S_F}{m_h^2} - \frac{P_F}{m_A^2} \right)$$

where,

$$(3.8) \qquad S_F = \frac{B_F f_F^2 M_F^2}{6} \left(1 + \frac{M_F^2}{(m_i + m_j)^2} \right)$$

$$(3.9) \qquad P_F = -\frac{B_F f_F^2 M_F^2}{6} \left(1 + \frac{11 M_F^2}{(m_i + m_j)^2} \right).$$

Here M_F is the mass of the meson, m_H, m_h and m_A are the masses of H, h and A, f_F is the pseudoscalar decay constant and B_F is the B-parameter of the vacuum insertion approximation defined in [54]. We present the values of these parameters and the experimental values for ΔM_F in Table 3.1.

The Cheng-Sher ansatz [57] is sometimes assumed for the flavor changing couplings,

$$(3.10) \qquad \xi_{ij}^{U,D,E} = \lambda_{ij}^{U,D,E} \frac{\sqrt{m_i m_j}}{v},$$

as many approaches to flavor model building would give rise to it. Let us now find the maximum allowed value of $\xi_{ij}^{U/D}$ consistent with the experimental data and simultaneously determine the corresponding $\lambda_{ij}^{U/D}$. For B_d^0 and B_s^0 we use the SM predictions from lattice QCD, $\Delta M_{B_d}^{SM} = (4.5 \pm 1.0) \times 10^{-13}$ GeV [58] and $\Delta M_{B_s}^{SM} = (135 \pm 20) \times 10^{-13}$ GeV [3] and add the theoretical error in quadrature to the experimental error. To find the upper bound on ξ_{db}^D and ξ_{sb}^D we demand that

the sum of the SM value and the 2HDM contribution from Eq. (3.7) does not exceed the experimental value in Table 3.1 by more than two standard deviations. In obtaining the upper bounds on ξ_{ds}^D and ξ_{uc}^U we require that just the 2HDM contribution from Eq. (3.7) does not exceed the experimetal value in Table 3.1 by more than two standard deviations. Taking $m_H = m_h = m_A = 120$ GeV we find,

$$(3.11) \qquad \xi_{ds}^D \lesssim 1 \times 10^{-5} \ \lambda_{ds}^D \lesssim 0.1$$

$$(3.12) \qquad \xi_{uc}^D \lesssim 3 \times 10^{-5} \ \lambda_{uc}^D \lesssim 0.2$$

$$(3.13) \qquad \xi_{db}^D \lesssim 4 \times 10^{-5} \ \lambda_{db}^D \lesssim 0.06$$

$$(3.14) \qquad \xi_{sb}^D \lesssim 2 \times 10^{-4} \ \lambda_{sb}^D \lesssim 0.06.$$

The upper bounds stated above have an uncertainty due to the uncertainty in the value of $f_F \sqrt{B_F}$. From Eq. (3.7) we can see that a 10% uncertainty in $f_F \sqrt{B_F}$ would translate to a 10% uncertainty in the upper bound. Greater precision in lattice estimates of the SM values is required for more stringent constraints on $\xi_{ij}^{U/D}$ from $F^0 - \bar{F}^0$ mixing.

Future measurement of branching ratios of rare B decay modes such as $B(\bar{B}_s \to \mu^+ \mu^-)$ at LHCb is another way effects of the flavor changing couplings ξ_{bs}^D and ξ_{sb}^D may be discovered. Expressions for this branching ratio in the SM, and the Higgs contribution in a 2HDM with arbitray Yukawa couplings, can be found in Ref. [59]. The SM value is $(3.51 \pm 0.50) \times 10^{-9}$ [59] and the current Tevatron upper bound at 95% CL is 5.8×10^{-8} [60]. As LHCb would reach the sensitivity to measure the SM value [61], we can estimate the kind of upper bounds LHCb experiments would put on ξ_{bs}^D and ξ_{sb}^D by demanding that the Higgs contribution to this braching ratio is less than the SM value. Assuming again that ξ_{bs}^D and ξ_{sb}^D are real and equal to each

other, and that $\xi_{ij} = \lambda_{ij}\sqrt{m_i m_j}/v$, we obtain

$$(3.15) \qquad \lambda_{sb}^D \;\lesssim\; 2\,\frac{(m_A/120\text{ GeV})^2}{\lambda_{\mu\mu}^E} \quad \text{(Tevatron inferred bound)}$$

$$(3.16) \qquad \lambda_{sb}^D \;\lesssim\; 0.6\,\frac{(m_A/120\text{ GeV})^2}{\lambda_{\mu\mu}^E} \quad \text{(LHCb expected sensitivity)}.$$

Although this limit from Tevatron and future sensitivity expectations at LHCb do not appear to be as powerful as meson-meson mixing constraints, the uncertainty in what $\lambda_{\mu\mu}^E$ might be in the presence of next generation Higgs bosons suggests that it should stay under consideration. For a more thorough discussion of $B_s^0 - \bar{B}_s^0$ mixing constraints and the processes $\bar{B}_s \to \mu^+\mu^-, \bar{B}_d \to \bar{K}\mu^+\mu^-$ see Ref. [59]. For a discussion on the constraints on the diagonal couplings ξ_{ii}^F see Ref. [62].

We have seen above that the off-diagonal couplings ξ_{ij}^F are required to be extremely small in order to satisfy FCNC constraints. There is a general class of solutions to this problem [9] while admitting the existence of extra Higgs bosons in the spectrum. Tree-level FCNCs do not arise if Higgs boson interactions with the fermions take the form

$$\Delta\mathcal{L}_f = y_{ij}^D \bar{Q}'_{iL}\, F_d(\{\Phi_k\})\, D'_{jR} + y_{ij}^U \bar{Q}'_{iL}\, F_u(\{\Phi_k\})\, U'_{jR} + y_{ij}^E \bar{L}'_{iL}\, F_e(\{\Phi_k\})\, E'_{jR} + c.c.$$

$$(3.17)$$

where all the quark fields are gauge eigenstates. $F_{u,d,e}(\{\Phi_k\})$ are functions of Higgs fields $\{\Phi_k\}$, constrained only by the requirements that they are independent of the fermionic flavor indices i, j and that F_u transforms like an $SU(2)_L$ doublet with hypercharge $-1/2$, and F_d and F_e transform like $SU(2)_L$ doublets with hypercharge $1/2$.

The generalized form of Eq. (3.17) subsumes many ideas already present in the literature. For example, the SM Higgs sector is $F_u = H_{SM}^c$ and $F_d = F_e = H_{SM}$.

The type II [63] 2HDM [8] is $F_u = H_u$ and $F_d = F_e = H_d$. The type I 2HDM [8] is $F_u = \Phi_1^c$ and $F_d = F_e = \Phi_1$ with an additional Φ_2 that does not couple to fermions. The leptophilic Higgs model of Ref. [64] is $F_u = \phi_q^c$, $F_d = \phi_q$ and $F_e = \phi_l$.

There are an infinite variety of models that can satisfy Eq. (3.17). However, principles are expected to be at work to fall into this class if there is more than one Higgs boson. In the case of supersymmetry, the type II structure follows from holomorphy of the superpotential. In the case of type I theories, it is usually assumed that the second Higgs has, for example, a discrete Z_2 symmetry $\Phi_2 = -\Phi_2$ that forbids its direct coupling to fermions whereas Φ_1 does not.

The summary point is that a next generation Higgs boson is unlikely to satisfy FCNC currents due to tree-level mediated interactions unless a principle is invoked the ensures that it will satisfy the condition of Eq. (3.17). The most straightforward principle that we can invoke, and one that has been nicely illustrated recently in the model of [51], is a selection rule that forbids the next generation Higgs boson from coupling to fermions.

3.3   Next Generation Higgs bosons of Supersymmetry

We begin with a discussion of next generation Higgs bosons in supersymmetry. In minimal supersymmetry there are already two Higgs doublets present in the spectrum. In unrestricted field theory, two Higgs doublets with arbitrary couplings are a disaster for flavor changing neutral currents. However, as mentioned above, supersymmetric theories have the special property that all superpotential operators must be holomorphic in the superfields. Thus, it is impossible to employ one Higgs field to give masses to both up-type fermions and down-type fermions. The introduction of the second Higgs doublet solves this problem, and holomorphy is the principle by

which tree-level FCNC's are held under control. The interaction lagrangian takes the form of the type II 2HDM in the form of Eq. (3.17). Of course, when supersymmetry is broken, non-holomorphic interactions can induce additional couplings leading ultimately to potentially interesting flavor changing neutral currents [65], but those are naturally small over much of parameter space.

If we wish to add more Higgs doublets to supersymmetry, we must do it in up- and down-Higgs boson pairs. This is in sympathy with adding a new generation – a new copy – of the $\{H_u, H_d\}$ pair. More importantly, it is required to straightforwardly satisfy anomaly constraints due to the presence of new fermions that are the super-partners of the Higgs bosons. When a next generation of Higgs doublets is added to the spectrum, holomorphy is no longer powerful enough to save us from tree-level FCNC. Additional Yukawa couplings generally create FCNC challenges [52, 62]. In Ref. [53] supersymmetric three generation Higgs models have been considered where an exact symmetry prevents the next generation Higgs Bosons from coupling to the fermions. They show that these next generation Higgs bosons would not couple to the standard Higgs bosons and under the assumption of equal scalar masses at unification scale they would not get VEVs, thus avoiding FCNC problems. In general the simplest way out of the FCNC challenge is to assume that the extra Higgs doublet pairs couple very weakly, or not at all, to the fermions. This is the assumption we shall adopt for now.

The result of the discussion above is that we are overlaying a type I Higgs structure to our type II supersymmetric theory. In other words, we are adding a Higgs boson pair that does not couple to the fermions on top of a Higgs pair that does. Our emphasis in this study is on the type I aspect (i.e., the next generation), and as such the supersymmetric type II feature is of less immediacy. Thus, we shall postpone

a detailed discussion of additional constraints to later, to the less complex model of adding one Higgs boson to the SM. Nevertheless, we wish to present the mass eigenstates and mixing, and in particular highlight what effect multiple Higgs bosons have on the mass of the lightest Higgs boson scalar of supersymmetry.

3.3.1 General Higgs Potential

For the supersymmetric two Higgs generation model (SUSY 2HGM), we consider two additional Higgs superfields H_{u2} and H_{d2} charged under $SU(2)_L \times U(1)_Y$ just as H_{u1}, H_{d1} respectively. The terms in the superpotential involving these superfields are,

$$(3.18) \qquad W = \mu_{11} H_{u1} H_{d1} + \mu_{12} H_{u1} H_{d2} + \mu_{21} H_{u2} H_{d1} + \mu_{22} H_{u2} H_{d2}.$$

From now on by $H_{u1}, H_{d1}, H_{u2}, H_{d2}$ we will denote only the scalar part of the superfields which have the components,

$$(3.19) \qquad H_{ui} = \begin{pmatrix} H_{ui}^+ \\ H_{ui}^0 \end{pmatrix} \quad H_{di} = \begin{pmatrix} H_{di}^0 \\ H_{di}^- \end{pmatrix}.$$

The D-terms are given by,

$$(3.20) \qquad D^a = -g \sum_i (H_{ui}^\dagger T^a H_{ui} + H_{di}^\dagger T^a H_{di}).$$

The D-term contribution to the potential is given by,

$$
\begin{aligned}
V_D \;=\;& \frac{1}{2} \sum_a D_a D_a \\
=\;& \lambda [\sum_i (|H_{ui}|^2 - |H_{di}|^2)]^2 + \frac{g^2}{2} (\sum_i |(H_{ui}^{+*} H_{ui}^0 + H_{di}^{0*} H_{di}^-)|^2 \\
& - \sum_i (|H_{ui}^0|^2 - |H_{di}^0|^2) \sum_j (|H_{uj}^+|^2 - |H_{dj}^-|^2)).
\end{aligned}
$$

(3.21)

where $\lambda = \frac{g^2 + g'^2}{8}$. Using the form of the superpotential in Eq. (3.18) we get the F-term contribution,

$$V_F = (|\mu_{11}|^2 + |\mu_{12}|^2)|H_{u1}|^2 + (|\mu_{22}|^2 + |\mu_{21}|^2)|H_{u2}|^2 + (|\mu_{11}|^2 + |\mu_{21}|^2)|H_{d1}|^2$$

(3.22)
$$+(|\mu_{22}|^2 + |\mu_{12}|^2)|H_{d2}|^2 + (a_u H_{u1}^\dagger H_{u2} + a_d H_{d1}^\dagger H_{d2} + c.c.)$$

where,

(3.23)
$$a_d = \mu_{11}^* \mu_{12} + \mu_{21}^* \mu_{22}$$

(3.24)
$$a_u = \mu_{11}^* \mu_{21} + \mu_{12}^* \mu_{22}.$$

In addition to the D-terms and F-terms there are the soft SUSY breaking terms,

$$V_{soft} = m_{u1}'^2 |H_{u1}|^2 + m_{u2}'^2 |H_{u2}|^2 + m_{d1}'^2 |H_{d1}|^2 + m_{d2}'^2 |H_{d2}|^2 + (b_{11} H_{u1} H_{d1} +$$

(3.25)
$$b_{12} H_{u1} H_{d2} + b_{21} H_{u2} H_{d1} + b_{22} H_{u2} H_{d2} + c.c.)$$

where $H_{ui} H_{dj} = H_{ui}^+ H_{dj}^- - H_{ui}^0 H_{dj}^0$.

Adding all the terms from Eq. (3.21), (3.22) and (3.25) we get finally,

$$
\begin{aligned}
V &= V_D + V_F + V_{soft} \\
&= m_{u1}^2 |H_{u1}|^2 + m_{u2}^2 |H_{u2}|^2 + m_{d1}^2 |H_{d1}|^2 + m_{d2}^2 |H_{d2}|^2 \\
&\quad + (a_u H_{u1}^\dagger H_{u2} + a_d H_{d1}^\dagger H_{d2} + c.c.) \\
&\quad + (b_{11} H_{u1} H_{d1} + b_{12} H_{u1} H_{d2} + b_{21} H_{u2} H_{d1} + b_{22} H_{u2} H_{d2} + c.c.) \\
&\quad + \lambda[\sum_i (|H_{ui}|^2 - |H_{di}|^2)]^2 + \frac{g^2}{2}(\sum_i |(H_{ui}^{+*} H_{ui}^0 + H_{di}^{0*} H_{di}^-)|^2 \\
&\quad - \sum_i (|H_{ui}^0|^2 - |H_{di}^0|^2) \sum_j (|H_{uj}^+|^2 - |H_{dj}^-|^2)).
\end{aligned}
$$

(3.26)

Here m_i^2 is the sum of $m_i'^2$ and the F-term contribution from Eq. (3.22). All the couplings are required to be real by hermiticity with the exception of the bilinear

couplings b_{ij} and a_i which are in general complex. By redefining the phases of the doublets H_{u1}, H_{d2} and H_{u2} only three of these six couplings can be chosen to be real so that the theory is in general CP violating.

Note that we are allowing $H_{u1,d1}$ to mix arbitrarily with $H_{u2,d2}$ in the Higgs potential only. Some mixing between the two generations is necessary as we do not want to have a global symmetry under which the next generation Higgs bosons can be rotated with respect to the first generation because this would lead to the presence of a massless Goldstone boson. When it comes to interacting with the fermions, as discussed before and emphasized again later, next generation Higgs bosons are generally barred from having couplings unlike the first generation Higgs bosons.

3.3.2 Electroweak symmetry breaking and scalar mass matrices

We put $\langle H_{ui}^+ \rangle = \langle H_{di}^- \rangle = 0$, $\langle H_i^0 \rangle = \frac{1}{\sqrt{2}} v_i$ and demand that the first derivatives of the potential with respect to the fields H_i^0 vanish to obtain,

$$(3.27) \qquad m_{d1}^2 - \tilde{b}_{11}\frac{v_{u1}}{v_{d1}} - \tilde{b}_{21}\frac{v_{u2}}{v_{d1}} + \tilde{a}_d\frac{v_{d2}}{v_{d1}} + \lambda(\sum_j v_{dj}^2 - \sum_j v_{uj}^2) = 0$$

$$(3.28) \qquad m_{u1}^2 - \tilde{b}_{11}\frac{v_{d1}}{v_{u1}} - \tilde{b}_{12}\frac{v_{d2}}{v_{u1}} + \tilde{a}_u\frac{v_{u2}}{v_{u1}} - \lambda(\sum_j v_{dj}^2 - \sum_j v_{uj}^2) = 0$$

$$(3.29) \qquad m_{d2}^2 - \tilde{b}_{22}\frac{v_{u2}}{v_{d2}} - \tilde{b}_{12}\frac{v_{u1}}{v_{d2}} + \tilde{a}_d\frac{v_{d1}}{v_{d2}} + \lambda(\sum_j v_{dj}^2 - \sum_j v_{uj}^2) = 0$$

$$(3.30) \qquad m_{u2}^2 - \tilde{b}_{22}\frac{v_{d2}}{v_{u2}} - \tilde{b}_{21}\frac{v_{d1}}{v_{u2}} + \tilde{a}_u\frac{v_{u1}}{v_{u2}} - \lambda(\sum_j v_{dj}^2 - \sum_j v_{uj}^2) = 0.$$

Here $\tilde{b}_{ij} = \text{Re } b_{ij}$ and $\tilde{a}_i = \text{Re } a_i$. It is necessary that $\langle H_{ui}^+ \rangle = \langle H_{di}^- \rangle = 0$ for electromagnetism to remain unbroken. We can always choose one of the charged fields, say H_{d1}^- to have an expectation value $\langle H_{d1}^- \rangle = 0$ using the $SU(2)_L$ gauge freedom.

To ensure that $\langle H_{u1}^+ \rangle = \langle H_{d2}^- \rangle = \langle H_{u2}^+ \rangle = 0$ is consistent with the minimization conditions, however, we must demand that in addition to eqs. (3.27)-(3.30) the second derivatives of the potential with respect to the charged fields at this point are positive. This is equivalent to demanding that the masses of the three physical charged Higgs bosons are positive.

Also note that we have assumed the VEV of the neutral components v_{ui}, v_{di} to be real and positive. One of the VEVs say, v_{d1}, can be chosen to be real and positive using the $U(1)_Y$ gauge freedom. As we discussed earlier this theory is in general CP violating therefore we can choose the other VEVs v_{u1}, v_{u2} and v_{d1} to be real and positive simply by a convenient choice of phases of the respective doublet fields. These phases can then be absorbed in the bilinear couplings b_{ij} and a_i and a redefinition of the quark fields. If the underlying theory ensures that all the bilinear couplings b_{ij} and a_i are real so that the Lagrangian conserves CP, in order to avoid spontaneous CP violation v_{u1}, v_{u2} and v_{d1} must be real too. Therefore the point $\langle A_{u1} \rangle = \langle A_{d2} \rangle = \langle A_{u2} \rangle = 0$ must be a minima where $A_i = \sqrt{2}\, \text{Im}\, (H_i^0)$. For this, in addition to eqs. (3.27)-(3.30) the second derivatives of the potential with respect to the pseudoscalar fields A_i must be positive also at this point. This is equivalent to demanding that the three physical pseudoscalars in the theory must have positive masses. Once v_{u1}, v_{u2} and v_{d1} are known to be real they can always be chosen to be positive by a convenient choice of signs of the respective doublet fields, which can then be absorbed in the the bilinear couplings b_{ij} and a_i and a redefinition of the quark fields. If b_{ij} and a_i are complex the CP even states mix with the pseudoscalar states. To avoid this unnecessary complication to our present purposes we will present below the mass matrices assuming that the b_{ij} and a_i are real.

Using eqs. (3.27)-(3.30) we can eliminate the m_i^2. We can find the mass matrix of

the four CP-even scalars and the four pseudoscalars by substituting $H_i^0 = \frac{1}{\sqrt{2}}(v_i + h_i + iA_i)$. The mass matrix for the CP-even scalars, $\mathcal{M}_H^2$, in the $\{d_1, u_1, d_2, u_2\}$ basis is,

$$
\begin{pmatrix}
m_{H11}^2 & -b_{11} - 2\lambda v_{u1}v_{d1} & a_d + 2\lambda v_{d1}v_{d2} & -b_{21} - 2\lambda v_{u2}v_{d1} \\
-b_{11} - 2\lambda v_{u1}v_{d1} & m_{H22}^2 & -b_{12} - 2\lambda v_{u1}v_{d2} & a_u + 2\lambda v_{u1}v_{u2} \\
a_d + 2\lambda v_{d1}v_{d2} & -b_{12} - 2\lambda v_{u1}v_{d2} & m_{H33}^2 & -b_{22} - 2\lambda v_{u2}v_{d2} \\
-b_{21} - 2\lambda v_{u2}v_{d1} & a_u + 2\lambda v_{u1}v_{u2} & -b_{22} - 2\lambda v_{u2}v_{d2} & m_{H44}^2
\end{pmatrix}
$$

where,

$$
\begin{aligned}
m_{H11}^2 &= b_{11}\frac{v_{u1}}{v_{d1}} + b_{21}\frac{v_{u2}}{v_{d1}} - a_d\frac{v_{d2}}{v_{d1}} + 2\lambda v_{d1}^2 \\
m_{H22}^2 &= b_{11}\frac{v_{d1}}{v_{u1}} + b_{12}\frac{v_{d2}}{v_{u1}} - a_u\frac{v_{u2}}{v_{u1}} + 2\lambda v_{u1}^2 \\
m_{H33}^2 &= b_{12}\frac{v_{u1}}{v_{d2}} + b_{22}\frac{v_{u2}}{v_{d2}} - a_d\frac{v_{d1}}{v_{d2}} + 2\lambda v_{d2}^2 \\
m_{H44}^2 &= b_{21}\frac{v_{d1}}{v_{u2}} + b_{22}\frac{v_{d2}}{v_{u2}} - a_u\frac{v_{u1}}{v_{u2}} + 2\lambda v_{u2}^2.
\end{aligned}
$$

The pseudoscalar mass matrix, $\mathcal{M}_A^2$, in the $\{d_1, u_1, d_2, u_2\}$ basis is,

$$
\begin{pmatrix}
m_{A11}^2 & b_{11} & a_d & b_{21} \\
b_{11} & m_{A22}^2 & b_{12} & a_u \\
a_d & b_{12} & m_{A33}^2 & b_{22} \\
b_{21} & a_u & b_{22} & m_{A44}^2
\end{pmatrix}
$$

where,

$$
\begin{aligned}
m_{A11}^2 &= b_{11}\frac{v_{u1}}{v_{d1}} + b_{21}\frac{v_{u2}}{v_{d1}} - a_d\frac{v_{d2}}{v_{d1}} \\
m_{A22}^2 &= b_{11}\frac{v_{d1}}{v_{u1}} + b_{12}\frac{v_{d2}}{v_{u1}} - a_u\frac{v_{u2}}{v_{u1}} \\
m_{A33}^2 &= b_{12}\frac{v_{u1}}{v_{d2}} + b_{22}\frac{v_{u2}}{v_{d2}} - a_d\frac{v_{d1}}{v_{d2}} \\
m_{A44}^2 &= b_{21}\frac{v_{d1}}{v_{u2}} + b_{22}\frac{v_{d2}}{v_{u2}} - a_u\frac{v_{u1}}{v_{u2}}.
\end{aligned}
$$

The charged Higgs mass matrix differs from the pseudoscalar mass matrix only due to the last term in the potential in Eq. (3.26). In the basis $\left\{ H_{d1}^{-*}, H_{u1}^{+}, H_{d2}^{-*}, H_{u2}^{+} \right\}$,

$$\mathcal{M}_+^2 = \mathcal{M}_A^2 + \frac{g^2}{4} \begin{pmatrix} v_{u1}^2 + v_{u2}^2 - v_{d2}^2 & v_{d1}v_{u1} & v_{d1}v_{d2} & v_{d1}v_{u2} \\ v_{u1}v_{d1} & v_{d1}^2 + v_{d2}^2 - v_{u2}^2 & v_{u1}v_{d2} & v_{u1}v_{u2} \\ v_{d2}v_{d1} & v_{d2}v_{u1} & v_{u1}^2 + v_{u2}^2 - v_{d1}^2 & v_{d2}v_{u2} \\ v_{u2}v_{d1} & v_{u2}v_{u1} & v_{u2}v_{d2} & v_{d1}^2 + v_{d2}^2 - v_{u1}^2 \end{pmatrix}.$$

3.3.3 Upper bound on the mass of the lightest CP even Higgs

We want to transform the mass matrices above to the Runge basis which is defined as follows. One of the basis vectors in the Runge basis is,

$$(3.31) \qquad \vec{V}_1 = v_{d1}/v \ H_{d1}^c + v_{u1}/v \ H_{u1} + v_{d2}/v \ H_{d2}^c + v_{u2}/v \ H_{u2}.$$

Here $v = \sqrt{v_{u1}^2 + v_{d1}^2 + v_{u2}^2 + v_{d2}^2}$. H_{di}^c is in the $SU(2)_L$ conjugate representation and is given by,

$$(3.32) \qquad H_{di}^c = \begin{pmatrix} -H_{di}^- \\ H_{di}^{0*} \end{pmatrix}.$$

We choose the other basis vectors so that they are orthogonal to this vector and to each other. The simplest choices for two of the basis vectors are,

$$\begin{aligned} \vec{V}_2 &= v_{u1}/v_1 \ H_{d1}^c - v_{d1}/v_1 \ H_{u1} \\ (3.33) \qquad \vec{V}_3 &= v_{u2}/v_2 \ H_{d2}^c - v_{d2}/v_2 \ H_{u2} \end{aligned}$$

where $v_1 = \sqrt{v_{u1}^2 + v_{d1}^2}$ and $v_2 = \sqrt{v_{u2}^2 + v_{d2}^2}$. We can find the fourth basis vector which is orthogonal to the first three by the expression,

$$\begin{aligned} \vec{V'}_4 &= (\vec{V}_1.\vec{U})\vec{V}_1 + (\vec{V}_2.\vec{U})\vec{V}_2 + (\vec{V}_3.\vec{U})\vec{V}_3 - \vec{U} \\ (3.34) \qquad \vec{V}_4 &= \frac{\vec{V'}_4}{\sqrt{\vec{V'}_4.\vec{V'}_4}} \end{aligned}$$
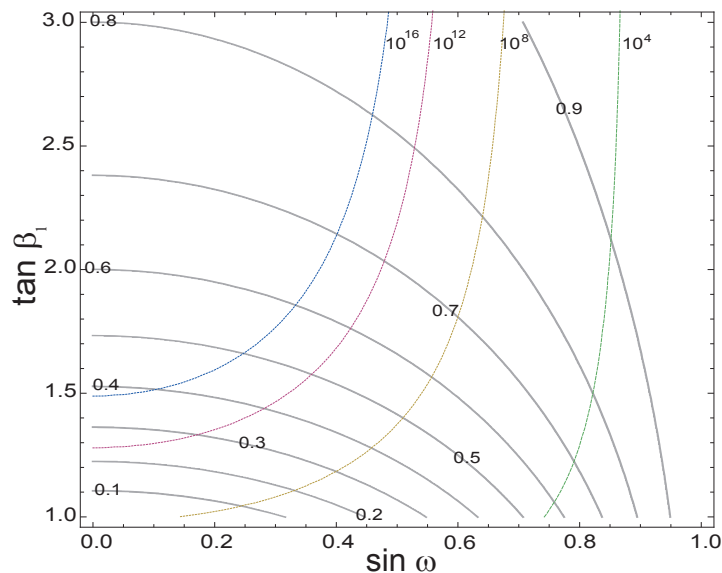
Figure 3.2: Contours of the upper bound on the mass of the lightest Higgs (in M_Z units) in the SUSY 2HGM taking $\cos 2\beta_2 = -1$. We have also shown contours of equal Λ_{SC} (in GeV), the energy scale at which the top Yukawa coupling λ_t becomes larger than 4π. Details about the calculation of Λ_{SC} appear in Section 3.5.

where $\vec{U}$ can be any arbitrary vector. The transformation matrix is an $SO(4)$ rotation matrix,

$$(3.35) \qquad\qquad R = (\vec{V_1}\ \vec{V_2}\ \vec{V_3}\ \vec{V_4}).$$

In the Runge basis, the mass matrices of the pseudoscalar, charged Higgs and CP-even scalar Higgs boson masses take on special form. For the pseudoscalar and charged Higgs mass matrix, the first row and first column contain all zeros, which is expected since the first basis vector V_1 is the "electroweak VEV multiplet" which has all the VEV. Thus, the CP-odd and charged components of the first basis vector in the Runge basis are the spin-zero Goldstone boson states absorbed by the Z_L^0, W_L^+, and W_L^- vector bosons. What remains is one more component of a full doublet, namely the CP-even part. We shall write the full CP-even mass matrix below and identify the matrix element corresponding to the mass of this CP even scalar and

comment on its meaning.

The CP even mass matrix in the Runge basis is,

$$(3.36) \qquad \mathcal{M}_H^{'2} = R^T \mathcal{M}_H^2 R.$$

We get $\mathcal{M}_H^{'2} =$

$$\begin{pmatrix} \frac{2\lambda(\sum_i(v_{di}^2-v_{ui}^2))^2}{v^2} & \frac{4\lambda v_{d1}v_{u1}\sum_i(v_{di}^2-v_{ui}^2)}{v_1 v} & \frac{4\lambda v_{d2}v_{u2}\sum_i(v_{di}^2-v_{ui}^2)}{v_2 v} & \frac{4\lambda(v_{u2}^2 v_{d1}^2-v_{u1}^2 v_{d2}^2)\sum_i(v_{di}^2-v_{ui}^2)}{v_1 v_2 v^2} \\ \frac{4\lambda v_{d1}v_{u1}\sum_i(v_{di}^2-v_{ui}^2)}{v_1 v} & m_{H22}^{'2} & m_{H23}^{'2} & m_{H24}^{'2} \\ \frac{4\lambda v_{d2}v_{u2}\sum_i(v_{di}^2-v_{ui}^2)}{v_2 v} & m_{H23}^{'2} & m_{H33}^{'2} & m_{H34}^{'2} \\ \frac{4\lambda(v_{u2}^2 v_{d1}^2-v_{u1}^2 v_{d2}^2)\sum_i(v_{di}^2-v_{ui}^2)}{v_1 v_2 v^2} & m_{H24}^{'2} & m_{H34}^{'2} & m_{H44}^{'2} \end{pmatrix}$$

where,

$$m_{H22}^{'2} = \frac{8\lambda(v_{u1}v_{d1})^3 + b_{11}v_1^4 + b_{21}v_{u1}^3 v_{u2} - a_u v_{d1}^3 v_{u1} - a_d v_{u1}^3 v_{d2} + b_{12}v_{d1}^3 v_{d2}}{v_1^2 v_{u1} v_{d1}}$$

$$m_{H23}^{'2} = \frac{a_d v_{u1}v_{u2} + b_{12}v_{d1}v_{u2} + b_{21}v_{u1}v_{d2} + a_u v_{d1}v_{d2} + 8\lambda v_{u1}v_{u2}v_{d2}}{v_1 v_2}$$

$$m_{H24}^{'2} = \frac{v^2(b_{21}v_{u1}v_{u2} + a_u v_{d1}v_{u2} - a_d v_{u1}v_{d2} - b_{12}v_{d1}v_{d2}) + 8\lambda(v_{u1}v_{d1}^3 v_{u2}^2 - v_{u1}^3 v_{d1}v_{d2}^2)}{v v_1^2 v_2}$$

$$m_{H33}^{'2} = \frac{8\lambda(v_{u2}v_{d2})^3 + b_{22}v_2^4 + b_{21}v_{d1}v_{d2}^3 - a_u v_{u1}v_{d2}^3 - a_d v_{d1}v_{u2}^3 + b_{12}v_{u1}v_{u2}^3}{v_2^2 v_{u2} v_{d2}}$$

$$m_{H34}^{'2} = \frac{v^2(b_{21}v_{d1}v_{d2} - a_u v_{u1}v_{d2} + a_d v_{d1}v_{u2} - b_{12}v_{u1}v_{u2}) + 8\lambda(v_{d1}^2 v_{u2}^3 v_{d2} - v_{u1}^2 v_{u2}v_{d2}^3)}{v v_1 v_2^2}$$

$$m_{H44}^{'2} = \frac{v^4(b_{21}v_{d1}v_{u2} - a_u v_{u1}v_{u2} + b_{12}v_{u1}v_{d2} - a_d v_{d1}v_{d2}) + 8\lambda(v_{d1}^2 v_{u2}^2 - v_{u1}^2 v_{d2}^2)^2}{v^2 v_1^2 v_2^2}.$$

The Runge basis helps us see what the lightest Higgs boson mass becomes in the limit that supersymmetry breaking masses are large, $\tilde{m} \gg M_Z$. In that case, the {11} element of the CP even Higgs boson mass matrix is the only diagonal element that stays small. A theorem of linear algebra tells us that the smallest eigenvalue of a positive definite matrix is smaller than the smallest diagonal element. Therefore, at tree-level we know from this {11} element the upper bound on the mass of the

lightest CP even Higgs h, which is[1]

$$m_h^2 \leq \frac{2\lambda(\sum_i(v_{di}^2 - v_{ui}^2))^2}{v^2}$$

(3.37) $$\Rightarrow m_h \leq M_Z|\cos^2\omega\cos 2\beta_1 + \sin^2\omega\cos 2\beta_2|,$$

where $\tan\beta_i \equiv v_{ui}/v_{di}$ and $\tan\omega \equiv v_2/v_1$.

The leading supersymmetry breaking corrections to this expression are from top squark loops in the same manner as found in the Minimal Supersymmetric Standard Model (MSSM). Thus, the controlling difference between our theory and the MSSM prediction for the Higgs mass is the tree-level expression of Eq. (3.37) compared to that of the MSSM, which is

(3.38) $$m_h \leq M_Z|\cos 2\beta|.$$

One sees that if we set $\tan\beta_1 = \tan\beta$, which becomes in both theories the fixed value for the ratio of VEVs of the two Higgs doublets that couple to the fermions, a small additional contribution can be made to the Higgs boson mass in our next generation Higgs theory compared to the MSSM by allowing for larger $\tan\beta_2 > \tan\beta_1 = \tan\beta$.

The available gain to the Higgs boson mass in this manner is tiny if $\tan\beta_1 \gtrsim 5$. For lower values of $\tan\beta_1$ the additional Higgs doublet pair contributions can be significant if the mixing angle ω is larger. This may be useful since it is a challenge in the MSSM to obtain a Higgs boson mass above the $114\,\mathrm{GeV}$ experimental limit without having too-high superpartner masses that induce fine-tuning in the electroweak sector potential.

In Fig. 3.2 we plot contours of the tree-level Higgs boson mass in units of M_Z in the plane of $\tan\beta_1$ vs. $\sin\omega$, assuming that $\cos 2\beta_2 = -1$, which is a good approx-

---

[1]Note that such an upper bound would exist even if our assumption that b_{ij} and a_i are real is not true. For complex b_{ij} and a_i the CP even and pseudoscalar states mix. There are again seven neutral scalars and a Goldstone boson. The 7×7 mass matrix of the physical scalars would again have $\frac{2\lambda(\sum_i(v_{di}^2 - v_{ui}^2))^2}{v^2}$ as the {11} element in the seven dimensional basis in which V_1 is the Runge vector. Here the Runge vector in the original eight dimensional space is $V_1^T = \frac{1}{v}(v_1, v_2, v_3, v_4, 0, 0, 0, 0)$.

$\sin\omega$	$\tilde{m}_t$ (TeV)	Λ_{SC} (GeV)
0	2.7	2×10^{16}
0.5	2.0	5×10^{8}
0.7	1.4	3×10^{5}
0.9	0.8	2×10^{3}

Table 3.2: For various values of $\sin\omega$ we show the value of $\tilde{m}_t$ needed to raise the Higgs boson mass above the experimental limit of $114\,\mathrm{GeV}$ and also the scale Λ_{SC} where the top Yukawa coupling diverges. The tree-level contribution is obtained by assuming $\tan\beta_1 = 1.5$ and $\cos 2\beta_2 = -1$.

imation if $\tan\beta_2 \gtrsim 5$. One sees that as $\sin\omega$ increases, the second Higgs doublet is more responsible for electroweak symmetry breaking and therefore the Higgs mass increases due to larger $\tan\beta_2$. The drawback is that the Higgs bosons that couple to the fermions get smaller VEVs, leading to larger Yukawa couplings. The larger top Yukawa coupling could diverge at a low scale. We describe this effect in more detail in Section 3.5. In Fig. 3.2 we have also plotted, therefore, the contours of the scale Λ_{SC} at which the top Yukawa coupling becomes strongly interacting (i.e., diverges). In Table 3.2 we show that with increasing $\sin\omega$ mixing angle, it is possible to have a smaller value of the stop masses so that that the Higgs boson mass is greater than $114\,\mathrm{GeV}$. The quoted values of $\tilde{m}_t \equiv \sqrt{\tilde{m}_{t_1}\tilde{m}_{t_2}}$ are obtained by assuming that the tree-level contributions are derived from $\tan\beta_1 = 1.5$ and $\cos 2\beta_2 = -1$, and that only the leading order radiative correction is contributing to the Higgs boson mass,

$$(3.39) \qquad \Delta m_h^2 = \frac{3}{2\pi^2}\frac{m_t^4}{v^2}\log\left(\frac{\tilde{m}_{t_1}\tilde{m}_{t_2}}{m_t^2}\right).$$

For higher values of $\sin\omega$, the tree-level contribution increases, thereby putting less pressure on the stop masses to raise the Higgs boson mass above $114\,\mathrm{GeV}$. This is clear from the values in the table, where for higher $\sin\omega$ the needed $\tilde{m}_t$ values are lower.

We also show in Table 3.2 the scale Λ_{SC} at which the top Yukawa coupling diverges for the various values of $\sin\omega$. As is expected, the larger the value of $\sin\omega$ for some given $\tan\beta_1$, the lower the Λ_{SC} scale. This is the tradeoff one has between

a larger Higgs mass prediction and a lower scale of top quark Yukawa coupling divergence. This is reminiscent of the Next-to-Minimal Supersymmetric Standard model (NMSSM) which can have an arbitrarily large Higgs boson mass by adjusting the parameter λ in the superpotential interaction $\lambda N H_u H_d$; however, large values of λ imply divergences well below a putative unification scale. This is a common feature in many attempts to solve the Higgs mass bound challenge of supersymmetry.

3.4 Next Generation Higgs boson of Standard Model

3.4.1 Electroweak symmetry breaking and scalar mass matrices

To add a next generation Higgs boson to the SM is equivalent to postulating a 2HDM with two scalar doublets Φ_1 and Φ_2 having hypercharge $1/2$. Earlier we discussed the many ways that a second Higgs boson can be added to the spectrum without being incompatible with experiment. There are many options, including type I models and type II models and variants on that theme. The type II structure is most naturally incorporated within supersymmetry using holomorphy as the guiding principle, as we discussed in the previous section. Going beyond that, the most straightforward way to incorporate extra Higgs doublets is to implement a type I structure. In other words, the second Higgs boson (or next full generation) induces no tree-level FCNC by virtue of it having no Yukawa couplings with the SM fermions.

To ensure no couplings of the second Higgs boson to fermions, the discrete symmetry,

$$(3.40) \qquad\qquad \Phi_2 \to -\Phi_2.$$

can be imposed, for example. If we allow a soft violation of this symmetry by dimension-two terms we can still avoid tree level FCNC bounds. The most general renormalizable potential for the scalars in which the discrete symmetry is softly

broken only by dimension-two terms is,

$$V(\Phi_1, \Phi_2) = \mu_1^2|\Phi_1|^2 + \mu^2|\Phi_2|^2 + b(\Phi_1^\dagger\Phi_2 + c.c.) + \lambda_1|\Phi_1|^4 + \lambda_2|\Phi_2|^4$$

(3.41)
$$+\lambda_3|\Phi_1|^2|\Phi_2|^2 + \lambda_4(\Phi_2^\dagger\Phi_1)(\Phi_1^\dagger\Phi_2) + \left[\frac{\lambda_5}{2}(\Phi_1^\dagger\Phi_2)^2 + c.c.\right].$$

The potential above is the potential in the toy model of [51] once the singlet in their theory gets a VEV. Hermiticity requires all the coupling constants in the above potential to be real with the exception of b and λ_5. A convenient choice of the phase of Φ_2 will allow only one of the two couplings to be real so that the theory is CP violating in general. Note that if both b and λ_5 vanish the potential is invariant under a global $U(1)$ symmetry for Φ_2. Thus either b or λ_5 must be non-zero to prevent the pseudoscalar from being a massless Goldstone boson.

Two CP conserving limits of this potential have been considered in the literature [66]. The limit in which $b = 0$ has been called potential A (V_A) and the limit in which $\lambda_5 = 0$ has been called potential B (V_B). Let us now analyze in some detail the electroweak symmetry breaking (EWSB) pattern in these two limits[2].

Potential A: $b = 0, \lambda_5 \neq 0$

Potential A can be obtained by strictly imposing the discrete symmetry $\Phi_2 \to -\Phi_2$ which requires $b = 0$ in eq. (3.42),

$$V_A(\Phi_1, \Phi_2) = \mu_1^2|\Phi_1|^2 + \mu^2|\Phi_2|^2 + \lambda_1|\Phi_1|^4 + \lambda_2|\Phi_2|^4 + \lambda_3|\Phi_1|^2|\Phi_2|^2$$

(3.42)
$$+\lambda_4(\Phi_2^\dagger\Phi_1)(\Phi_1^\dagger\Phi_2) + \left[\frac{\lambda_5}{2}(\Phi_1^\dagger\Phi_2)^2 + c.c.\right].$$

Without loss of generality all the λ_i couplings are real. Hermiticity demands it for all λ_i except λ_5, which can always be rotated to real and chosen to be either positive or negative by making Φ_2 absorb its phase. For definiteness we choose $\lambda_5 \leq 0$ here.

---

[2]For a discussion about the vacuum structure and the possibility of spontaneous violation of CP and electromagnetism in more general 2HDMs see Ref. [67].

The potential must be bounded from below in all field directions. One can test for dangerous runaway directions by parameterizing field excursions arbitrarily large in value. The following field directions give us all the unbounded from below (UFB) constraints (see, e.g., [68]):

$$
\begin{array}{ccc}
\underline{\Phi_1^T, \Phi_2^T \text{ direction}} & & \underline{\text{UFB constraint}} \\[4pt]
(0, a), (0, 0) & & \lambda_1 > 0 \\[4pt]
(0, 0), (0, a) & & \lambda_2 > 0 \\[4pt]
(0, \lambda_2^{1/4} a), (\lambda_1^{1/4} a, 0) & & \lambda_3 + 2\sqrt{\lambda_1 \lambda_2} > 0 \\[4pt]
(0, \lambda_2^{1/4} a), (0, \lambda_1^{1/4} a) & & \lambda_3 + \lambda_4 + \lambda_5 + 2\sqrt{\lambda_1 \lambda_2} > 0.
\end{array}
\tag{3.43}
$$

The most general vacuum expectations values for the two $\Phi_{1,2}$ Higgs fields can be expressed as (see, e.g., [69])

$$
\Phi_1 = \begin{pmatrix} 0 \\ v_1/\sqrt{2} \end{pmatrix}, \text{ and } \Phi_2 = \begin{pmatrix} u_2/\sqrt{2} \\ v_2 e^{i\xi}/\sqrt{2} \end{pmatrix}.
\tag{3.44}
$$

A non-zero u_2 would indicate the full breaking of $SU(2)_L \times U(1)_Y$, and in particular the photon would obtain mass. For electromagnetism to remain unbroken when Φ_1 and Φ_2 get VEVs the following condition must hold (see for instance [9, 69]),

$$
\lambda_4 + \lambda_5 < 0.
\tag{3.45}
$$

The minimization conditions obtained by setting $dV/d\phi_i = 0$ for all real fields ϕ_i defined in

$$
\Phi_1 = \begin{pmatrix} \phi_1 + i\phi_2 \\ \phi_3 + i\phi_4 \end{pmatrix}, \text{ and } \Phi_2 = \begin{pmatrix} \phi_5 + i\phi_6 \\ \phi_7 + i\phi_8 \end{pmatrix},
\tag{3.46}
$$

then ensure that EWSB is proper and the doublets get the VEVs,

$$
\Phi_1 = \begin{pmatrix} 0 \\ v_1/\sqrt{2} \end{pmatrix}, \text{ and } \Phi_2 = \begin{pmatrix} 0 \\ v_2/\sqrt{2} \end{pmatrix}
\tag{3.47}
$$

where $v_1 \geq 0$ and we can always choose $v_2 \geq 0$ by a convenient choice of sign of the doublet field Φ_2. The minimization conditions $dV/d\phi_3 = 0$ and $dV/d\phi_7 = 0$ given by [9, 69],

(3.48)
$$\phi_3 : \quad \mu_1^2 + \frac{\lambda_3+\lambda_4+\lambda_5}{2}v_2^2 + \lambda_1 v_1^2 = 0$$
$$\phi_7 : \quad \mu_2^2 + \frac{\lambda_3+\lambda_4+\lambda_5}{2}v_1^2 + \lambda_2 v_2^2 = 0$$

can be used to eliminate the parameters μ_1 and μ_2 [70].

We need to check if this solution is stable. To do that we require that the second derivative of the potential, i.e. the mass matrix, be positive definite. We can find the mass eigenvalues are by solving four 2×2 matrices. These matrices arise from $\phi_k \phi_{k+4}$ mixing for $k = 1, 2, 3, 4$. We simplify the entries in these matrices by substituting μ_1^2 and μ_2^2 from Eq. (3.48). To begin with, we look at the $\phi_1\phi_5$ and $\phi_2\phi_6$ mixings, which have the same 2×2 mass matrix:

(3.49)
$$\mathcal{M}^2_{\phi_1\phi_5} = \mathcal{M}^2_{\phi_2\phi_6} = \begin{pmatrix} -\frac{\lambda_4+\lambda_5}{2}v_2^2 & \frac{\lambda_4+\lambda_5}{2}v_1 v_2 \\ \frac{\lambda_4+\lambda_5}{2}v_1 v_2 & -\frac{\lambda_4+\lambda_5}{2}v_1^2 \end{pmatrix}$$

which leads to four eigenstates

(3.50)
$$m^2_{G^\pm} = 0 \text{ (charged Goldstone bosons)}$$

(3.51)
$$m^2_{H^\pm} = -\frac{\lambda_4 + \lambda_5}{2}(v_1^2 + v_2^2) \text{ (charged Higgs bosons)}.$$

The mixing angle is,

(3.52)
$$\tan \omega = \frac{v_2}{v_1}.$$

Now let us look at $\phi_4\phi_8$ mixing:

(3.53)
$$\mathcal{M}^2_{\phi_4\phi_8} = \begin{pmatrix} -\lambda_5 v_2^2 & \lambda_5 v_1 v_2 \\ \lambda_5 v_1 v_2 & -\lambda_5 v_1^2 \end{pmatrix}.$$
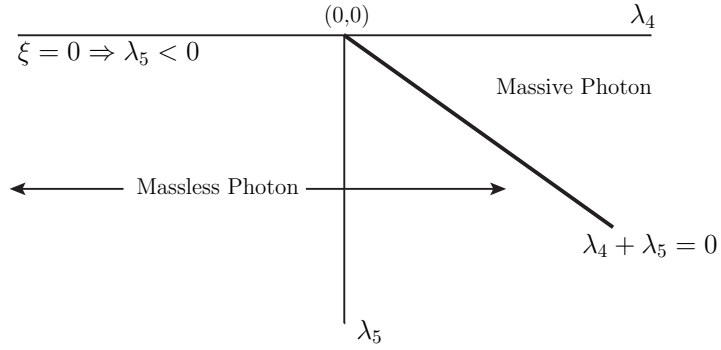
Figure 3.3: Parameter space for massive and massless photon in a type I 2HDM with potential A.

This leads to two eigenstates

$$
(3.54) \qquad m_G^2 \;=\; 0 \text{ (neutral Goldstone bosons)}
$$

$$
(3.55) \qquad m_A^2 \;=\; -\lambda_5(v_1^2 + v_2^2) \text{ (neutral pseudoscalar boson)}.
$$

The mixing angle is again $\tan\omega = v_2/v_1$. Finally, there is $\phi_3\phi_7$ mixing:

$$
(3.56) \qquad \mathcal{M}_{\phi_3\phi_7}^2 = \begin{pmatrix} 2\lambda_1 v_1^2 & (\lambda_3 + \lambda_4 + \lambda_5)v_1 v_2 \\ (\lambda_3 + \lambda_4 + \lambda_5)v_1 v_2 & 2\lambda_2 v_2^2 \end{pmatrix}.
$$

This is the 2×2 mass matrix for the two physical neutral scalar Higgs bosons of the theory, h and H. The mixing angle to rotate from $\{\phi_3, \phi_7\}$ basis to $\{H, h\}$ basis is usually called α, which is defined by convention to satisfy

$$
(3.57) \qquad \begin{pmatrix} H \\ h \end{pmatrix} = \begin{pmatrix} \cos\alpha & \sin\alpha \\ -\sin\alpha & \cos\alpha \end{pmatrix} \begin{pmatrix} \phi_3 \\ \phi_7 \end{pmatrix}.
$$

The solutions are obtained by simple eigenvalue, eigenvector analysis of the 2×2 matrix, and one obtains

$$
(3.58) \qquad \tan 2\alpha = \frac{\lambda_{345} v_1 v_2}{\lambda_1 v_1^2 - \lambda_2 v_2^2}
$$

where $\lambda_{345} = \lambda_3 + \lambda_4 + \lambda_5$. We will use the convention that H is the 'SM-like' Higgs and hence we will always take $\alpha < \pi/4$. The masses of the CP-even scalars are,

$$(3.59) \qquad m_{h,H}^2 = \lambda_1 v_1^2 + \lambda_2 v_2^2 \pm \sqrt{(\lambda_1 v_1^2 - \lambda_2 v_2^2)^2 + \lambda_{345} v_1 v_2^2}.$$

.

We require that the mass matrix be positive definite, which puts important constraints on the parameters of the theory. For example, from the charged Higgs and pseudo-scalar Higgs boson masses we know that

$$(3.60) \qquad \lambda_4 + \lambda_5 < 0, \text{ and } \lambda_5 < 0$$

is required. Note that the first condition is the same as Eq. (3.45), the condition that ensures that the photon remains massless. Fig. 3.3 plots the parameter space in the λ_4 vs. λ_5 plane that corresponds to massive photon and massless photon cases in agreement with Ref. [69].

Potential B: $\lambda_5 = 0$, $b \neq 0$

Potential B can be obtained by imposing a global $U(1)$ symmetry for Φ_2 and allowing it to be broken only softly by dimension-two terms like $b\Phi_1^\dagger \Phi_2$,

$$V(\Phi_1, \Phi_2) = \mu_1^2 |\Phi_1|^2 + \mu^2 |\Phi_2|^2 + b(\Phi_1^\dagger \Phi_2 + c.c.) + \lambda_1 |\Phi_1|^4 + \lambda_2 |\Phi_2|^4 + \lambda_3 |\Phi_1|^2 |\Phi_2|^2$$

$$(3.61) \qquad + \lambda_4 (\Phi_2^\dagger \Phi_1)(\Phi_1^\dagger \Phi_2).$$

Without loss of generality all the λ_i couplings are real due to hermiticity. The coupling b can be rotated to real by Φ_2 absorbing its phase.

The conditions for the potential to be bounded from below in all field directions are the same as Eq. (3.43) with $\lambda_5 = 0$ as these conditions are determined by the quartic couplings so that the additional bilinear term does not affect them. The

most general vacuum expectations values for the two $\Phi_{1,2}$ Higgs fields can again be expressed by Eq. (3.44).

The minimization condition $dV/d\phi_1 = 0$ [69] in this case is given by,

$$(3.62) \qquad\qquad bu_2 + \frac{\lambda_4}{2} u_2 v_1 v_2 \cos\xi = 0$$

It is clear that for

$$(3.63) \qquad\qquad b + \frac{\lambda_4}{2} v_1 v_2 \cos\xi \neq 0$$

it is required that $u_2 = 0$ from the ϕ_1 minimization condition in Eq. (3.62). This ensures that electromagnetism is not broken and the photon remains massless as the doublets get VEVs. This condition and the other minimization conditions then ensure that the doublets get VEVs of the form,

$$(3.64) \qquad\qquad \Phi_1 = \begin{pmatrix} 0 \\ v_1/\sqrt{2} \end{pmatrix}, \text{ and } \Phi_2 = \begin{pmatrix} 0 \\ v_2/\sqrt{2} \end{pmatrix}$$

where $v_1 \geq 0$ and we can always choose $v_2 \geq 0$ by a convenient choice of sign of the doublet field Φ_2, which can then be absorbed in a redefinition of the coupling b. The minimization conditions $dV/d\phi_3 = 0$ and $dV/d\phi_7 = 0$ given by [69],

$$(3.65) \qquad \begin{aligned} \phi_3: \quad & \mu_1^2 + b(v_2/v_1) + \tfrac{\lambda_3+\lambda_4}{2} v_2^2 + \lambda_1 v_1^2 = 0 \\ \phi_7: \quad & \mu_2^2 + b(v_1/v_2) + \tfrac{\lambda_3+\lambda_4}{2} v_1^2 + \lambda_2 v_2^2 = 0 \end{aligned}$$

can be used to eliminate the parameters μ_1 and μ_2 [70].

Let us now look at the mass matrix after substituting μ_1^2 and μ_2^2 from Eq. (3.65). Let us first look at the $\phi_1\phi_5$ and $\phi_2\phi_6$ mixings, which have the same 2×2 mass matrix:

$$(3.66) \qquad \mathcal{M}^2_{\phi_1\phi_5} = \mathcal{M}^2_{\phi_2\phi_6} = \begin{pmatrix} -\frac{\lambda_4}{2} v_2^2 - bv_2/v_1 & \frac{\lambda_4}{2} v_1 v_2 + b \\ \frac{\lambda_4}{2} v_1 v_2 + b & -\frac{\lambda_4}{2} v_1^2 - bv_1/v_2 \end{pmatrix}$$

which leads to four eigenstates

(3.67) $m_{G^\pm}^2 \;\; = \;\; 0$ (charged Goldstone bosons)

(3.68) $m_{H^\pm}^2 \;\; = \;\; -\dfrac{v_1^2 + v_2^2}{2}\left(\lambda_4 + \dfrac{2b}{v_1 v_2}\right)$ (charged Higgs bosons),

the mixing angle being,

(3.69) $$\tan\omega = \frac{v_2}{v_1}.$$

Now let us look at $\phi_4\phi_8$ mixing:

(3.70) $$\mathcal{M}_{\phi_4\phi_8}^2 = \begin{pmatrix} -bv_2/v_1 & b \\ b & -bv_1/v_2 \end{pmatrix}.$$

This leads to two eigenstates

(3.71) $m_{G^0}^2 \;\; = \;\; 0$ (neutral Goldstone boson)

(3.72) $m_A^2 \;\; = \;\; -\dfrac{b}{v_1 v_2}(v_1^2 + v_2^2)$ (neutral pseudoscalar boson),

where the mixing angle is again given by $\tan\omega = v_2/v_1$. Finally, there is $\phi_3\phi_7$ mixing:

(3.73) $$\mathcal{M}_{\phi_3\phi_7}^2 = \begin{pmatrix} 2\lambda_1 v^2 - bv_2/v_1 & (\lambda_3 + \lambda_4)v_1 v_2 + b \\ (\lambda_3 + \lambda_4)v_1 v_2 + b & 2\lambda_2 v_2^2 - bv_1/v_2 \end{pmatrix}.$$

We have again,

(3.74) $$\begin{pmatrix} H \\ h \end{pmatrix} = \begin{pmatrix} \cos\alpha & \sin\alpha \\ -\sin\alpha & \cos\alpha \end{pmatrix}\begin{pmatrix} \phi_3 \\ \phi_7 \end{pmatrix}.$$

The masses and mixing angle are,

(3.75) $$\tan 2\alpha = \frac{\lambda_{34} v_1 v_2 + b}{\lambda_1 v_1^2 - \lambda_2 v_2^2 + b\frac{v_1^2 - v_2^2}{2v_1 v_2}}$$

where $\lambda_{34} = \lambda_3 + \lambda_4$, and

(3.76)
$$m_{h,H}^2 = \lambda_1 v_1^2 + \lambda_2 v_2^2 - b\frac{v_1^2 + v_2^2}{2v_1 v_2} \pm \sqrt{\left(\lambda_1 v_1^2 - \lambda_2 v_2^2 + b\frac{v_1^2 - v_2^2}{2v_1 v_2}\right)^2 + (\lambda_{34} v_1 v_2 + b)^2}.$$
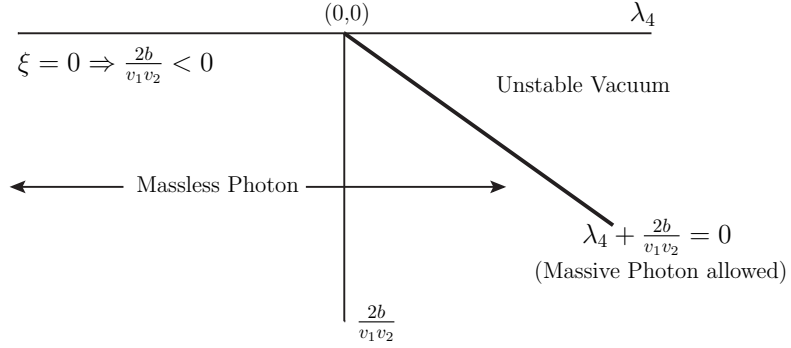
Figure 3.4: Parameter space for the different patterns of EWSB in the type I 2HDM with potential B.

Requiring the charged and pseudoscalar Higgs mass to be positive gives us,

$$(3.77) \qquad \lambda_4 + \frac{2b}{v_1 v_2} < 0 \quad \frac{2b}{v_1 v_2} < 0.$$

Fig. 3.4 shows the the regions in the parameter space which lead to the different patterns of EWSB for potential B.

An analysis of the general potential in Eq. (3.41) is complicated by the fact that both b and λ_5 cannot be chosen to be real by redefining the phase of Φ_2. This leads to a mixing between the pseudoscalar and CP even states. If both b and λ_5 are assumed to be real, however, the masses and mixing angles for the general potential in Eq. (3.41), assuming that the vacuum is invariant under CP and electromagnetism, are,

$$(3.78) \qquad m_{H^\pm}^2 = -\frac{v_1^2 + v_2^2}{2}\left(\lambda_4 + \lambda_5 + \frac{2b}{v_1 v_2}\right)$$

$$(3.79) \qquad m_A^2 = -(v_1^2 + v_2^2)\left(\lambda_5 + \frac{b}{v_1 v_2}\right)$$

$$(3.80) \quad m_{h,H}^2 = \lambda_1 v_1^2 + \lambda_2 v_2^2 - b\frac{v_1^2 + v_2^2}{2 v_1 v_2} \pm \sqrt{\left(\lambda_1 v_1^2 - \lambda_2 v_2^2 + b\frac{v_1^2 - v_2^2}{2 v_1 v_2}\right)^2 + \lambda_{345} v_1 v_2^2}$$

$$(3.81) \qquad \tan\omega = \frac{v_2}{v_1}$$
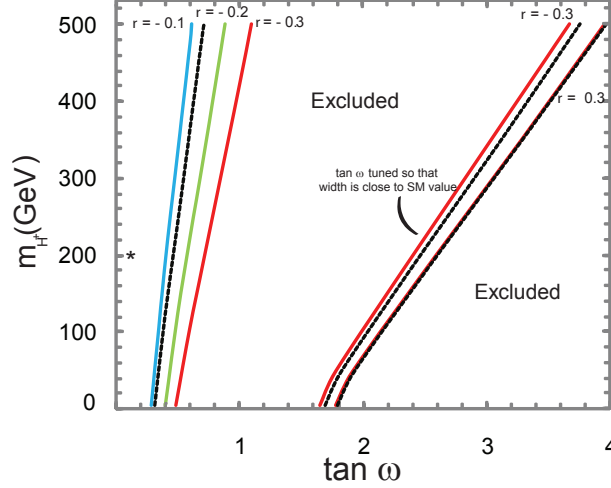
Figure 3.5: The solid lines show contours of constant r, the fractional deviation of the type I 2HDM value of the $b \to s\gamma$ width from the SM value. The dashed lines are the boundaries of the region in the m_{H^+}-$\tan\omega$ plane excluded by constraints from the $b \to s\gamma$ branching rate at two standard deviations. As one can see from Eq. (3.84) there are two different ways of satisfying the constraint: (1) if $\tan\omega$ is small the type I 2HDM width is close to the SM value, or (2) $\tan^2\omega$ can be tuned to a higher value so that $\left|\sum_{i=c,t} \lambda_i C_{7i}(m_b)\right|$ in Eq. (3.84) is close to the SM value ($C_{7i} \simeq -C_{7i}^{SM}$). Thus there are two disconnected allowed regions in Fig. 3.5. The star shows our choice of m_{H^+} and $\tan\omega$ that we use for collider simulations later.

$$(3.82) \qquad \tan 2\alpha = \frac{\lambda_{345} v_1 v_2 + b}{\lambda_1 v_1^2 - \lambda_2 v_2^2 + b\frac{v_1^2 - v_2^2}{2v_1 v_2}}$$

where $\lambda_{345} = \lambda_3 + \lambda_4 + \lambda_5$. Thus in 2HDMs from the original eight degrees of freedom we get three Goldstone bosons and five physical scalars. The Goldstone bosons are absorbed as longitudinal modes by $W^{+/-}$ and Z. The tree level masses of the $W^{+/-}$ and Z are,

$$(3.83) \qquad M_W = M_Z \cos\theta_W = \frac{g}{2}\sqrt{v_1^2 + v_2^2}.$$

We now give some of the constraints that this model experiences when requiring compatibility with all past experiment.

3.4.2 Indirect Constraints

Constraints due to virtual $H^{+/-}$ effects

In the type I 2HDM the coupling of $H^{+/-}$ to the fermions is proportional to $\tan\omega$. Thus in the type I 2HDM, unlike the type II 2HDM, all the constraints coming from processes involving virtual $H^{+/-}$ can be met for small enough $\tan\omega$. The strongest such constraint comes from the $b \to s\gamma$ branching rate. An expression for the width of the process in type I 2HDMs is [71],

$$\Gamma_{b\to s\gamma} = \frac{\alpha G_F^2 m_b^2}{128\pi^4}\left|\sum_{i=c,t}\lambda_i C_{7i}(m_b)\right|^2$$

$$C_{7i}(m_b) = \eta^{-16/23}[C_{7i}(M_W) - \frac{116}{135}(\eta^{10/23} - 1) - \frac{116}{378}(\eta^{28/23} - 1)]$$

$$(3.84) \quad C_{7i}(M_W) = A_W(m_i^2/M_W^2) + \tan^2\omega\ A_{Hi}(m_i^2/m_{H+}^2).$$

Here $\lambda_i = V_{is}^* V_{ib}$, $\eta = \alpha_s(m_b)/\alpha_s(M_W)$, A_W is the SM contribution due to $W^{+/-}$ loops and A_H is the additional contribution due to triangle diagrams involving the charged Higgs. For expressions of A_W and A_H see for instance [71]. The SM value for the width can be obtained by simply putting $\omega = 0$ or taking the limit $m_{H+} \to \infty$ in the above equation.

Let the fractional deviation of the type I 2HDM value from the SM value be,

$$(3.85) \qquad\qquad r = \frac{\Gamma_{b\to s\gamma}^{2HDM-I} - \Gamma_{b\to s\gamma}^{SM}}{\Gamma_{b\to s\gamma}^{SM}}.$$

Fig. 3.5 shows the contours of constant r in the m_{H+}-$\tan\omega$ plane. The dashed lines in Fig. 3.5 show the region excluded by experiments at 2σ level. To obtain the dashed curves we have used the world average for the experimental value of the branching fraction [72],

$$B(\bar{B} \to X_s\gamma) = (3.55 \pm 0.24^{+0.09}_{-0.10} \pm 0.03) \times 10^{-4}.$$

We have rescaled the theoretical value obtained using Eq. (3.84) to reproduce the NNLO SM prediction [73],

$$B(\bar{B} \to X_s\gamma) = (3.15 \pm 0.23) \times 10^{-4}$$

in the $m_{H^+} \to \infty$ limit and added the error associated with this value in quadrature to the experimental error. From Eq. (3.84) one can see that there are two different ways of satisfying the constraint: (1) if $\tan\omega$ is small the type I 2HDM width is close to the SM value, or (2) $\tan^2\omega$ can be tuned to a higher value so that $\left|\sum_{i=c,t} \lambda_i C_{7i}(m_b)\right|$ in Eq. (3.84) is close to its SM value ($C_{7i} \simeq -C_{7i}^{SM}$). Thus there are two disconnected allowed regions in Fig. 3.5. We can see from Fig. 3.5 that the constraint is satisfied for all values of m_{H^+} if,

$$(3.86) \qquad\qquad\qquad \tan\omega < 0.32$$

which translates to,

$$(3.87) \qquad\qquad\qquad v_2 < 75 \text{ GeV}.$$

For $m_{H^+} = 200$ GeV we obtain the constraint $\tan\omega < 0.47$ ($v_2 < 105$ GeV). Another constraint due to virtual $H^{+/-}$ effects comes from $B_d^0 - \bar{B}_d^0$ oscillations. This, however, puts a weaker constraint than the $b \to s\gamma$ process at the 2σ level [74].

It is important to note that a small v_2 not only implies a small ω but also suggests a small α for a 2HDM with the general potential in Eq. (3.41). This can be seen from the expression for $\tan 2\alpha$ in Eq. (3.82). Using Eq. (3.79) we can obtain the expression for $\tan 2\alpha$ for $\tan\omega = v_2/v_1 \ll 1$,

$$(3.88) \qquad\qquad \tan 2\alpha \approx \frac{\lambda_3 + \lambda_4 - (m_A^2/v_1^2)}{\lambda_1 - \frac{1}{2}(m_A^2/v_1^2 + \lambda_5)} \tan\omega$$

which shows that a small v_2 suggests that α should be small too.

The ρ parameter

In the 2HDM the ρ-parameter gets additional contributions from corrections to M_W and M_Z due to loops of the scalars. With respect to the SM theory with a Higgs boson mass of $m_h = 120$ GeV, the range of $\Delta\rho$ that can be tolerated [55] by
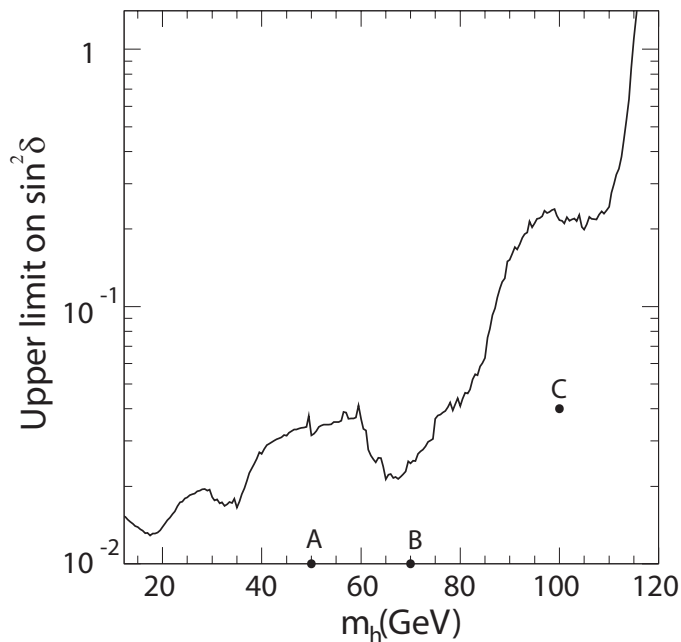
Figure 3.6: Upper bounds on $\sin^2 \delta$ as a function of m_h derived from searches for the Higgsstrahlung process $e^+ e^- \to Zh$ at LEP with center of mass energy $\sqrt{s}$ = 91-209 GeV. It has been assumed that h decays entirely to $b\bar{b}$. We also plot the three parameter sets A, B and C that we have chosen for simulations (Table 3.3) on the $\sin^2 \delta$ - m_h plane. The curve has been reproduced from Ref. [2].

replacing the single SM Higgs boson with the 2HDM is $0.0000 \lesssim \Delta\rho \lesssim 0.0012$ at the 68% CL, where $\Delta\rho = \rho(2HDM) - \rho(m_h^{SM})$. The 2HDM computation needed for this can be found in Ref. [75]. One finds that it is easy to satisfy precision electroweak constraints for a 2HDM with masses in the neighborhood of $50 - 300$ GeV, as we shall see later in our example benchmark points that we use to study collider signatures.

3.4.3 Collider Constraints

The fact that none of the scalars h, H or A were seen at LEP puts constraints on their masses m_h, m_H, m_A and $\delta = |\alpha - \omega|$. We are especially interested in the cases when the decay modes $A \to Zh$ or $H \to hh/AA$ are kinematically allowed, i.e. when the conditions $|m_A - m_h| > m_Z$ or $m_H > 2m_{h/A}$ hold respectively.

The major constraint on the mass of the non SM-like CP-even Higgs, m_h comes from the non-discovery of h produced by the Higgstrahlung process $e^+e^- \to hZ$ at LEP. The cross section of the Higgstrahlung process in the 2HDM is suppressed by a factor of $\sin^2 \delta$ with respect to the cross section of the same process in the SM. It is therefore possible to have h as light as we wish by choosing a sufficiently small value of δ. Upper bounds on the cross section for this process for a particular value of m_h therefore give upper bounds on $\sin^2 \delta$. Fig. 3.6 shows the LEP2 upper bounds [2] on $\sin^2 \delta$ vs m_h assuming h decays entirely to $b\bar{b}$. As one can see from the figure there are no constraints on m_h at all, if $\sin \delta < 0.1$, and no constraints on $\sin \delta$ if $m_h > 114$ GeV. If we take $\sin \delta < 0.2$, $m_h \approx 100$ GeV is safely within allowed limits.

Another important process that could have been potentially seen at LEP is the associated production process $e^+e^- \to hA$. The cross section for this process is proportional to $\cos^2 \delta$ in the 2HDM. Analysis of LEP2 data, assuming $|m_A - m_h| > m_Z$ so that A predominantly decays as $A \to Zh$, has been done by the DELPHI collaboration [76] and the process has been found to be unconstrained. Even if this condition does not hold there are no constraints on δ if we have $m_A + m_h > 200$ GeV [2].

The constraints on the pseudoscalar mass m_A are much weaker. The cross section of associated production process, $e^+e^- \to HA$, is proportional to $\sin^2 \delta$. The results of LEP analyses motivated by this process put upper limits on $\sin^2 \delta$ for a given m_A and m_H (see Ref. [2] for details). If the dominant decay mode is $H \to AA$ there are no constraints at all if $m_H > 120$ GeV and $m_A > 50$ GeV [2].

As far as the charged Higgs is concerned, the LEP2 direct search constraints from the process $e^+e^- \to Z^* \to H^+H^-$ place a lower limit of 76.7 GeV on m_H^+ [77]. The Tevatron search for $t \to H^+b$ puts a 95% CL upper bound on $B(t \to H^+b)$ at $0.1-0.3$

in the mass range 90 GeV$< m_{H^+} < 150$ GeV assuming B$(H^+ \rightarrow c\bar{s})$ to be 100% [78].
For almost the entire mass range $B(t \rightarrow H^+ b) < 0.1$ is allowed. In the type I 2HDM
this branching ratio is proportional to $\tan^2 \omega$, so that we obtain $\tan \omega \ (\approx s_\omega) < 0.3$
for $m_{H^+} = 90$ GeV and $\tan \omega < 0.8 \ (s_\omega < 0.6)$ for $m_{H^+} = 150$ GeV by requiring
$B(t \rightarrow H^+ b) < 0.1$. The limit on $\tan \omega$ is actually too conservative for $m_{H^+} = 90$
GeV as the upper bound on the branching fraction for this mass is about 0.3.

Finally let us consider the SM-like Higgs boson H. If $m_H < 2m_{h/A}$, H would
predominantly decay into quarks with branching ratios very similar to that in SM.
In this case the process $e^+ e^- \rightarrow HZ$ puts a weaker lower bound on m_H in 2HDMs
than the SM value 114 GeV because the 2HDM cross section of this process is smaller
than the SM cross section by a factor $\cos^2 \delta$. If $H \rightarrow hh/AA$ is allowed there are
of course no constraints on δ if $m_H > 115$ GeV, and for $\delta > 0$, m_H can be even
smaller [2]. We will take $m_H = 120$ GeV for all the parameter sets we use in our
simulations in section 3.6.

3.5 Yukawa Coupling Perturbativity

If there exists at least one Higgs boson with a VEV that does not couple to a
fermion f, the Yukawa coupling of that fermion λ_f must necessarily be greater than
its corresponding would-be SM value. Larger Yukawa couplings in the theory run
the risk of renormalizing to strong coupling at a lower scale than desired. In our
study this is a consideration that must be explored, since our emphasis is on next
generation Higgs bosons that do not couple to the fermions. Therefore, in this section
we quantify where Yukawa couplings blow up in renormalization group evolution as
a function of the VEV of fermiophobic Higgs doublets in the theory. The effect is
particularly pronounced for the top quark Yukawa coupling, since it is associated

with the highest mass fermion in the theory.

The one loop Renormalization Group Equations (RGEs) for the Yukawa (λ_f) [79] and gauge couplings (see for eg. [80]) in an extension of the SM with n_d extra Higgs doublets is,

$$(3.89) \quad \frac{d\lambda_t}{d(\ln\mu)} = \frac{\lambda_t}{16\pi^2}\left(\frac{3}{2}\lambda_t^2 - \frac{3}{2}\sum_D |V_{tD}|^2\lambda_D^2 + S - 8g_3^2 - \frac{9}{4}g_2^2 - \frac{17}{12}g'^2\right)$$

$$(3.90) \quad \frac{d\lambda_b}{d(\ln\mu)} = \frac{\lambda_b}{16\pi^2}\left(\frac{3}{2}\lambda_b^2 - \frac{3}{2}\sum_U |V_{Ub}|^2\lambda_U^2 + S - 8g_3^2 - \frac{9}{4}g_2^2 - \frac{5}{12}g'^2\right)$$

$$(3.91) \quad \frac{d\lambda_\tau}{d(\ln\mu)} = \frac{\lambda_\tau}{16\pi^2}\left(\frac{3}{2}\lambda_\tau^2 + S - \frac{9}{4}g_2^2 - \frac{15}{4}g'^2\right)$$

$$(3.92) \quad \frac{dg'}{d(\ln\mu)} = \frac{\frac{41+n_d}{6}g'^3}{16\pi^2}, \quad \frac{dg_2}{d(\ln\mu)} = \frac{\frac{-19+n_d}{6}g_2^3}{16\pi^2}, \quad \frac{dg_3}{d(\ln\mu)} = -\frac{7g_3^3}{16\pi^2},$$

where $S = 3\sum_U \lambda_U^2 + 3\sum_D \lambda_D^2 + \sum_E \lambda_E^2$. U, D and E denote the up-type quarks, the down-type quarks and the leptons while g', g_2 and g_3 are the $U(1)_Y$, $SU(2)_L$ and $SU(3)$ gauge couplings. Note that the summation over U, D does not include a summation over colors. There are similar equations for the other up-type quarks ($t \to U$ in Eq. (3.89)), the other down-type quarks ($b \to D$ in Eq. (3.90) and the other leptons ($\tau \to E$ in Eq. (3.91)). For the type I 2HDM $n_d = 1$.

For supersymmetric models with n_g extra generations of Higgs doublet pairs than
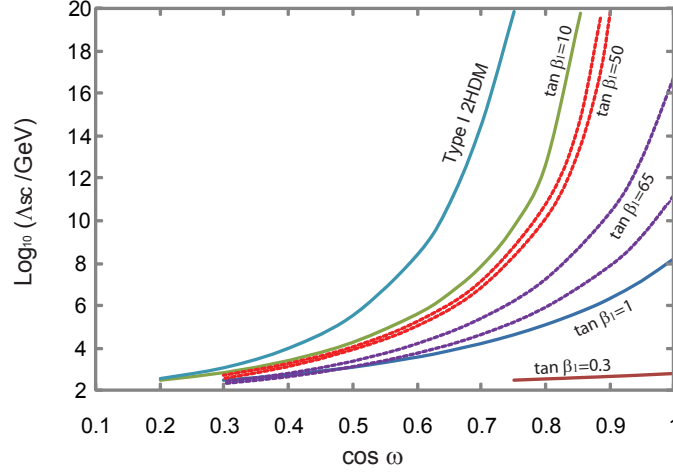
Figure 3.7: Λ_{SC}, the energy scale at which either one of the three large Yukawa couplings λ_t, λ_b or λ_τ becomes larger than 4π, as a function of c_ω. We show curves for the type I 2HDM case as well as the the SUSY 2HGM with different values of $\tan\beta_1$. For the $\tan\beta_1 = 50$ and $\tan\beta_1 = 65$ cases we show two dashed curves corresponding to the minimum (left) and maximum (right) allowed value of $m_b(M_Z)$ in Eq. (3.102). For the mean value $m_b(M_Z) = 2.85$ GeV in Eq. (3.102), for $\tan\beta_1 \geq 55$ it is the bottom Yukawa which becomes strong ($> 4\pi$). We have used the Renormalization Group Equations at one loop level.

MSSM the one loop RGEs for Yukawa [79] and gauge couplings (see for eg. [81]) are,

$$\frac{d\lambda_t}{d(\ln\mu)} = \frac{\lambda_t}{16\pi^2}\left(3\lambda_t^2 + \sum_D |V_{tD}|^2\lambda_D^2 + 3\sum_U \lambda_U^2 - \frac{16}{3}g_3^2 - 3g_2^2 - \frac{13}{9}g'^2\right)$$

(3.93)

$$\frac{d\lambda_b}{d(\ln\mu)} = \frac{\lambda_b}{16\pi^2}\left(3\lambda_b^2 + \sum_U |V_{Ub}|^2\lambda_U^2 + 3\sum_D \lambda_D^2 + \sum_E \lambda_E^2 - \frac{16}{3}g_3^2 - 3g_2^2 - \frac{7}{9}g'^2\right)$$

(3.94)

$$\frac{d\lambda_\tau}{d(\ln\mu)} = \frac{\lambda_\tau}{16\pi^2}\left(3\lambda_\tau^2 + 3\sum_D \lambda_D^2 + \sum_E \lambda_E^2 - 3g_2^2 - 3g'^2\right)$$

(3.95)

$$\frac{dg'}{d(\ln\mu)} = \frac{(11+n_g)g'^3}{16\pi^2}, \quad \frac{dg_2}{d(\ln\mu)} = \frac{(1+n_g)g_2^3}{16\pi^2}, \quad \frac{dg_3}{d(\ln\mu)} = -\frac{3g_3^3}{16\pi^2}.$$

(3.96)

For the supersymmetric two Higgs generation Model (SUSY 2HGM) of Section 3.3.1

$n_g = 1$. There are similar equations for the other up-type quarks ($t \to U$ in Eq.

(3.93)), the other down-type quarks ($b \to D$ in Eq. (3.94)) and the other leptons

$(\tau \to E$ in Eq. (3.95)).

The Yukawa couplings in type I 2HDM are given by,

$$(3.97) \qquad \lambda_f(m_f) = \sqrt{2}\frac{m_f(m_f)}{vc_\omega}$$

where $c_\omega = v_1/v$ (with $v = 2M_W/g$). In the SUSY 2HGM the Yukawa couplings are given by,

$$(3.98) \qquad \lambda_U(m_U) = \sqrt{2}\frac{m_U(m_U)}{vc_\omega s_{\beta_1}}$$

$$(3.99) \qquad \lambda_D(m_D) = \sqrt{2}\frac{m_D(m_D)}{vc_\omega c_{\beta_1}}$$

$$(3.100) \qquad \lambda_E(m_E) = \sqrt{2}\frac{m_E(m_E)}{vc_\omega c_{\beta_1}}$$

where $\tan\beta_1 = v_{u1}/v_{d1}$.

In the type I 2HDM all the Yukawa couplings except for the top Yukawa coupling can be ignored. In the SUSY 2HGM in addition to the top Yukawa, the tau and bottom Yukawa couplings also become important at high values of β_1. We have solved the RGE with the boundary conditions,

$$(3.101) \qquad m_t(pole) = m_t(m_t)\left(1 + \frac{4\alpha_s(m_t)}{3\pi}\right) = 171.3 \text{ GeV}$$

$$(3.102) \qquad m_b(M_Z) = 2.7 - 3.0 \text{ GeV}$$

$$(3.103) \qquad m_\tau(M_Z) = 1.75 \text{ GeV}$$

[82] and $\alpha_s(M_Z) = 0.1182$. In Eq. (3.102) the allowed range corresponds to the Particle Data Group (PDG) range for $m_b(m_b) = 4.03 - 4.37$ GeV [55]. Let Λ_{SC} be the strong coupling scale, i.e the energy scale at which either one of the three large Yukawa couplings λ_t, λ_b or λ_τ becomes larger than 4π. In Fig. 3.7 we show how Λ_{SC} varies as a function of c_ω. We show the curve for the type I 2HDM case as well as the curves for the SUSY 2HGM for various values of $\tan\beta_1$. In the SUSY 2HGM at

Set	Input Parameters	$\Delta\rho$
A	$m_H = 120$ GeV, $m_h = 50$ GeV, $m_A = 150$ GeV, $m_{H^+} = 200$ GeV, $s_\omega = 0.1$, $s_\alpha = 0.2$ ($\sin\delta = 0.10$)	0.0010
B	$m_H = 120$ GeV, $m_h = 70$ GeV, $m_A = 180$ GeV, $m_{H^+} = 200$ GeV, $s_\omega = 0.1$, $s_\alpha = 0.2$ ($\sin\delta = 0.10$)	0.0003
C	$m_H = 120$ GeV, $m_h = 100$ GeV, $m_A = 200$ GeV, $m_{H^+} = 200$ GeV, $s_\omega = 0.1$, $s_\alpha = 0.3$ ($\sin\delta = 0.20$)	< 0.0001

Table 3.3: Example parameter sets. The values of $\Delta\rho$ are computed in these 2HDMs with respect to the SM value with Higgs mass of 120 GeV.

high values of $\tan\beta_1 \gtrsim 50$ the bottom Yukawa coupling becomes strong at a lower energy scale than the top Yukawa coupling.

We see from the results of this section that if we allow the fermiophobic next generation Higgs doublet too large of a VEV, the enhanced Yukawa couplings that are required to make up for the smaller VEV of the Higgs boson that the fermions couple to may diverge at a lower scale than desired. For example, if one wishes to preserved supersymmetric gauge coupling unification up to the scale of $\sim 10^{16}$ GeV there are critical values of $\cos\omega$ that cannot be crossed depending on $\tan\beta_1$, which leads to maximum values of the next generation Higgs boson VEV.

3.6 Signatures at the Large Hadron Collider

In this section we identify processes that can provide signatures of next generation Higgs bosons at the LHC. While our numerical results have been obtained for the type I 2HDM our basic conclusions are true for next generation Higgs bosons in general.

3.6.1 Dominant decay modes

We will now compute the branching ratios of the various decay modes of the neutral Higgs bosons in the type I 2HDM. The relevant Feynman rules can be found in Ref. [66].

Fig. 3.8(a) shows the branching ratios for decay of the pseudoscalar A (see Eq. (3.42)). The decay modes $A \to hh$, $A \to HH$, $A \to WW$ and $A \to ZZ$ are not allowed by symmetry as A is a pseudoscalar. As shown in the figure, when allowed kinematically, the branching ratio for $A \to Zh$ is nearly unity.

The SM-like Higgs H decays mainly via the modes $H \to hh/AA$ even if modes like $H \to WW$ and $H \to ZZ$ are kinematically allowed. Fig. 3.8(b) shows the branching ratios of H in potential A with a light h.

The branching ratios of h are very similar to that of a SM Higgs for small values of m_h when decay modes like $h \to ZA$ and $h \to AA$ are not kinematically allowed. For $m_h > 2m_A$, the decay mode $h \to AA$ overwhelms all other modes including $h \to ZA$, $h \to WW$ and $h \to ZZ$. A very interesting limit is $\alpha \to 0$, $\omega \to 0$. In this limit h becomes both fermiophobic and bosophobic (the tree level coupling of h to fermions is proportional to $-s_\alpha/c_\omega$ and the coupling to vector bosons is proportional to $\sin \delta$) and the dominant decay mode becomes $h \to \gamma\gamma$. This case has been dealt with in detail in Ref. [66] and [83].

3.6.2 The $pp \to Zh(b\bar{b})h(b\bar{b})$ signal and choice of input parameters

As we noted in Section 3.4.2 indirect constraints put an upper bound on v_2 in the type I 2HDM and this not only implies a small ω but also suggests a small α and hence suggests a small $\delta = |\alpha - \omega|$. A small VEV for the fermiophobic Higgs doublets is also required for high scale perturbativity as we saw in the last section. If δ is small a light h can satisfy the constraints due to the $e^+e^- \to hZ$ at LEP (Fig. 3.6). The pseudoscalar A must then be chosen sufficiently heavy to satisfy the LEP constraints from $e^+e^- \to hA$ (see Section 3.4.3).

Another implication of a small δ is that unlike the process $pp \to hZ$, which is highly suppressed (by $\sin^2 \delta$ in 2HDMs), the processes $pp \to Ah$ and $pp \to ZH$ are
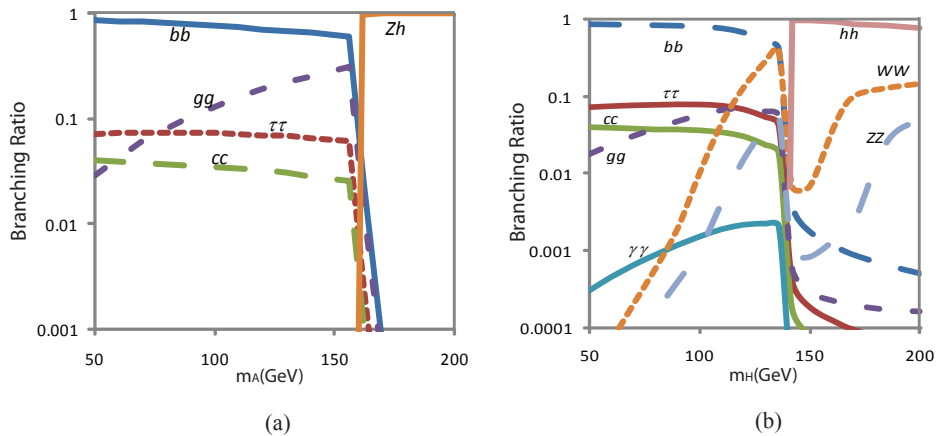
Figure 3.8: (a) Branching ratios of the various decay modes of the pseudoscalar A with $m_H = 120$ GeV, $m_h = 70$ GeV, $m_{H^+} = 150$ GeV, $s_\alpha = 0.2$ and $s_\omega = 0.1$ in any 2HDM and (b) branching ratios of the SM-like Higgs H in potential A with $m_A = 180$ GeV, $m_h = 70$ GeV, $m_{H^+} = 150$ GeV, $s_\alpha = 0.2$ and $s_\omega = 0.1$.

only mildly suppressed (by $\cos^2 \delta$ in 2HDMs). In the first case, if allowed kinematically, A predominantly decays as $A \to Zh$ (Fig. 3.8(a)) and in the second case H predominantly decays as $H \to hh/AA$ (Fig. 3.8(b)) if allowed to kinematically so that both processes can lead to the same final state $Zh(b\bar{b})h(b\bar{b})$.[3]

Table 3.3 shows three different sets of input parameters for which we perform simulations to compute the $pp \to Zh(b\bar{b})h(b\bar{b})$ signal. Set A receives contributions from both the $pp \to Ah$ and $pp \to ZH$ processes whereas all the other sets receive contributions from the $pp \to Ah$ process only. We have also computed $\Delta\rho$ for all the data sets in Table 3.3 to show that this constraint is met. As for the other constraints, we have marked these parameter sets in Fig. 3.5 and Fig. 3.6 to show that our parameter sets satisfy the $b \to s\gamma$ constraint and the $e^+e^- \to hZ$ constraint respectively.

As mentioned in Section 3.4.3 a light A is experimentally less constrained than a light h. Although we will not perform simulations for the process $pp \to A(b\bar{b})h$

---

[3]Note, however, that in a 2HDM with potential B, in the limit $\alpha, \omega \to 0$ we get $m_h^2 \to m_A^2$ (see Eq. (3.72) and Eq. (3.76)) so that $A \to Zh$ would not be kinematically allowed in this limit. This issue does not arise for potential A or the general potential in Eq. (3.41).
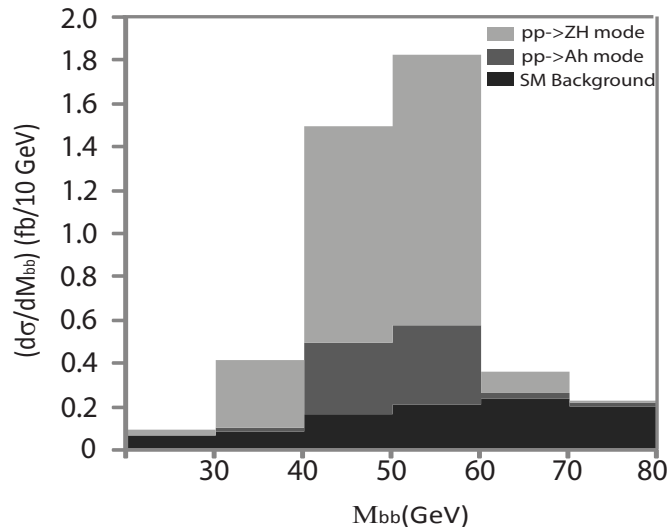
Figure 3.9: The $2b$ invariant mass spectrum M_{bb} for the signal on top of the SM background for the input parameters in Set A (see Table 3.3), showing a peak at $m_h = 50$ GeV. Two processes contribute to the signal (1) $pp \to A(Zh)h \to Z(l^+l^-)Zb\bar{b}b\bar{b}$ and (2) $pp \to ZH(hh) \to Z(l^+l^-)Zb\bar{b}b\bar{b}$. The cuts applied are those in eqs. (3.104)-(3.107) and the center of mass energy has been taken to be 14 TeV. The branching ratio $B(H \to hh) \approx 1$. The reconstruction efficiency of the lepton pair and the jets and the b-tagging efficiency have all been taken to be unity at this stage.

followed by $h \to ZA(b\bar{b})$ the analysis of the process would be very similar to the process we will consider. This process would be important if $h \to ZA$ is kinematically allowed but $h \to AA$ is not kinematically allowed. If $m_H > 2m_A$ the process $pp \to ZH(AA) \to Zb\bar{b}b\bar{b}$ will be a very important signature. Although we will not perform a simulation for such a scenario, we will compute the contribution to the cross section of the process $pp \to ZH(hh) \to Zb\bar{b}b\bar{b}$ for Set A (this will be a part of the net cross section). This is again expected be very similar to the case when A, rather than h, is the lighter scalar that H decays into.

It should be clear that all the arguments that have led us to the $pp \to A(Zh)h \to Zh(b\bar{b})h(b\bar{b})$ signal are valid not only for the type I 2HDM but for any multi-Higgs theory having scalar doublets that do not couple to fermions. It is easiest to satisfy the constraints from charged Higgs loop contributions (as in the $b \to s\gamma$ process) and high scale perturbativity if the VEVs of these fermiophobic doublets are small. Let
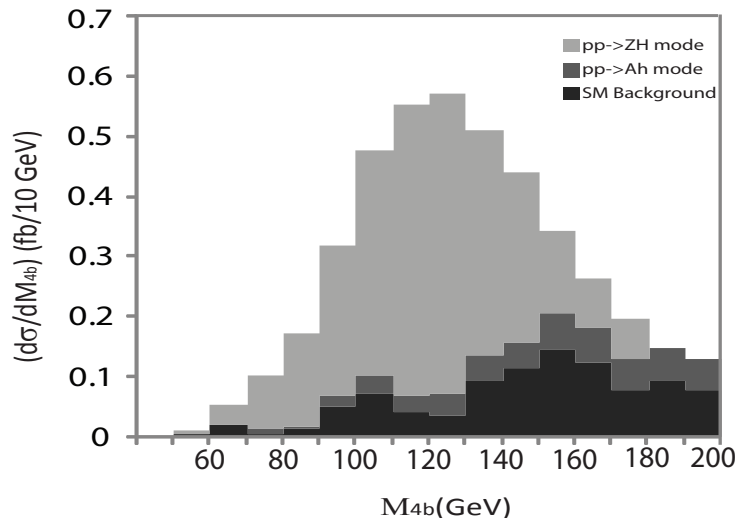
Figure 3.10: The $4b$ invariant mass spectrum M_{4b} for the signal on top of the SM background for the input parameters in Set A (see Table 3.3). Two processes contribute to the signal (1) $pp \to A(Zh)h \to Z(l^+l^-)Zb\bar{b}b\bar{b}$ and (2) $pp \to ZH(hh) \to Z(l^+l^-)Zb\bar{b}b\bar{b}$. The $pp \to ZH(hh)$ mode gives rise to a peak at $m_H = 120$ GeV. We have smeared the $4b$ invariant mass assuming an experimental resolution of 20% of m_H (24 GeV in this case) for the reconstructed peak. The cuts applied are those in eqs. (3.104)-(3.107) and the center of mass energy has been taken to be 14 TeV. The branching ratio $B(H \to hh) \approx 1$. The reconstruction efficiency of the lepton pair and the jets and the b-tagging efficiency have all been taken to be unity at this stage.

h and A be mass eigenstates that contain mostly the CP-even and CP-odd neutral components of such a doublet respectively. A small VEV of this doublet would imply that the ZZh coupling strength is small, but the ZAh coupling strength would not get suppressed.

3.6.3 Signal and Background cross section at LHC

We now present the results of the simulations we performed for the $pp \to Zh(b\bar{b})h(b\bar{b})$ signal. The analyses we present are new; however, there are related studies that we will point out to the reader in our Set A analysis. All our results are independent of the choice of 2HDM potential except for the $H \to hh$ contribution to the signal in parameter set A that depends on $B(H \to hh)$ which is model dependent. $B(H \to hh)$ has been taken to be equal to its value in potential A which is nearly 1. We used
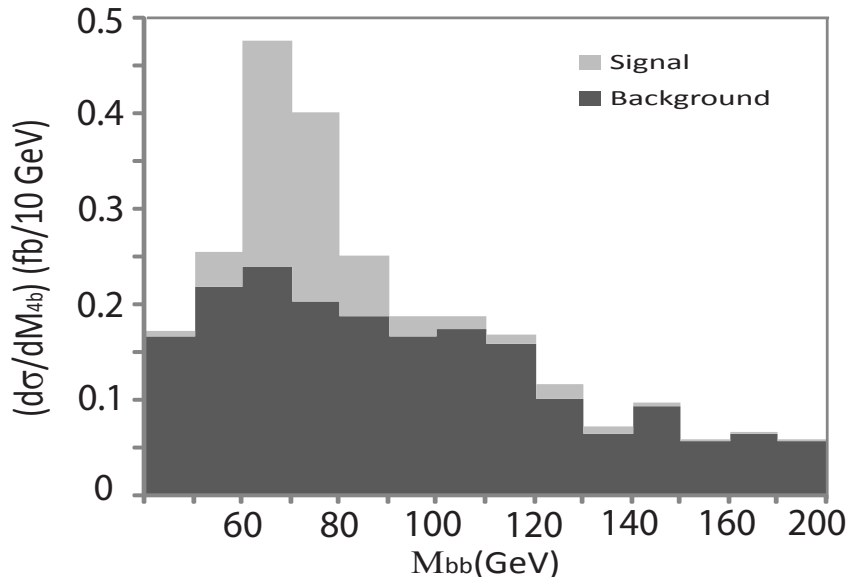
Figure 3.11: Invariant mass spectrum M_{bb} for the signal on top of the SM background for the input parameters in Set B (see Table 3.3), showing a peak at $m_h = 70$ GeV. The signal process is $pp \to A(Zh)h \to Z(l^+l^-)Zb\bar{b}b\bar{b}$. The cuts applied are those in eqs. (3.104)-(3.107) and the center of mass energy has been taken to be 14 TeV. The reconstruction efficiency of the lepton pair and the jets and the b-tagging efficiency have all been taken to be unity at this stage.

MADGRAPH [84] to generate signal and background events at 14 TeV center of mass energy for the process $pp \to Zh(b\bar{b})h(b\bar{b})$ for the different parameter sets in Table 3.3. We then decayed the Z to l^+l^- ($l = e, \mu$) using the DECAY software in the MADGRAPH package. Note that we have ignored any contribution to the SM background from final states with lepton pairs not produced in Z decay that have invariant mass close to M_Z nevertheless. The following basic selection cuts have been applied using MadAnalysis,

$$p_T(b,l) > 15 \text{ GeV} \tag{3.104}$$

$$|\eta_{b,l}| < 2.5 \tag{3.105}$$

$$\Delta R_{bp} > 0.4. \tag{3.106}$$

where $\Delta R = \sqrt{(\Delta \eta)^2 + (\Delta \phi)^2}$ and p is any parton (i.e. quark or lepton) in the process. The background cross section with these cuts is 9.9 fb. To reduce the
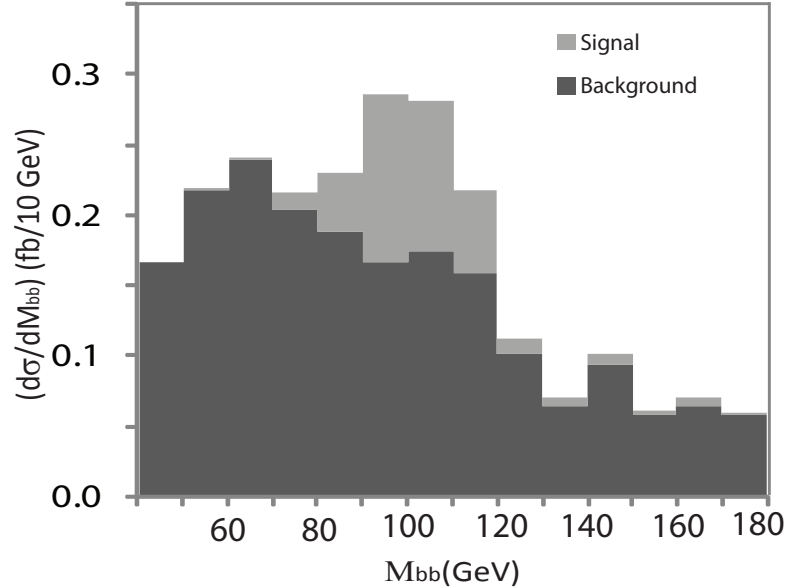
Figure 3.12: Invariant mass spectrum M_{bb} for the signal on top of the SM background for the input parameters in Set C (see Table 3.3), showing a peak at $m_h = 100$ GeV. The signal process is $pp \to A(Zh)h \to Z(l^+l^-)Zb\bar{b}b\bar{b}$. The cuts applied are those in eqs. (3.104)-(3.107) and the center of mass energy has been taken to be 14 TeV. The reconstruction efficiency of the lepton pair and the jets and the b-tagging efficiency have all been taken to be unity at this stage.

background further we use the fact that two $b\bar{b}$ pairs have the same invariant mass in the signal up to experimental resolution. Detector simulations of scalars decaying into b-pairs [85] find that because of detector effects like calorimeter energy resolution, electronic noise, and physics effects like final state radiation, energy loss outside cone and semi leptonic decays, only about 85% of the events register di-b-jet invariant masses within 20% of the true value. To simulate this effect we smear the invariant masses according to a Gaussian distribution such that 85% of the events lie within 20% of the mean. There are three ways to divide the four b-quarks (say $abcd$) into two pairs (ab cd, ac bd and ad bc). The combination that gives the invariant masses of the two pairs (after smearing) closest to each other has been considered (note that in reality the experimental uncertainties in the invariant masses of the six possible

Set	Cross Section with the cuts in eqs. (3.104)-(3.106) (fb)	Cross Section with the cuts in eqs. (3.104)-(3.107) (fb)	Detector level Cross-Section with the cuts in Eqs.(3.104)-(3.107)
Set A			
$pp \rightarrow Ah$	1.2	0.8	0.1
$pp \rightarrow ZH$	3.6	2.7	0.4
Total	4.8	3.5	0.5
Set B			
$pp \rightarrow Ah$	0.9	0.6	0.09
Set C			
$pp \rightarrow Ah$	0.6	0.4	0.06
SM Background	9.9	2.6	0.4

Table 3.4: Signal and background cross sections for $pp \rightarrow Zh(b\bar{b})h(b\bar{b})$ at LHC. The center of mass energy has been taken to be 14 TeV and the acceptance cuts are those mentioned in the top row.

b-pairs are not uncorrelated as assumed here). Let M_{bb1} and M_{bb2} be the smeared invariant masses of the two b pairs thus selected, and let M_{bb} be the mean of these two numbers. We impose the following cut in addition to those in Eq. (3.104),

$$(3.107) \qquad\qquad |M_{bb1} - M_{bb2}| < 0.2\ M_{bb}.$$

With this additional cut the background is reduced from 9.9 fb to 2.6 fb whereas the signal is only reduced to about 70% of the value with only the cuts in eqs. (3.104)-(3.106). We provide the cross sections for the different parameter sets and the background in Table 3.4. Note that the background cross section can be further reduced by requiring M_{bb} to be in a certain mass window around m_H

In Fig. 3.9 we plot the $2b$ invariant mass spectrum for Set A obtained for the events passing the cuts in eqs. (3.104)-(3.107). For Set A the contribution to the cross section of $pp \rightarrow Zh(b\bar{b})h(b\bar{b})$ comes from two different processes $pp \rightarrow A(Zh)h \rightarrow Zb\bar{b}b\bar{b}$ and $pp \rightarrow ZH(hh) \rightarrow Zb\bar{b}b\bar{b}$. The branching ratio $B(H \rightarrow hh)$ has been taken to be equal to its potential A value which is nearly 1. As shown in Fig. 3.9 the

contribution from $pp \to ZH(hh)$ mode is quite large. This contribution also gives rise to a peak in the $4b$ invariant mass spectrum as shown in Fig. 3.10. We have smeared the $4b$ invariant mass assuming an experimental resolution of 20% of m_H (24 GeV in this case) for the reconstructed peak. We expect very similar results if A rather than h is the scalar H decays to. The signal from $pp \to ZH(AA) \to Zb\bar{b}b\bar{b}$ will be a very promising signature for the type I 2HDM, especially because the constraints on a light A are rather weak as discussed in section 3.4.3. Similar analyses for $H \to AA$ have been done before (in Ref. [86] the final state $lA(b\bar{b})A(b\bar{b})$ has been considered while in Ref. [87] the final state $W(E_T^{miss}l)A(b\bar{b})A(b\bar{b})$ has been considered). These papers, however, do not apply the cut in Eq. (3.107) which leads to improved significance of the signal.

Fig. 3.11, 3.12 shows the $2b$ invariant mass spectrum for the other parameter sets. Only the process $pp \to A(Zh)h \to Zb\bar{b}b\bar{b}$ contributes to the cross section in these cases.

To get the cross section we expect the detectors to effectively measure we must multiply by the efficiency of reconstruction of a lepton pair and that of four jets. These efficiencies depend on kinematical quantities like p_T and η. We take an average value 0.8 for lepton pair reconstruction efficiency (see pgs. 72-92, pgs. 210-223 in Ref. [49]) and 0.9 for reconstruction efficiency of a jet (see pgs. 286-287 in Ref. [49]). We also require that at least three of the jets are b-tagged which gives an overall b-tagging efficiency equal to $\binom{4}{3}\epsilon_b^3(1-\epsilon_b)+\epsilon_b^4$ where the b-tagging efficiency for single jet $\epsilon_b \approx 0.5$ [49]. Putting it all together we get,

$$(3.108) \qquad\qquad \sigma^{eff} = 0.16\ \sigma.$$

This equation is applicable for both the cross section and the background. The effective signal and background cross sections also appear in Table 3.4.

We have not computed the contribution due to mistagging of c-jets or other light jets. This will decrease the signal significance somewhat as mistagging is expected to have an appreciable contribution only to the SM background and not the signal. This is because the signal cross section is proportional to the square of the branching ratio of h to the mistagged quarks but the branching ratio of h to quarks other than b-quarks is much smaller. In Ref. [87] the signal and background cross sections for the process $pp \to WH \to W(E_T^{miss}l)A(b\bar{b})A(b\bar{b})$ have been computed including mistagging effects. A rough estimate of the cross sections they obtain can be made from Fig. 5 in their paper. Such an estimate shows that the background cross section they obtain due to mistagged quarks is about a third of the contribution due to correctly tagged b quarks. This mistag background is highly dependent upon the details of detector performance issues that will be sorted out in the course of the LHC runs. We do not expect the addition of these backgrounds to substantively change the discovery capability that we have presented, especially since they are unlikely to peak at the Higgs mass m_h in the di-jet invariant mass spectrum.

3.7   Conclusion and Discussion

In conclusion, we have argued that next generation Higgs bosons should be viewed as generic possibilities in string theory model building, and illustrated this viewpoint with recent developments in string phenomenology. We presented a generalized theorem for the structure of Higgs couplings to SM fermions that automatically avoids problematic tree-level flavor changing neutral currents that are induced by new Higgs boson exchanges. Our viewpoint is that the interaction rules of this theorem are too restrictive to be satisfied without a principle. In the case of the two-Higgs doublet model of supersymmetry, the principle is holomorphy. Additional Higgs bosons

added in any other context, such as more Higgs doublet pairs in supersymmetry or simply another Higgs boson in the SM, requires a strong discrete symmetry or selection rule. This can be contemplated within effective field theories, for example by $\Phi \to -\Phi$ Z_2 symmetry, or within string theory by algebraic selection rules that may not totally forbid the unwanted couplings but can approximate zero, as was the case in the work of [51].

Next we considered various constraints that these theories must face. For example, although tree-level flavor changing neutral currents induced by neutral Higgs exchanges may be satisfied, loop-level ones induced by the charged Higgs boson may not be. The $b \to s\gamma$ transition is quite constraining to exotic Higgses that get large vacuum expectation values, since they steal VEV from the Higgs that couples to fermions, thereby raising those fermion Yukawa coupling magnitudes to dangerous levels. Even normal Cabibbo-Kobayashi-Maskawa (CKM) mixings can create too-large amplitude shift in that case compared to what experiment allows, and therefore the parameter space is not completely open and limits are derived on the exotic Higgs VEV as a function of the charged Higgs boson mass.

We computed the spectrum of Higgs boson states with a next generation in the supersymmetric and non-supersymmetric context. Within supersymmetry we showed that there is the prospect of slightly raising the tree-level CP even Higgs boson mass with respect to the MSSM in the smaller $\tan\beta$ region. The effects are largest when the next generation Higgs boson has a large vacuum expectation value. The large Yukawa couplings that are present when an exotic, fermiophobic Higgs doublet takes a large VEV can alter the domain of perturbativity of the theory. We showed both in the SM context and the supersymmetry context that the top quark Yukawa coupling could develop a Landau pole well below the Planck scale. A low-scale Landau pole

would preclude the existence of a perturbative theory description of unification at the high scale, and these results must be taken into account when considering a next generation of Higgs bosons.

Finally, we investigated the phenomenology of the exotic Higgs sectors at the LHC. Multi-Higgs boson phenomenology within supersymmetry is a mature topic; however, the fermiophobic next generation Higgs boson layer to the theory has not been considered in depth. The salient new features are similar to SM phenomenology with an additional fermiophobic Higgs doublet. Thus, we discussed collider physics possibilities within that less complex framework.

A particularly interesting possibility is the production of hA at the LHC, followed by $A \to hZ$. Assuming h is rather light, say less than $\sim 150\,\mathrm{GeV}$, we can expect the largest branching fraction of h decays to be to $b\bar{b}$. For good distinction from background we can also demand the Z decay to leptons l^+l^-. Thus, the signal becomes $4b + 2l$. Background becomes particularly limited when we require at least three b-quark tags and that the four jets reconstruct two equal mass resonances. We propose that as a search strategy for this case, and show that there are good prospects for the LHC to find this signal. Discovery would be an indication of next generation Higgs bosons.

CHAPTER IV

Higgs boson significance plot deformations due to mixed-in scalars

4.1 Mixed-in singlets

Most of the research related to LHC phenomnology has been directed at different approaches to electroweak symmetry breaking (EWSB) and the hierarchy problem. The possibility of new physics at the TeV scale that is not directly related to EWSB and the hierarchy problem, however, cannot be ruled out. Such new physics will also be accessible to the LHC and one should be prepared for it. The LHC should improve our understanding of what the TeV scale lagrangian of our world is and we should be open to all possibilities not just those that address the questions that we think, with our limited understanding, to be important. We can, for instance, think of new, hidden forces under which the SM is not charged. String theory landscape studies, suggest, for instance that many such hidden sectors might exist. While such new physics may not have any conceptual link with EWSB, as we will see in this chapter, it can still affect Higgs physics at the LHC in very interesting ways.

How would such hidden gauge groups affect us? One possibility is that there are heavy 'messenger' states charged under both SM and hidden sector groups. Such models are called hidden valley models [88]. Another possibility is that relevant gauge invariant hidden sector operators can directly couple to relevant gauge invariant

operators in the SM via renormalizable couplings. The only relevant gauge invariant SM operators are $|\Phi_{SM}|^2$, Φ_{SM} being the SM like Higgs and the hypercharge field strength $B_{\mu\nu}$. Thus we can think of the following couplings,

$$(4.1) \qquad |\Phi_{SM}|^2|\Phi'|^2 \text{ and } B_{\mu\nu}X^{\mu\nu}$$

where Φ is a hidden sector scalar that is a singlet under the SM and $X^{\mu\nu}$ is the field strength of an abelian hidden sector gauge field. The former case is very generic because any scalar field not charged under SM groups is a possible candidate for Φ'. Such an operator would cause a mixing of the mass eigenstates,

$$(4.2) \qquad \begin{pmatrix} H \\ h \end{pmatrix} = \begin{pmatrix} \cos\alpha & \sin\alpha \\ -\sin\alpha & \cos\alpha \end{pmatrix} \begin{pmatrix} \phi \\ \phi' \end{pmatrix}.$$

where ϕ and ϕ' are the neutral CP-even components of the scalars. The couplings of both the Higgs scalars, h and H will be proportional to the SM Higgs couplings and the production cross-section times branching ratio of these Higgs bosons is suppressed as follows,

$$\sigma_H = \xi\sigma_{SM}(m_H)$$
$$(4.3) \qquad \sigma_h = (1-\xi)\sigma_{SM}(m_h),$$

where $\xi = \cos^2\alpha$. A more complete discussion of the theory can be found in [89,90]. While complex scalars charged under new hidden gauge groups are of more interest to us, our analysis holds also for a real scalar, ϕ. In this case the interaction term $|\Phi_{SM}|^2\phi$ will also contribute to the mixing between the scalars. [1]

---

[1] Such sharing of couplings can also arise from the mixing of the SM neutral Higgs component with the neutral components of an exotic doublet, H', or a triplet with no hypercharge, Σ, provided H' or Σ get a vanishing or small VEV. A triplet is, of course, required to have no VEV as it would otherwise give tree-level contributions to the ρ-parameter. As discussed in Ref. [20], vanishing or small VEVs are favored by experimental constraints for exotic doublets too. As the exotic VEV, $v_2 \to 0$, and hence $\beta = \tan^{-1}(v_2/v_1) \to 0$, the mixing angle, α, between the mass eigenstates h and H, which is proportional to β in this limit, also vanishes, i.e. $\alpha = c\beta \to 0$. However, depending on the parameters of the potential, we can still have α/β relatively large (for the case of the doublets, see Eq. (3.88)) so that we can have a non-negligible mixing angle α even if β is much smaller.

In this letter we wish to show how the standard significance searches for the SM Higgs boson are affected by the existence of these mixed-in states. Careful inspection of the $H \to WW \to l\nu l\nu$ "significance plots" could reveal the existence of two more more Higgs bosons, even before the resonance of the second Higgs boson has been found in another search channel with better mass resolution.

We will first describe the method of making significance projections for the SM Higgs boson. For illustration we will proceed along the lines of the ATLAS analysis which has a similar sensitivity to the CMS study but is much easier to reproduce. We will comment on the CMS study at the end. We will then describe how the existence of an extra mixed-in scalar state would alter the significance plots, showing that new physics could be revealed through that shape first. And finally we will make some concluding comments.

4.2   LHC Sensitivity Projections.

We will first reproduce the ATLAS sensitivity projections for Higgs searches at the LHC for 7 TeV center of mass energy that were made in Ref. [1]. We concentrate on the $H \to WW \to l\nu l\nu$ $(l = e, \mu)$ channel as this is the most sensitive channel in the range $125 - 190$ GeV. In the range $130 - 180$ GeV this is by far the dominant channel and sensitivity limits obtained from just this channel alone are very close to limits obtained by combining all channels. For $m_H \lesssim 130$ GeV the $H \to \gamma\gamma$ channel starts to become competitive with the $H \to WW \to l\nu l\nu$ channel and for $m_H \gtrsim 190$ GeV the $H \to ZZ \to 4l$ channel becomes important so that considering the $H \to WW \to l\nu l\nu$ channel alone for these masses would give us weaker sensitivity estimates compared to estimates evaluated by combining all channels.

For our computations we will use the expected Standard Model (SM) signal (S_{SM})

and background (B) values for $\mathcal{L} = 1$ fb^{-1} integrated luminosity given in Ref. [1]. The values for S_{SM} and B for the $H \rightarrow WW \rightarrow l\nu l\nu$ channel have been given in Ref. [1] as a function of the putative mass of the Higgs m_H used for the search. The only m_H-dependent cut that has been applied in Ref. [1] is,

$$(4.4) \qquad\qquad m_T \leq m_H$$

where the transverse mass m_T is defined by $m_T = \sqrt{(E_T^{ll} + E_T^{miss})^2 - (\mathbf{P}_T^{ll} + E_T^{miss})^2}$, the transverse momentum of the lepton pair, $\mathbf{P}_T^{ll} = \mathbf{P}_T^{l1} + \mathbf{P}_T^{l2}$, $E_T^{ll} = \sqrt{P_T^{ll\ 2} + m_{ll}^2}$, E_T^{miss} is the missing transverse energy and m_{ll} is the invariant mass of the leptons [17]. This cut utilizes the fact that for a Higgs decaying to $l\nu l\nu$, m_T is always less than the Higgs mass. The other cuts used in Ref. [1] have been described in more detail in Ref. [91] .

For evaluating exclusion confidence levels and discovery significances we use simple event counting estimates assuming a Gaussian distribution for the expected number of events. We review the procedure for setting exclusion limits and finding significances in detail in the Appendix D. For the exclusion estimates we use the fact that a signal value S still allowed after applying 95% confidence level exclusion bounds must satisfy,

$$(4.5) \qquad\qquad \frac{S}{\sqrt{S + B + (\Delta B)^2}} \leq 1.64.$$

Here ΔB is the systematic error. As far as significance estimates are considered we use the significance estimator (defined as S_{c12} in [92]),

$$(4.6) \qquad\qquad Z_0 = 2(\sqrt{S+B} - \sqrt{B})\sqrt{\frac{B}{B + (\Delta B)^2}}.$$

Taking $\Delta B/B = 0.15$ we find projections for the 95% upper limit on S/S_{SM} that can be put with $\mathcal{L} = 1$ fb^{-1}. As values of the signal and background have been
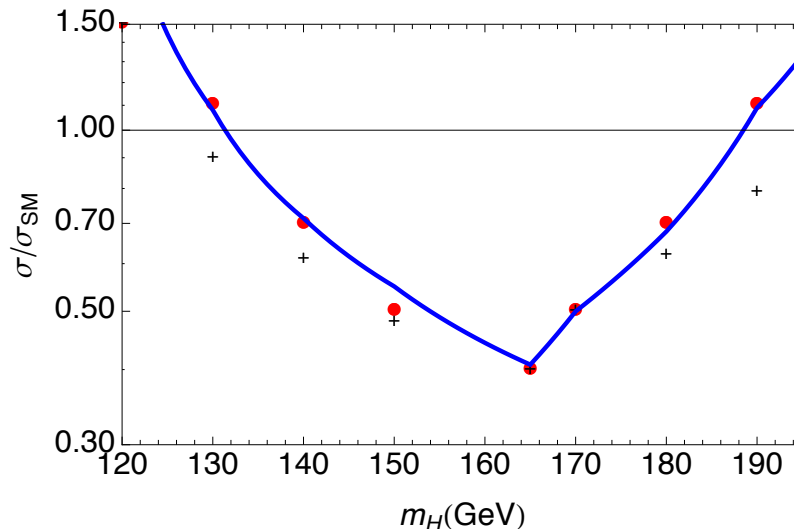
Figure 4.1: The multiple of the cross-section of a Standard Model Higgs boson which can be excluded at 95% confidence level using 1 fb^{-1} LHC data at 7 TeV by the $h \to WW \to l\nu l\nu$ channel. For comparison we also show the ATLAS projections that appear in Ref. [1] for the $h \to WW \to l\nu l\nu$ channel (red dots) and after combining all channels ("+" signs).

given only for a discrete set of masses in Ref. [1], for intermediate masses we have linearly interpolated. The results, shown in Fig.4.1, agree very well with ATLAS projections for the reach of the $H \to WW \to l\nu l\nu$ channel (red dots in Fig.4.1). We also show in Fig.4.1 the projected ATLAS limits obtained in Ref. [1] after combining all the channels. The numerical value $\Delta B/B = 0.15$ has been chosen to get maximum agreement with the ATLAS projections in Ref. [1]. As mentioned earlier after combining all the channels stronger limits can be obtained although the limits from the $H \to WW \to l\nu l\nu$ channel alone are close to the combined limits for 130 GeV $< m_H <$ 190 GeV.

4.3 Significance with mixed-in Higgs bosons.

As can be seen from Fig.4.1 even if the SM Higgs is excluded at a certain mass it is still possible to have a Higgs boson at that mass if the production cross-section times branching ratio is suppressed by ξ compared to the SM. We want to consider the

scenario where there are two Higgs scalars, H and h, and the production cross-section times branching ratio of these Higgs bosons is suppressed according to Eq. (4.3). We will always take $\xi > 0.5$ so that H will always be the SM-like Higgs. For a sufficiently large ξ it would be hard to detect the scalar H. In a situation where only H is detected, deviations from SM can still be detected if the cross-section for production of H, which would be smaller than the SM expectation, can be measured. As we will see, however, it may not always be easy to detect such a deviation in the cross-section.

We will now describe how the $H \to WW \to l\nu l\nu$ significance plots are distorted for the scenario mentioned above. An important difference from the last section is that instead of using the cut in Eq. (4.4) for the search we use the sliding mass window,

$$(4.7) \qquad\qquad 0.75\ m_H < m_T < m_H.$$

This is the cut being used by ATLAS in their present searches [93–95]. The background B after applying the above cut can be easily calculated from the background values given in Ref. [1] where the cut in Eq. (4.4) has been applied, by using [2]

$$B(0.75\ m_H < m_T < m_H) =$$

$$(4.8) \qquad\qquad B(m_T < m_H) - B(m_T < 0.75\ m_H).$$

We show in Fig.4.2 the background obtained by applying the cut in Eq. (4.7). One can similarly reconstruct the background m_T-distribution. For a particular m_H-bin, we will get a cross-section equal to,

$$(4.9) \qquad\qquad B(m_T < m_H) - B(m_T < m_H - 10\text{GeV}).$$

---

[2]In Ref. [1] background values for $B(m_T < m_H)$ for $m_H < 120$ GeV have not been provided; for $m_H < 120$ GeV we use the shape of the m_T-distribution curves for the background provided in [93] keeping the normalization of Ref. [1]. Note that [93] considers the signal and background only for the $H + 0$ jet and $H + 1$ jet analyses whereas Ref. [1] also consider the subdominant $H + 2$ jet contribution.

There is a subtlety which must be kept in mind if this cut is used for discovery searches and not just for setting exclusion limits. If a Higgs boson does exist at a certain mass $m_{h/H}^{true}$, we will obtain a significance after applying the sliding mass cut above, even for Higgs masses different from $m_{h/H}^{true}$. Thus instead of a sharp peak in significance at $m_{h/H}^{true}$ a broad excess would be seen around $m_{h/H}^{true}$, and the peak significance would not necessarily be obtained at $m_{h/H}^{true}$ if the background after applying the above cut is not flat with respect to m_H. As shown in Fig.4.2 the background rises for $m_H \lesssim 135$ GeV and falls for $m_H \gtrsim 150$ GeV. Consider the case of a Higgs boson with $m_H^{true} = 125$ GeV. Although the signal is maximum if one takes $m_H = 125$ GeV in the sliding window in Eq. (4.7), the background is smaller for lower values of m_H, as shown in Fig.4.2, so that the maximum significance is obtained at a mass lower than the 125 GeV. This can be seen from $\xi = 1$ curve in Fig.4.4 that shows the significance vs. m_H curve peaking below 125 GeV. Note, the plot was made for $\xi = 1$ but it would have the same shape (i.e., same peak position) for any ξ value. On the other hand, the significance curve for a 170 GeV Higgs would peak at values higher than 170 GeV because the background falls for $m_H > 170$ GeV.

Before discussing an example we mention how the significances scale with integrated luminosity. Because of systematic effects the significances do not scale as $\mathcal{L}^{0.5}$ but as $\mathcal{L}^{\alpha}$ where α varies between 0.3 and 0.6 [1]. In this work we take $\alpha = 0.4$ throughout.

4.4 Example with one extra mixed-in Higgs boson.

We want to illustrate the distortions in the significance plots that arise if there are two Higgs bosons with cross-sections given by Eq. (4.3) but the standard single Higgs search strategy is used. In order to better understand the significance profiles
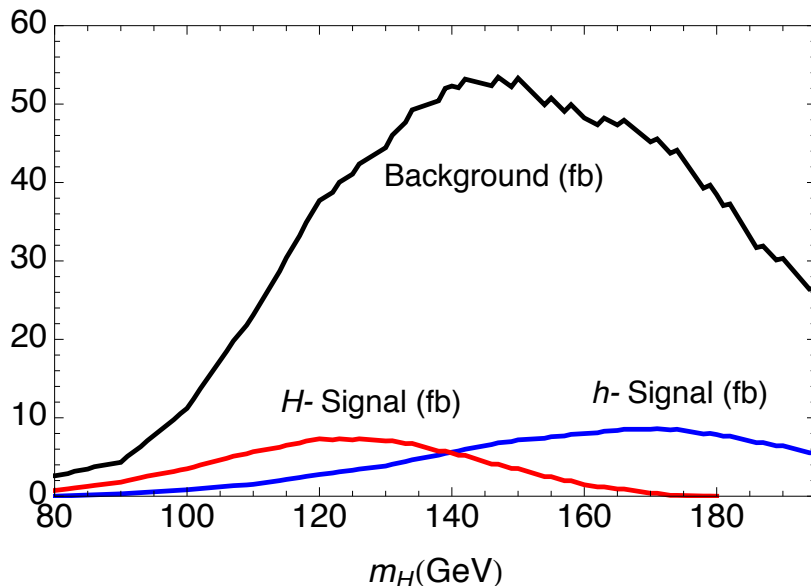
Figure 4.2: The signal cross-section for H and h with $m_H^{true} = 125$ GeV, $m_h^{true} = 170$ GeV and $\xi = 0.8$ and the SM background cross-section after applying the cut in Eq. (4.7).

we need to look at the underlying m_T-distributions for the signal and background first. We take $m_H^{true} = 125$ GeV and $m_h^{true} = 170$ GeV and consider two cases with $\xi = 1$ and $\xi = 0.8$. For the m_T-distribution of the signal we take the shape from Ref. [96] and Ref. [94] for H and h respectively and we use the signal cross-section values provided in Ref. [1] for the normalization. We show the m_T-distributions for the signal plus background taking $\xi = 1$ and $\xi = 0.8$ in Fig.5.6. As one can see even though the production cross-section for h is smaller in the $\xi = 0.8$ case, the m_T distribution hardly changes from the $\xi = 1$ case (the SM limit) in the $m_H < 125$ GeV region of the plot. The reason is that for the $\xi = 0.8$ case, there are extra events from the decay of the scalar h having $m_T < 125$ GeV. As the SM cross-section in this channel at 170 GeV is much higher than the cross-section at 125 GeV this leakage of H-decay events into the $m_H < 125$ GeV region is substantial. For $m_H > 125$ GeV there is a noticeable difference in the $\xi = 0.8$ case as there is now an excess in this region which is not expected for $\xi = 1$. Such an excess can,
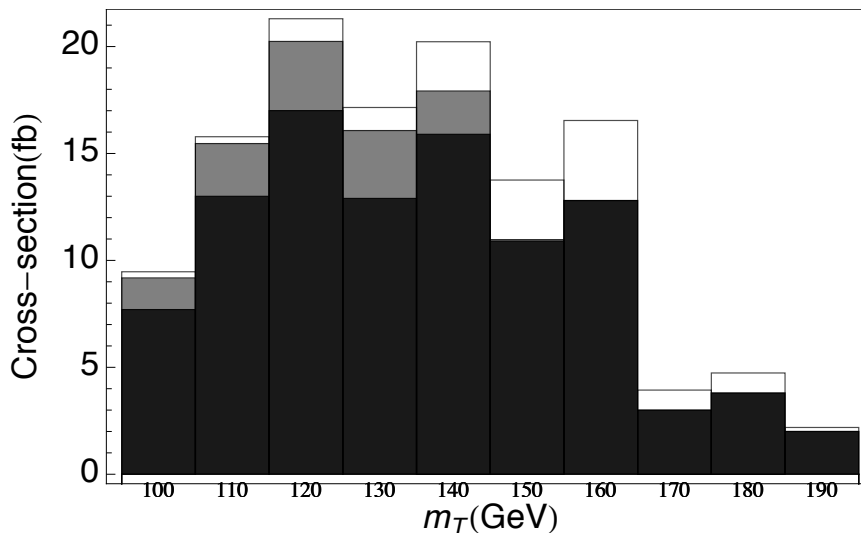
Figure 4.3: We show the m_T-distributions for the background (black) and the signal plus background with $\xi = 1$ (grey) and $\xi = 0.8$ (white). We have taken $m_H^{true} = 125$ GeV and $m_h^{true} = 170$ GeV. In the $\xi = 0.8$ case the effect of the 170 GeV Higgs can be seen in the presence of the excess for $m_H > 125$ GeV.

however, easily be misinterpreted as an error in background modeling or a background fluctuation. If such an excess persists, to ascertain whether it is due to a mixed-in scalar or a background modeling error, would require more effort in reanalyzing and understanding the different backgrounds. To quantify the significance of this excess we need to look at the significance plots shown in Fig.4.4 and Fig.4.5. As can be seen from Fig.4.4 and Fig.4.5 there is no noticeable feature at 170 GeV. Also the significance at 125 GeV does not decrease (in-fact it marginally increases) when we go from $\xi = 1$ to $\xi = 0.8$. This is again because of the above mentioned extra events from the decay of the scalar H having $m_T < 125$ GeV that leak into the "125 GeV signal".

The Higgs boson at 125 GeV would also be seen in the $H \rightarrow ZZ \rightarrow 4l$ and $H \rightarrow \gamma\gamma$ channels with much better mass resolution. The cross-section can, however, not be measured accurately with 15 fb^{-1} data because of statistical uncertainties. This is because a 20 % reduction in the cross-section would be less than even a one
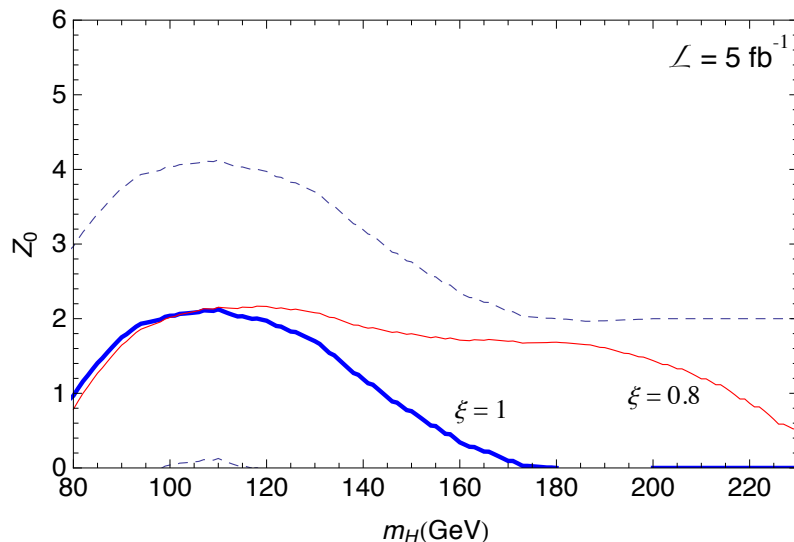
Figure 4.4: The significance vs m_H curve for 5 fb^{-1} data after applying the sliding mass cut in Eq. (4.7) on the signal and background assuming $m_H^{true} = 125$ GeV and $m_h^{true} = 170$ GeV. We show the curve for $\xi = 0.8$ and $\xi = 1$. The dashed line shows the 2-sigma band around the $\xi = 1$ line.

sigma downward fluctuation. As far as the 170 GeV Higgs is concerned neither the $H \to ZZ \to 4l$ channel nor the $H \to \gamma\gamma$ channel is sensitive to it with 15 fb data for $(1 - \xi) = 0.2$.

Thus we see that in the scenario mentioned none of the measurements discussed so far would give any clear indication of the presence of the 170 GeV scalar. The only difference between the $\xi = 1$ and $\xi = 0.8$ case would be in the shape of the significance vs m_H curve, which is due to a difference in the underlying m_T-distribution. As can be seen from Fig.4.4 and Fig.4.5 the significance falls off much more sharply in the $\xi = 1$ case. The $\xi = 0.8$ curve lies within the two-sigma bands around the median $\xi = 1$ expectation for low luminosities (see Fig.4.4) and the difference in shape becomes significant only at higher luminosities (see Fig.4.5).

To disentangle the signal for h one can treat signal due to a supposed SM Higgs at 125 GeV as part of the background. The mass of the lighter Higgs can be inferred from excesses that would exist in other channels like $H \to ZZ \to 4l$ and $H \to \gamma\gamma$.
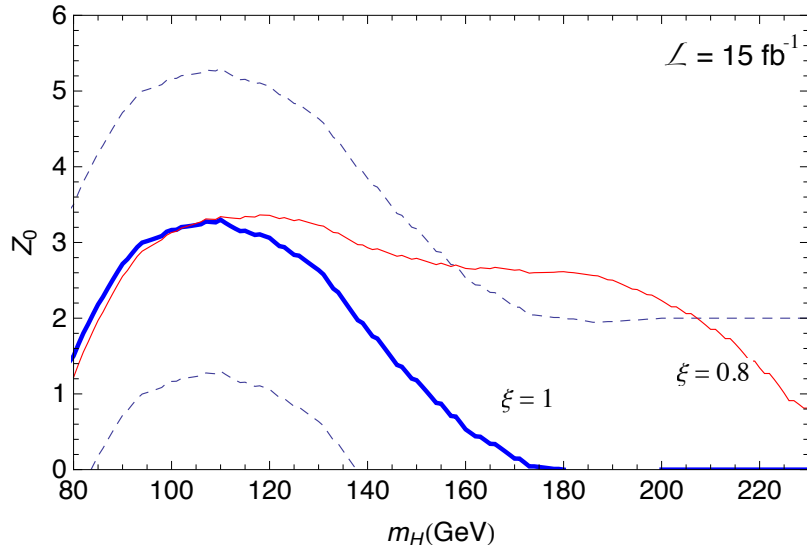
Figure 4.5: The significance vs m_H curve for 15 fb^{-1} data after applying the sliding mass cut in Eq. (4.7) on the signal and background assuming $m_H^{true} = 125$ GeV and $m_h^{true} = 170$ GeV. We show the curve for $\xi = 0.8$ and $\xi = 1$. The dashed line shows the 2-sigma band around the $\xi = 1$ line.

This leads to a curve (Fig.4.6) which peaks in the high mass region. For 10 fb^{-1} luminosity we get almost a three-sigma excess which indicates the presence of a heavier Higgs boson in addition to the Higgs at 125 GeV. Note that we are subtracting the SM contribution for a 125 GeV Higgs whereas in reality the Higgs boson H at 125 GeV has a reduced cross-section with $\xi = 0.8$, and so the subtraction is unwittingly too large. The dashed curve in Fig.4.6 shows the significance curve if the correct light Higgs contribution with $\xi = 0.8$ is subtracted from the signal and included in the background. Note that the peak position, even for the dashed curve is somewhat displaced to masses higher than 170 GeV. This is because of the falling background at 170 GeV as discussed below Eq. (4.9).

Finally let us comment on the CMS Higgs search analysis. Although both the ATLAS and CMS analyses have similar sensitivities, the CMS analysis is more in-volved as the cuts have been optimized individually for each Higgs boson mass [97]. The basic qualitative features that we have highlighted here, however, should still
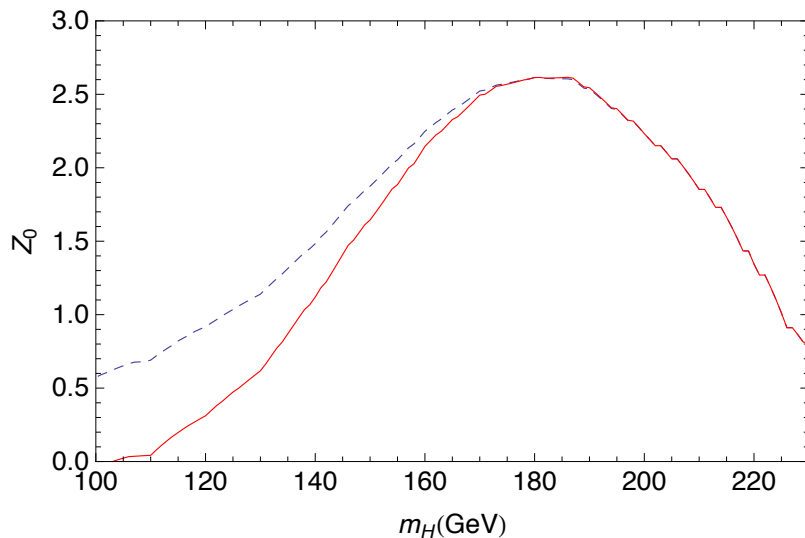
Figure 4.6: The significance vs m_H curve for 15 fb^{-1} data after applying the sliding mass cut in Eq. (4.7) on the signal and background, assuming $m_H^{true} = 125$ GeV, $m_h^{true} = 170$ GeV, $\xi = 0.8$ and treating the contribution of a SM Higgs at 125 GeV as background. The dashed curve shows the significance curve if the correct light Higgs contribution with $\xi = 0.8$ is subtracted from the signal and included in the background.

be true for the CMS analysis. Even in the CMS study Higgs bosons would show up as broad resonances in the $h/H \to WW \to 2l2\nu$ channel, in most of the mass region considered here, before they are discovered in other channels with better mass resolution. Thus even in the CMS study the shape of the significance plots would be crucial for distinguishing an SM Higgs scenario from the case where there is an additional mixed-in scalar state. For the specific example we have considered even in the CMS study one expects that a heavier Higgs at 170 GeV, even with smaller couplings, would have substantial leakage of events to the signal window of a Higgs with lower mass and that the significance plot would have a longer tail if there is an additional heavier Higgs. To see how our results still hold for the CMS study as far as the details are concerned, however, a thorough analysis needs to be done with the CMS cuts.

4.5   Conclusions.

In this letter we have considered two mixed-in scalars having masses in the range where $h/H \to WW \to 2l2\nu$ channel is sensitive. We find no dilution of significance of the 'SM-like' Higgs boson expected because of the mixing, because of leakage of events from the other scalar into its signal region. Nevertheless, with one extra mixed-in exotic Higgs boson, the shape of the significance plot for Higgs boson discovery in the $WW \to 2l2\nu$ channel – even while performing search for one SM Higgs – gets altered in a way that might reveal the existence of this other Higgs boson. The presence of the other scalar leads to a broadening of the excess over a larger mass range relative to the minimal SM Higgs case. In such a situation we propose that the second scalar can be more clearly identified by subtracting the contribution due to the 'SM-like' Higgs

Of course, the total production rate for the 'SM-like' Higgs, which could be measured in other channels like $H \to \gamma\gamma$ and $H \to ZZ \to 4l$, would be off compared to the SM in the event that the Higgs boson is mixed-in with a scalar. The QCD uncertainties of production rate, and the statistical uncertainties that would be present in the initial phase of discovery would, however, be large enough that distortions in the $H \to WW \to 2l2\nu$ significance plot may be more revealing than simple accounting for the total rate.

CHAPTER V

Probing Quartic Neutral Gauge Couplings by diffractive photon fusion at the LHC

5.1 Introduction

The Standard Model has been tested very accurately by experiments. There are, however, many theoretical reasons to believe that there is physics beyond the SM. Some of these motivations, like the hierarchy problem and the existence of dark matter, point to the existence of new physics at the TeV scale. LEP-2 precision data and flavor constraints seem to favor a scenario with a mass gap between a light Higgs ($m_H \lesssim 200$ GeV) and new physics at the scale of a few TeV. A model independent way of parametrizing the effects of new physics in such a scenario is to use the effective field theory approach. All possible operators allowed by the symmetries of the theory are included, suppressed by appropriate powers of the cut-off Λ. If Λ is the order of a few TeV, these operators can be directly measured at the Large Hadron Collider.

These operators are expected to give rise to anomalous triple and quartic gauge couplings. In this chapter we discuss a special class of these couplings: the Quartic Neutral Gauge Boson Couplings (QNGC), that is, quartic vertices involving only the neutral gauge bosons, γ and Z. QNGCs are special because as we will show they do not exist in the SM and receive their lowest order contributions from dimension

8 operators. Thus the measurement of these couplings would indicate directly the presence of dimension 8 operators[1] in a scenario where a light Higgs is present. This is not true, for example, in the case of $\gamma\gamma W^+W^-$ and ZZW^+W^- couplings which get contributions from the SM lagrangian and its dimension 6 extension [98]. Thus QNGCs can be very useful in probing new physics scenarios with a light Higgs that exclusively generate dimension 8 operators. One such example that generates only dimension 8 operators at tree-level is the exchange of the spin 2 Kaluza-Klein excitations of the graviton in models with large extra dimensions. We will see how integrating out these massive modes generates QNGCs and how probing these couplings would allow us to probe the fundamental Planck scale in these extra dimensional theories.

We also consider the higgsless case where electroweak symmetry is non-linearly realized. In this case, with the exception of the $ZZZZ$ coupling, QNGCs do not appear at the dimension 4 level and the lowest order contribution comes from dimension 6 operators. This is unlike quartic gauge couplings having $W^{+/-}$ bosons which always appear first at the dimension 4 level. Thus in this case also, unlike processes involving quartic gauge couplings with $W^{+/-}$ bosons, processes involving QNGCs can directly probe higher order operators (in this case dimension 6 operators).

In this chapter we will explore the possibility of measuring the $\gamma\gamma\gamma\gamma$ and $\gamma\gamma ZZ$ couplings in the diffractive photon fusion processes, $pp(\gamma\gamma \to \gamma\gamma)pp$ and $pp(\gamma\gamma \to ZZ)pp$ (see Fig. 5.1) respectively. There are plans to install very forward detectors by the ATLAS and CMS collaborations [99] which can detect protons that scatter diffractively at small angles and thus can identify such processes. To the best of our knowledge, this is the first study on the LHC sensitivity of the measurement of the

---

[1]In the case of the $\gamma\gamma ZZ$ coupling there is a non-local contribution from the $\gamma\gamma \to H^* \to ZZ$ process which is of an order lower than dimension 8 contributions. However, as we discuss later, this contribution can be subtracted if the $H \to \gamma\gamma$ partial width is known.
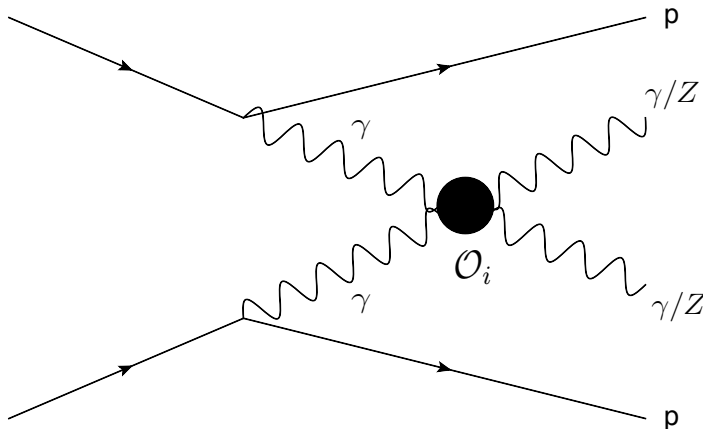
Figure 5.1: The diffractive photon fusion processes $pp(\gamma\gamma \to \gamma\gamma)pp$ and $pp(\gamma\gamma \to ZZ)pp$. The outgoing protons can be detected by very forward detectors to be installed by ATLAS and CMS. In the figure above $\mathcal{O}_i$ represents operators contributing to Quartic Neutral Gauge Couplings (QNGCs).

$\gamma\gamma\gamma\gamma$ coupling. There have been previous studies for the $\gamma\gamma ZZ$ coupling, but these studies focussed only on the higgsless case. In Refs. [100, 101] probing the $\gamma\gamma ZZ$ coupling by inelastic processes like $pp \to \gamma\gamma\gamma$, $pp \to \gamma\gamma Z$ and $pp \to jj(ZZ \to \gamma\gamma) \to jj\gamma\gamma$ has been studied, whereas, in Refs. [102–104] measurement of this coupling in the diffractive process $pp(\gamma\gamma \to ZZ)pp$, that we will study in this work too, has been explored. In this work, however, we consider both the light Higgs and the higgsless cases. As we will see, in the higgsless case considered in the previous studies only a subset of all the operators relevant to the light Higgs case are important.

Let us now see what are the advantages of diffractive photon fusion processes in measuring these couplings. Even if a process can be traced back to a definite set of operators as is the case here, it is rarely the case that a particular collider signature can be traced back to a unique process. For this reason many different, complementary measurements are usually required to uncover the underlying new physics processes. For example consider the inelastic counterpart of the signature we are considering for the $\gamma\gamma ZZ$ coupling, the $pp \to jj(\gamma\gamma \to ZZ) \to jjZZ$ process

or the similar vector boson fusion (VBF) process $pp \rightarrow jj(ZZ \rightarrow \gamma\gamma) \rightarrow jj\gamma\gamma$.
Although these signatures would have a much larger cross-section than the diffractive
signature we are considering, if an excess is observed in the $jjZZ$ or $jj\gamma\gamma$ final
states it would be hard to reconstruct the exact process responsible for it because
of the many different new physics processes in addition to QNGCs that can have
this signature[2]. The triple gauge boson production processes $pp \rightarrow \gamma\gamma Z$ (studied
previously in Ref. [100, 101]) and $pp \rightarrow \gamma\gamma\gamma$ are somewhat better in this respect but,
again, because the intermediate state in $pp \rightarrow \gamma\gamma Z(\gamma\gamma\gamma)$ cannot be known, it would
not be possible to conclude with certainty that QNGCs are responsible, if an excess
is seen. The diffractive signals we study in this work are interesting because exclusive
final states where two protons have been detected in the forward detectors can arise
only from diffractive photon fusion or exclusive pomeron fusion. In the latter case
the underlying subprocess would be $gg \rightarrow \gamma\gamma/ZZ$. Thus the inverse problem of
pinning down the new physics responsible for an excess in the $pp\gamma\gamma$ and $ppZZ$ final
states is relatively less ambiguous as there are only two new physics possibilities
namely the enhancement of the $\gamma\gamma \rightarrow \gamma\gamma/ZZ$ processes and/or the enhancement
of the $gg \rightarrow \gamma\gamma/ZZ$ processes. As we will discuss later, exclusive pomeron fusion
processes are, however, expected to have a much smaller cross-section as compared
to photon fusion processes.

---

[2]The $pp \rightarrow jj(\gamma\gamma \rightarrow ZZ) \rightarrow jjZZ$ process is experimentally challenging for a separate reason too which is that
the two jets would not have the special properties of VBF jets. VBF jets have a large rapidity gap between them
and have high p_T (see for example pg. 1271-1305 of [49]). For reasons mentioned in Section 5.5 the p_T of the jets
in the process $pp \rightarrow jj(\gamma\gamma \rightarrow ZZ) \rightarrow jjZZ$ is approximately equal to the photon virtuality and thus expected to be
very small. So while the photon fusion jets would have a large rapidity gap too, they will have very low p_T

5.2 Operators that give rise to Quartic Neutral Gauge Boson Couplings

5.2.1 Light Higgs case

We want to write down the lowest order contribution form higher dimensional operators to QNGCs, that is, quartic vertices involving only the neutral gauge bosons γ and Z. We will consider only CP conserving operators here hence we will not use the dual field strength tensors like $\tilde{B}_{\mu\nu}$. In gauge invariant operators the electroweak vector boson fields can appear either from the field strengths $B_{\mu\nu}$ and $W^I_{\mu\nu}$ or covariant derivatives acting on the Higgs field, that is factors like,

$$(5.1) \qquad D_\mu\Phi = \partial_\mu\Phi - ig\frac{\tau_I}{2}W^I_\mu\Phi - i\frac{g'}{2}B_\mu\Phi,$$

provided the Higgs field, Φ, gets a vacuum expectation value (VEV). In the above equation τ_I are the Pauli matrices. Note that the $\epsilon_{IJK}W_J W_K$ part of $W^I_{\mu\nu}$ cannot contribute to quartic neutral gauge boson couplings as we must have $I = J = 3$ to get photons or Z fields unlike for instance in the case of the $\gamma\gamma W^+W^-$ coupling, where two gauge boson fields can come from the same field strength tensor $W^I_{\mu\nu}$. This has the important implication that the lowest order contribution to quartic neutral gauge boson couplings comes from dimension 8 operators[3] because we need either a field strength or $D_\mu\Phi$ factor, both dimension 2 operators, for each of the four gauge bosons. There must be an even number of $D_\mu\Phi$ factors along with the field strength tensors in these operators because otherwise there are an odd number of Lorentz indices in total and it is impossible to contract all of them. Thus we see that the operators we are interested in can have either four covariant derivatives, two field strengths and two covariant derivatives or four field strengths. We thus obtain the

---

[3]This fact is also true for $gg\gamma\gamma$ and $ggZZ$ couplings (g being the gluon).

following lagrangian of dimension 8 operators,

$$
\begin{aligned}
\mathcal{L}_{QNGC} &= \frac{c_1}{\Lambda^4} D_\mu \Phi^\dagger D^\mu \Phi D_\nu \Phi^\dagger D^\nu \Phi + \frac{c_2}{\Lambda^4} D_\mu \Phi^\dagger D_\nu \Phi D^\mu \Phi^\dagger D^\nu \Phi + \frac{c_3}{\Lambda^4} D_\rho \Phi^\dagger D^\rho \Phi B_{\mu\nu} B^{\mu\nu} \\
&+ \frac{c_4}{\Lambda^4} D_\rho \Phi^\dagger D^\rho \Phi W^I_{\mu\nu} W^{I\mu\nu} + \frac{c_5}{\Lambda^4} D_\rho \Phi^\dagger \sigma^I D^\rho \Phi B_{\mu\nu} W^{I\mu\nu} + \frac{c_6}{\Lambda^4} D_\rho \Phi^\dagger D^\nu \Phi B_{\mu\nu} B^{\mu\rho} \\
&+ \frac{c_7}{\Lambda^4} D_\rho \Phi^\dagger D^\nu \Phi W^I_{\mu\nu} W^{I\mu\rho} + \frac{c_8}{\Lambda^4} B_{\rho\sigma} B^{\rho\sigma} B_{\mu\nu} B^{\mu\nu} + \frac{c_9}{\Lambda^4} W^I_{\rho\sigma} W^{I\rho\sigma} W^J_{\mu\nu} W^{J\mu\nu} \\
&+ \frac{c_{10}}{\Lambda^4} W^I_{\rho\sigma} W^{J\rho\sigma} W^I_{\mu\nu} W^{J\mu\nu} + \frac{c_{11}}{\Lambda^4} B_{\rho\sigma} B^{\rho\sigma} W^I_{\mu\nu} W^{I\mu\nu} + \frac{c_{12}}{\Lambda^4} B_{\rho\sigma} W^{I\rho\sigma} B_{\mu\nu} W^{I\mu\nu} \\
&+ \frac{c_{13}}{\Lambda^4} B_{\rho\sigma} B^{\sigma\nu} B_{\mu\nu} B^{\mu\rho} + \frac{c_{14}}{\Lambda^4} W^I_{\rho\sigma} W^{I\sigma\nu} W^J_{\mu\nu} W^{J\mu\rho} + \frac{c_{15}}{\Lambda^4} W^I_{\rho\sigma} W^{J\sigma\nu} W^I_{\mu\nu} W^{J\mu\rho} \\
&+ \frac{c_{16}}{\Lambda^4} B_{\rho\sigma} B^{\sigma\nu} W^I_{\mu\nu} W^{I\mu\rho} + \frac{c_{17}}{\Lambda^4} B_{\rho\sigma} W^{I\sigma\nu} B_{\mu\nu} W^{I\mu\rho}.
\end{aligned}
$$

(5.2)

Thus we obtain seventeen independent operators. Note that, in the above list, $B_{\mu\nu} \epsilon_{IJK} W^{I\mu\nu} W^J_{\rho\sigma} W^{K\rho\sigma}$, $B_{\mu\nu} \epsilon_{IJK} (\Phi^\dagger \sigma^I \Phi) W^J_{\rho\sigma} W^{K\rho\sigma}$ and $B_{\mu\nu} \epsilon_{IJK} W^{I\mu\rho} W^{J\nu\sigma} W^K_{\rho\sigma}$ are absent because they are all equal to zero. In the first two cases ϵ_{IJK} is antisymmetric in J and K whereas the rest of the operator is symmetric in J and K and in the third case $B_{\mu\nu}$ is antisymmetric in μ and ν whereas the rest of the operator is symmetric in μ and ν. Operators with two σ^Is do not appear above as these can be reduced to operators in our list using the identity, $\sigma^I \sigma^J = \delta^{IJ} + i\epsilon^{IJK} \sigma_K$. Also notice that there are no operators like $\Phi^\dagger D^\mu D_\nu \Phi B_{\mu\rho} B^{\nu\rho}$. This is because such operators can be expressed as linear combinations of total derivatives, operators already in the list and operators that do not contribute to QNGCs, as follows,

$$
\begin{aligned}
\Phi^\dagger D^\mu D_\nu \Phi B_{\mu\rho} B^{\nu\rho} &= \partial^\mu (\Phi^\dagger D_\nu \Phi B_{\mu\rho} B^{\nu\rho}) - D^\mu \Phi^\dagger D_\nu \Phi B_{\mu\rho} B^{\nu\rho} \\
&\quad - \Phi^\dagger D_\nu \Phi \partial^\mu (B_{\mu\rho} B^{\nu\rho})
\end{aligned}
$$

(5.3)

where we have used $\partial_\mu (\Phi^\dagger D_\nu \Phi) = D_\mu \Phi^\dagger D_\nu \Phi + \Phi^\dagger (D_\mu D_\nu \Phi)$. Finally, operators with two Levi Civita tensors,like $\epsilon_{\mu\nu\rho\sigma} \epsilon_{\alpha\beta\gamma\delta} B^{\mu\alpha} B^{\nu\beta} B^{\rho\gamma} B^{\sigma\delta}$, which corresponds to taking

two dual field strength tensors, are not in the list. This is because using the identity,

$$(5.4) \qquad \epsilon_{i_1 i_2 i_3 i_4} \epsilon_{j_1 j_2 j_3 j_4} = 24 \, g_{j_i k_i} g_{j_2 k_2} g_{j_3 k_3} g_{j_4 k_4} \delta^{k_1}_{[i_i} ... \delta^{k_4}_{i_4]}$$

we can express such operators in terms of operators contracted using metric tensors which are already in our list.

If we rewrite these operators in terms of the fields A and Z defined by,

$$(5.5) \qquad \begin{pmatrix} B \\ W_3 \end{pmatrix} = \begin{pmatrix} c_w & -s_w \\ s_w & c_w \end{pmatrix} \begin{pmatrix} A \\ Z \end{pmatrix}$$

and the field strengths,

$$
\begin{aligned}
F_{\mu\nu} &= \partial_\mu A_\nu - \partial_\nu A_\mu \\
(5.6) \qquad Z_{\mu\nu} &= \partial_\mu Z_\nu - \partial_\nu Z_\mu.
\end{aligned}
$$

we will get $ZZZZ$, γZZZ, $\gamma\gamma ZZ$, $\gamma\gamma\gamma Z$ and $\gamma\gamma\gamma\gamma$ couplings. In this work we will explore the possibility of measuring these vertices by diffractive processes involving photon exchange, that is processes like $pp(\gamma\gamma \to X)pp$. Such processes can measure the $\gamma\gamma ZZ$, $\gamma\gamma\gamma Z$ and $\gamma\gamma\gamma\gamma$ vertices but we will focus only on the $\gamma\gamma ZZ$ and $\gamma\gamma\gamma\gamma$ vertices here (we give the complete list of the $\gamma\gamma\gamma Z$, γZZZ and $ZZZZ$ couplings in Appendix A). Expressing the operators above in terms of A and Z fields and the respective field strengths using Eq. (5.5) and Eq. (5.6) we get,

$$
\begin{aligned}
\mathcal{L}^{\gamma\gamma\gamma\gamma}_{QNGC} &= \frac{a_1^{\gamma\gamma}}{\Lambda^4} F_{\mu\nu} F^{\mu\nu} F_{\rho\sigma} F^{\rho\sigma} + \frac{a_2^{\gamma\gamma}}{\Lambda^4} F_{\mu\nu} F^{\mu\rho} F_{\rho\sigma} F^{\sigma\nu} \\
\mathcal{L}^{\gamma\gamma ZZ}_{QNGC} &= \frac{a_1^{ZZ}}{\Lambda^4} \frac{m_Z^2}{2} F_{\mu\nu} F^{\mu\nu} Z_\rho Z^\rho + \frac{a_2^{ZZ}}{\Lambda^4} \frac{m_Z^2}{2} F_{\mu\nu} F^{\mu\rho} Z_\rho Z^\nu + \frac{a_3^{ZZ}}{\Lambda^4} F_{\mu\nu} F^{\mu\nu} Z_{\rho\sigma} Z^{\rho\sigma} \\
(5.7) \qquad & \quad + \frac{a_4^{ZZ}}{\Lambda^4} F_{\mu\nu} Z^{\mu\nu} F_{\rho\sigma} Z^{\rho\sigma} + \frac{a_5^{ZZ}}{\Lambda^4} F_{\mu\nu} F^{\mu\rho} Z_{\rho\sigma} Z^{\sigma\nu} + \frac{a_6^{ZZ}}{\Lambda^4} F_{\mu\nu} Z^{\mu\rho} F_{\rho\sigma} Z^{\sigma\nu}
\end{aligned}
$$

where,

$$a_1^{\gamma\gamma} = c_w^4 c_8 + s_w^4 c_9 + c_w^2 s_w^2 (c_{10} + c_{11})$$

$$a_2^{\gamma\gamma} = c_w^4 c_{13} + s_w^4 c_{14} + c_w^2 s_w^2 (c_{15} + c_{16})$$

$$a_1^{ZZ} = c_w^2 c_3 + s_w^2 c_4 - c_w s_w c_5$$

$$a_2^{ZZ} = c_w^2 c_6 + s_w^2 c_7$$

$$a_3^{ZZ} = 2c_w^2 s_w^2 (c_8 + c_9 + c_{10}) + (s_w^4 + c_w^4)c_{11} - 2c_w^2 s_w^2 c_{12}$$

$$a_4^{ZZ} = (c_w^2 - s_w^2)^2 c_{12} + 4c_w^2 s_w^2 (c_8 + c_9 + c_{10}) - 4c_w^2 s_w^2 c_{11}$$

$$a_5^{ZZ} = 4c_w^2 s_w^2 (c_{13} + c_{14} + c_{15}) + (s_w^4 + c_w^4 - 2c_w^2 s_w^2)c_{16} - 4c_w^2 s_w^2 c_{17}$$

$$(5.8) \quad a_6^{ZZ} = (c_w^4 + s_w^4)c_{17} + 2c_w^2 s_w^2 (c_{13} + c_{14} + c_{15}) - 2c_w^2 s_w^2 c_{16}.$$

We have thus listed all operators that contribute to the $\gamma\gamma\gamma\gamma$ and $\gamma\gamma ZZ$ vertices. Note that c_1 and c_2 do not appear in the RHS in Eq. (5.8) because the corresponding operators contribute only to the $ZZZZ$ coupling. As we want to measure these couplings by the $\gamma\gamma \to \gamma\gamma$ and $\gamma\gamma \to ZZ$ processes respectively, let us also list operators that might enhance non-local background contributions through the processes like $\gamma\gamma \to X^* \to \gamma\gamma/ZZ$ at the same order, where X is some SM field. We find that the only dimension 6 operators giving such non-local contributions at the same order are those that contribute via the $\gamma\gamma \to H^* \to ZZ$ processes due to the anomalous $H\gamma\gamma$ couplings they introduce. These operators (already listed in Ref. [98]) are,

$$(5.9) \quad \mathcal{L}_6 = \frac{b_1}{\Lambda^2}|\Phi|^2 B_{\mu\nu}B^{\mu\nu} + \frac{b_2}{\Lambda^2}|\Phi|^2 W_{\mu\nu}^I W^{I\mu\nu} + \frac{b_3}{\Lambda^2}(\Phi^\dagger \sigma_I \Phi)B_{\mu\nu}W^{I\mu\nu}.$$

which give the following dimension 5 operator once the Higgs field, Φ, gets a VEV,

$$(5.10) \quad \frac{a_0 v}{\Lambda^2}HF_{\mu\nu}F^{\mu\nu}$$

where $v = 246$ GeV and,

$$(5.11) \quad a_0 = c_w^2 b_1 + s_w^2 b_2 - c_w s_w b_3.$$

Note that heavy particles that interact with the Higgs boson and photons generally induce this operator when integrated out. Fortunately, the coupling a_0 can be accurately measured at the LHC by measuring the $H \to \gamma\gamma$ partial width. Thus the effect of the only dimension 6 operator that contributes to the cross section can be subtracted.

We have not identified couplings for $\gamma\gamma X$ or XZZ, that arise from dimension > 6 operators and contribute to this process by an X exchange, because these contributions would have the dependance $\sim 1/\Lambda^n$ with $n > 4$ which would be of higher order than dimension 8 which is the lowest order at which the QNGCs get a contribution.

5.2.2 Higgsless case

Note that our treatment in the previous subsection differs from that in Refs. [100–102] where only the $\gamma\gamma \to ZZ$ process has been discussed. Among all the terms in Eq. (5.7) the authors consider only the operators $\mathcal{O}_1^{ZZ}$ and $\mathcal{O}_2^{ZZ}$ (i.e., the operators that have the coefficients a_1^{ZZ} and a_2^{ZZ} respectively). This can be justified if there is no light Higgs and electroweak symmetry breaking (EWSB) is non-linearly realized at low energies. Let us see why this is so. We follow the construction of Burgess et al. (Ref. [105]), use the matrix,

$$(5.12) \qquad \Sigma = \exp(2iX_i\pi_i/v)$$

and the covariant derivative,

$$(5.13) \qquad D_\mu\Sigma = \Sigma^\dagger\partial_\mu\Sigma - i\Sigma^\dagger[gW_\mu^a T_a + g'B_\mu Y]\Sigma.$$

to define the following fields,

$$
\begin{aligned}
e\mathcal{A}_\mu &= 2i \ \mathrm{Tr}[X_{em}D_\mu\Sigma] \\[2mm]
\frac{g}{2c_w}\mathcal{Z}_\mu &= i \ \mathrm{Tr}[X_3 D_\mu\Sigma] \\[2mm]
g\mathcal{W}^\pm_\mu &= i\sqrt{2} \ \mathrm{Tr}[T_\pm D_\mu\Sigma].
\end{aligned}
$$

(5.14)

Here Y is the hypercharge generator, $T_\pm = T_1 \pm T_2$, where T_i are the SU(2)$_L$ generators. X_{em} and X_3 are orthogonal linear combinations of Y and T_3, X_{em} being the unbroken generator of U(1)$_{em}$. We have kept the unconventional normalization of Ref. [105], viz $\mathrm{Tr}[T_a, T_b] = \frac{1}{2}\delta_{ab}$, $\mathrm{Tr}[T_a, Y] = 0$ and $\mathrm{Tr}[Y^2] = \frac{1}{2}$.

As shown in Ref. [105], the fields $\mathcal{A}$, $\mathcal{Z}$ and $\mathcal{W}^\pm$ in Eq. (5.14) transform purely electromagnetically and exactly like A, Z and $W^\pm$ respectively. In the unitary gauge, $\Sigma \to 1$ so that $\mathcal{A} \to A$, $\mathcal{Z} \to Z$ and $\mathcal{W}^\pm \to W^\pm$. It is thus easy to construct gauge invariant operators we are interested in if EWSB is non linearly realized. In the unitary gauge these are just all possible operators constructed from the A, Z and $W^\pm$ fields that respect the U(1)$_{em}$ symmetry. We get therefore for the $\gamma\gamma ZZ$ coupling,

(5.15)
$$
\mathcal{L}^{Higgsless}_{QNGC} = \frac{(g/2c_w)^2 a^{hl}_1}{\Lambda^2} F_{\mu\nu}F^{\mu\nu}Z_\rho Z^\rho + \frac{(g/2c_w)^2 a^{hl}_2}{\Lambda^2} F_{\mu\nu}F^{\mu\rho}Z_\rho Z^\nu
$$

Note that in this case we get as the lowest order contributions to QNGCs two dimension 6 operators, which are same as as $\mathcal{O}^{ZZ}_1$ and $\mathcal{O}^{ZZ}_2$ in Eq. (5.7), and none of the other operators in Eq. (5.7) are present above. Thus, unlike in the case with the light Higgs boson, these operators are indeed more important here, and this is why they are the only ones that appear in the analyses of Refs. [100–102]. The $\gamma\gamma\gamma$ coupling does not get any contribution at this order.

Another way to understand the above fact is by using the goldstone boson equivalence theorem which states that at high energies longitudinal gauge boson production

processes should have the same amplitude as processes in which the corresponding goldstone bosons are produced. The operators in Eq. (5.15) arise from operators like $c \, \text{Tr}[(D_\mu \Sigma)^\dagger D^\mu \Sigma] F_{\mu\nu} F^{\mu\nu}$. This can be expanded to give the terms involving the goldstones like, $((c/\Lambda^2)(\partial_\rho \vec{\pi} \partial^\rho \vec{\pi}/v^2)) F_{\mu\nu} F^{\mu\nu}$, which tells us that the $\mathcal{A}(\gamma\gamma \to Z_L Z_L)$ amplitude will be $\mathcal{O}(c\hat{s}^2/(v^2\Lambda^2))$, ignoring the dimensionless electroweak couplings. This is larger than the amplitude due to an operator like $((c/\Lambda^4)Z_{\rho\sigma}Z^{\rho\sigma}) F_{\mu\nu} F^{\mu\nu}$, not included in Eq. (5.14), which will give $\mathcal{A}(\gamma\gamma \to ZZ) = \mathcal{O}(c\hat{s}^2/\Lambda^4)$. The crucial difference is that, unlike the light Higgs case, the goldstones here are strongly coupled and suppressed by factors of $1/v$ and not $1/\Lambda$.

5.2.3 Graviton exchange in extra-dimensional theories as a source of QNGCs

In extra-dimensional theories where the fundamental gravity scale can be a few TeV, the graviton is accompanied by Kaluza-Klein (KK) partners in the 4D effective theory. Exchange of the $(4 + \delta)$-dimensional graviton, δ being the number of extra dimensions, can be thought of as the excahnge of the 4D graviton and its massive KK partners. The effective operator induced by tree-level graviton exchange is given by [106],

$$(5.16) \qquad \mathcal{O}_T = \frac{4\pi}{\Lambda_T^4} \left(\frac{T_{\mu\nu}T^{\mu\nu}}{2} - \frac{1}{\delta + 2} \frac{T_\mu^\mu T_\nu^\nu}{2} \right)$$

where $T^{\mu\nu}$ is the energy-momentum tensor. At tree level only dimension 8 operators are induced (at loop level only one dimension 6 operator operator is induced by virtual graviton exchange but this is a four fermion operator not involving the gauge bosons or the Higgs [107]).

Almost all the operators in Eq. (5.2) can be obtained by expanding $T^{\mu\nu}$ in Eq. (5.16). To show this let us write down the energy-momentum tensor for the

B_μ and W_μ^I gauge bosons and the Higgs boson,

$$T_B^{\mu\nu} = -B^{\mu\rho}B_\rho^\nu + \frac{1}{4}g^{\mu\nu}B^{\rho\sigma}B_{\rho\sigma}$$

$$T_W^{\mu\nu} = -W^{I\mu\rho}W_\rho^{I\nu} + \frac{1}{4}g^{\mu\nu}W^{I\rho\sigma}W_{\rho\sigma}^I$$

$$(5.17) \qquad T_\Phi^{\mu\nu} = D^\mu\Phi^\dagger D^\nu\Phi + D^\nu\Phi^\dagger D^\mu\Phi - g^{\mu\nu}(D^\mu\Phi^\dagger D_\mu\Phi - m^2\Phi^\dagger\Phi).$$

Note that virtual graviton exchange will also generate operators involving the gluon field strength, $G_{\mu\nu}^I$, like $G_{\mu\nu}^I G^{I\mu\nu} B_{\rho\sigma} B^{\rho\sigma}$, $G_{\mu\nu}^I G^{I\mu\nu} D^\rho\Phi^\dagger D_\rho\Phi$ etc. Such operators would enhance the signal by contributing to the central exclusive pomeron fusion process (CEP), $pp(CEP \to \gamma\gamma/ZZ)pp$. The luminosity of photons produced by the protons is however higher than the luminosity of the pomerons produced that undergo exclusive fusion (by exclusive we mean that the pomerons do not disintegrate into fragments) by a few orders of magnitude at the high energies where these operators become important (see Fig. 2 in Ref. [108]). Thus the $pp(CEP \to \gamma\gamma/ZZ)pp$ contribution is expected to be negligible compared to the $pp(\gamma\gamma \to \gamma\gamma/ZZ)pp$ contribution. In any case any contribution form this channel would only enhance the signal and thus improve the experimental potential of observing effects of virtual graviton exchange.

5.3 Constraints

QNGCs are very weakly constrained by existing data. There are no constraints on $\gamma\gamma\gamma\gamma$ couplings and the only constraints are on $\gamma\gamma ZZ$ couplings. We first consider the light Higgs case discussed in Section 5.2.1. A LEP analysis [109] based on the $e^+e^- \to Z\gamma\gamma$ process puts the following constraints on the operators $\mathcal{O}_1$ and $\mathcal{O}_2$ in Eq. (5.7),

$$(5.18) \qquad -\frac{1}{(69\,\text{GeV})^4} < \frac{a_1^{ZZ}}{\Lambda^4} < \frac{1}{(93\,\text{GeV})^4}$$

and,

$$(5.19) \qquad -\frac{1}{(65\,\mathrm{GeV})^4} < \frac{a_2^{ZZ}}{\Lambda^4} < \frac{1}{(65\,\mathrm{GeV})^4}.$$

While the authors of Ref. [109] did not carry out their analysis for the other operators in Eq. (5.7), as these are also dimension 8 operators we expect their contribution to these processes to be of a similar magnitude. Thus the constraints on these couplings are also expected to be very weak. Somewhat stronger constraints can be derived from electroweak precision data. In Ref. [101] precision constraints on the operators are derived and they find the bounds, $|a_{1,2}^{ZZ}/\Lambda^4| \lesssim 1/(270\,\mathrm{GeV})^{-4}$, which, as we shall see later, are still far too weak compared to the expected LHC sensitivity.

As the operators in the higgsless case discussed in Section 5.2.2 are exactly the two operators discussed above, the only difference being that we use a different parametrization for the couplings, the same constraints can be translated to the couplings in Eq. (5.15) in the higgsless case,

$$(5.20) \qquad -\frac{1}{(27\,\mathrm{GeV})^2} < \frac{a_1^{hl}}{\Lambda^2} < \frac{1}{(50\,\mathrm{GeV})^2}$$

and,

$$(5.21) \qquad -\frac{1}{(24\,\mathrm{GeV})^2} < \frac{a_2^{hl}}{\Lambda^2} < \frac{1}{(24\,\mathrm{GeV})^2},$$

whereas the precision constraints in Ref. [101] imply $|a_{1,2}^{hl}/\Lambda^2| \lesssim 1/(420\,\mathrm{GeV})^{-2}$.

Now we discuss the constraints on the scale, Λ_T, for virtual graviton exchange, which appears in Eq. (5.16). The strongest constraints on Λ_T come from LHC data at 7 TeV. With 36 pb^{-1} CMS data at 7 TeV the $pp \to jj$ process can be used to derive the constraint $\Lambda_T > 3.8$ TeV [110] at 95 % confidence level. The same process puts the constraint $\Lambda_T > 3.6$ TeV [110] with 36 pb^{-1} ATLAS data at 95 % confidence level. With 1.1 fb^{-1} CMS data, the $pp \to \gamma\gamma$ process puts the weaker constraint

$\Lambda_T > 3.1$ TeV at 95 % confidence level [111], but this process is eventually expected to probe scales up to about $\Lambda_T = 6$ TeV [106].

Finally, consider the operators in Eq. (5.9). At tree level the couplings b_1 and b_2 in Eq. (5.9) renormalize the coefficient of the kinetic terms for the gauge bosons B_μ and W_μ^I which is equivalent to a renormalization of the couplings g' and g. Thus all tree level effects due to the b_1 and b_2 can be absorbed in a redefinition of the couplings and hence these couplings are unconstrained. The coupling b_3 is related to the S-parameter by [112],

$$(5.22) \qquad \frac{b_3}{\Lambda^2} = \frac{\alpha_{em}}{4 s_w c_w v^2} \Delta S$$

Here α_{em} is the fine structure constant $v = 246$ GeV and s_w, c_w are the sine and cosine of the weak mixing angle. The bound on the S-parameter for $m_h = 113$ GeV and with no restrictions on the T parameter is $|\Delta S| \lesssim 0.3$ [112] at 90% confidence level. This translates to the following bound on b_3,

$$(5.23) \qquad \left| \frac{b_3}{\Lambda^2} \right| < \frac{1}{(6.6 \, \text{TeV})^2}.$$

This coupling is also constrained by measurements of the triple gauge couplings but these constraints are far weaker [39].

5.4 High energy behavior of amplitudes and violation of unitarity at tree-level

First let us look at the $\gamma\gamma \to \gamma\gamma$ process. We can find out the high energy behavior by dimensional analysis. The high energy behavior of the contribution from the local operators in Eq. (5.7) differs from the contribution from the non-local process, where

the $H\gamma\gamma$ vertex is derived from the operator $\mathcal{O}_0$, as follows,

$$\mathcal{O}_1^{\gamma\gamma}, \mathcal{O}_2^{\gamma\gamma} \quad : \quad \mathcal{A}(\gamma\gamma \to \gamma\gamma) \sim a_i \frac{\hat{s}^2}{\Lambda^4}$$

$$\mathcal{O}_0 \quad : \quad \mathcal{A}(\gamma\gamma \to H^* \to \gamma\gamma) \sim a_0 \frac{v\hat{s}}{\Lambda^2} \frac{1}{\hat{s}} \times a_0 \frac{v\hat{s}}{\Lambda^2} \sim a_0^2 \frac{v^2 \hat{s}}{\Lambda^4}$$

(5.24)

where $\hat{s}$ is the photon-photon center of mass energy squared. The local contribution is thus expected to dominate over the non-local contribution at high energies.

For the $\gamma\gamma \to ZZ$ process the operators in the light Higgs case in Eq. (5.7)can be divided into into two categories according to the final polarization of the Zs. At high energies the operators $\mathcal{O}_1^{ZZ}$, $\mathcal{O}_2^{ZZ}$ contribute mainly to the production of longitudinally polarized Z-bosons through the process $\gamma\gamma \to Z_L Z_L$ while the operators $\mathcal{O}_3^{ZZ} - \mathcal{O}_6^{ZZ}$ contribute mainly to transverse Z production through the process $\gamma\gamma \to Z_T Z_T$. This can be understood by using the goldstone boson equivalence theorem. The operators like $\mathcal{O}_3^{ZZ} - \mathcal{O}_6^{ZZ}$ do not arise from dimension 8 operators involving the Higgs field (see Eq. (5.8)) and so they do not introduce new couplings to the Goldstone bosons (that are eaten by the gauge bosons in the unitary gauge). New contributions to the process $\gamma\gamma \to Z_L Z_L$ they introduce are, therefore, suppressed.

Let us now see the energy dependance of the $\gamma\gamma \to ZZ$ amplitude of the dominant Z-polarization modes for the different operators using dimensional analysis in the

high energy limit,

$$\begin{aligned}
\mathcal{O}_3^{ZZ} - \mathcal{O}_6^{ZZ} \;:\; & \mathcal{A}(\gamma\gamma \to Z_T Z_T) \sim a_i \frac{\hat{s}^2}{\Lambda^4} \\
\mathcal{O}_1^{ZZ}, \mathcal{O}_2^{ZZ} \;:\; & \mathcal{A}(\gamma\gamma \to Z_L Z_L) \sim a_i \frac{m_Z^2 \hat{s}}{\Lambda^4} \frac{\hat{s}}{m_Z^2} \sim a_i \frac{\hat{s}^2}{\Lambda^4} \\
\mathcal{O}_0 \;:\; & \mathcal{A}(\gamma\gamma \to H^* \to Z_T Z_T) \sim a_0 \frac{v\hat{s}}{\Lambda^2} \frac{1}{\hat{s}} \frac{g m_Z}{c_w} \sim a_0 \frac{m_Z^2}{\Lambda^2} \\
\mathcal{O}_0 \;:\; & \mathcal{A}(\gamma\gamma \to H^* \to Z_L Z_L) \sim a_0 \frac{v\hat{s}}{\Lambda^2} \frac{1}{\hat{s}} \frac{g m_Z}{c_w} \frac{\hat{s}}{m_Z^2} \sim a_0 \frac{\hat{s}}{\Lambda^2}.
\end{aligned}$$

(5.25)

where the the $\hat{s}/m_Z^2$ factor for the longitudinal modes comes from the longitudinal polarization vectors and $g m_Z/c_w$ is the SM HZZ coupling. Note that according to Eq. (5.25) the $\gamma\gamma \to H^* \to ZZ$ process would mainly produce longitudinal Zs. As discussed earlier the contribution of the operator $\mathcal{O}_0$ can be subtracted by measuring the $H \to \gamma\gamma$ partial decay width. For the operators in the higgsless case in Section 5.2.2, the dominant mode will be $\gamma\gamma \to Z_L Z_L$ and the energy dependence would be,

$$(5.26) \qquad \mathcal{A}(\gamma\gamma \to Z_L Z_L) \sim (g/2c_w)^2 a_i^{hl} \frac{\hat{s}}{\Lambda^2} \frac{\hat{s}}{m_Z^2} \sim a_i^{hl} \frac{\hat{s}^2}{\Lambda^2 v^2}.$$

As all the amplitudes above grow with energy they would all violate partial wave unitarity for some value of $\hat{s}$. We obtain the perturbative unitarity bound for the processes in Appendix B. The condition that perturbative unitarity is not violated is,

$$(5.27) \qquad (\mathrm{Re}(b_l))^2 + \beta \sum_{\epsilon_3,\epsilon_4} |a_l|^2 + \delta_l < \frac{1}{4},$$

where a_l (b_l) is the l-th partial wave amplitude for the $\gamma\gamma \to ZZ(\gamma\gamma)$ process, $\beta = \sqrt{1 - \frac{4m_Z^2}{\hat{s}^2}}$, $\hat{s}$ is the photon-photon center of mass energy, δ_l is the positive contribution from other processes and ϵ_3 and ϵ_4 are the polarizations of the Z bosons
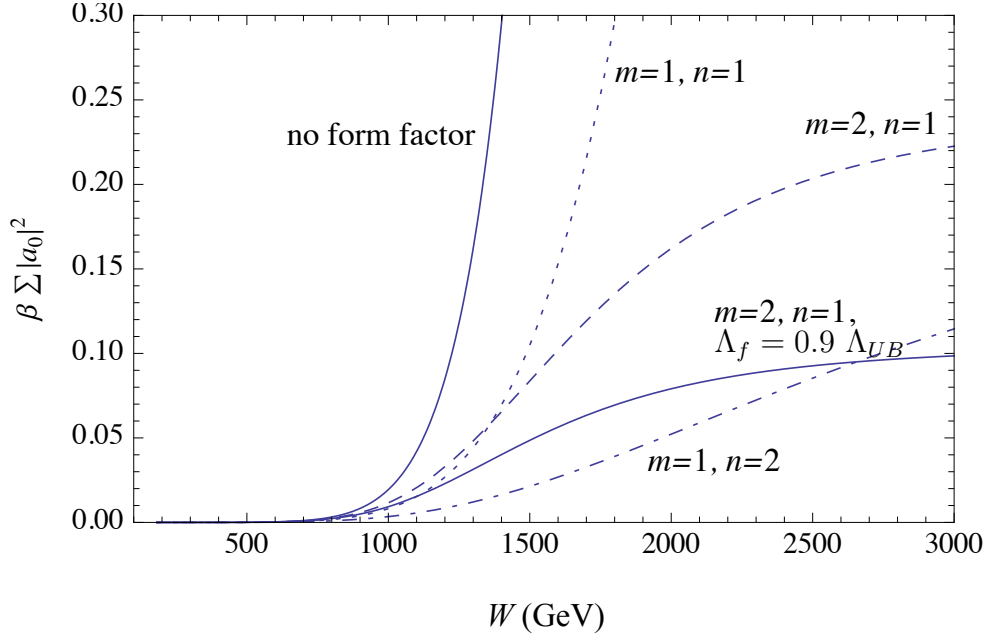
Figure 5.2: Here we plot $\left((\mathrm{Re}(b_l))^2 + \beta \sum_{\epsilon_3,\epsilon_4} |a_l|^2 \right)$ in Eq. (5.27) vs the photon-photon center of mass energy for $l = 0$ with and without the form factor in Eq. (5.28) taking $b_i/\Lambda^2 = 1$ TeV^{-2} and $c_i/\Lambda^4 = 1$ TeV^{-4}. We take $\Lambda_f^{\gamma\gamma/ZZ} = \Lambda_{UB}^{\gamma\gamma/ZZ}$ in the form factor for all the different cases other than the lower solid line where we take $\Lambda_f^{\gamma\gamma/ZZ} = 0.9\,\Lambda_{UB}^{\gamma\gamma/ZZ}$.

produced. For the first term the final polarizations are same as the initial. The initial polarizations of the photons must be chosen to maximize the LHS to get the most stringent possible bound. We find the most stringent bounds from the $l = 0$ mode.

To ameliorate the growth of the amplitude with energy we can use form factors as follows,

$$(5.28) \qquad \mathcal{A} \to \mathcal{A} \left(\frac{1}{1 + (\hat{s}/\Lambda_f^2)^m} \right)^n.$$

By Taylor expanding the modified amplitude we see that by introducing a form factor we effectively introduce higher order contributions, such as those expected from loop effects and higher dimensional operators, to cancel the tree-level growth of the amplitude. For example if $\mathcal{A} = k\hat{s}^2/\Lambda^4$ the for the choice $m = 2$ and $n = 1$

the modified amplitude is ,

$$(5.29) \qquad \frac{k\hat{s}^2/\Lambda^4}{1+(\hat{s}/\Lambda_f^2)^2} = (k\hat{s}^2/\Lambda^4)\left(1 - (\hat{s}/\Lambda_f^2)^2 + (\hat{s}/\Lambda_f^2)^4 - (\hat{s}/\Lambda_f^2)^6...\right).$$

In order that the Eq. (5.27) is obeyed we would require that,

$$(5.30) \qquad\qquad\qquad (\text{Re}(b_l))^2 < 0.1$$

$$(5.31) \qquad\qquad\qquad \beta \sum_{\epsilon_3,\epsilon_4} |a_l|^2 < 0.1.$$

The RHS in the two equations above do not add up to the RHS of Eq. (5.27) because we have made some allowance for other contributions to δ_l. To ensure that these conditions are obeyed we use form factors for both the $\gamma\gamma \to \gamma\gamma$ and the $\gamma\gamma \to ZZ$ amplitudes.

Fig. 5.2 shows the growth of $\left((\text{Re}(b_l))^2 + \beta\sum_{\epsilon_3,\epsilon_4}|a_l|^2\right)$ in Eq. (5.27) for $l = 0$ with energy, for different choices of the form factor parameters. We consider the light Higgs case in Section 5.2.1, taking the couplings $b_i/\Lambda^2 = 1$ TeV^{-2} and $c_i/\Lambda^4 = 1$ TeV^{-4}. Let $\Lambda_{UB}^{\gamma\gamma}$ and Λ_{UB}^{ZZ} be the values of $\hat{s}$ where the conditions in Eq. (5.30) and Eq. (5.31) are respectively violated when no form factor is applied. We can see that the amplitude keeps growing for $m = n = 1$ and $\Lambda_f^{\gamma\gamma/ZZ} = \Lambda_{UB}^{\gamma\gamma/ZZ}$, thus violating the perturbative unitarity bound. However, the amplitude is suppressed below the bound for $m = 1, n = 2$ and $m = 2, n = 1$ for the same values of $\Lambda_f^{\gamma\gamma/ZZ}$. We see that in the latter case the amplitude saturates the bounds in Eq. (5.30) and Eq. (5.31) at high energies. We also show a curve with $m = 2, n = 1$ but $\Lambda_f^{\gamma\gamma/ZZ} = 0.9 \, \Lambda_{UB}^{\gamma\gamma/ZZ}$ which coincides with the $\Lambda_f^{\gamma\gamma/ZZ} = \Lambda_{UB}^{\gamma\gamma/ZZ}$ curve at low energies but deviates from it for $\hat{s}$ close to Λ_{UB}^2. Unless otherwise mentioned from now on we will use form factors with $m = 2, n = 1$ and $\Lambda_f^{\gamma\gamma/ZZ} = \Lambda_{UB}^{\gamma\gamma/ZZ}$. While our final results will depend on this specific choice of form factor a different form factor would result in a cross-section with a different numerical value but the same order of magnitude. Thus there will be
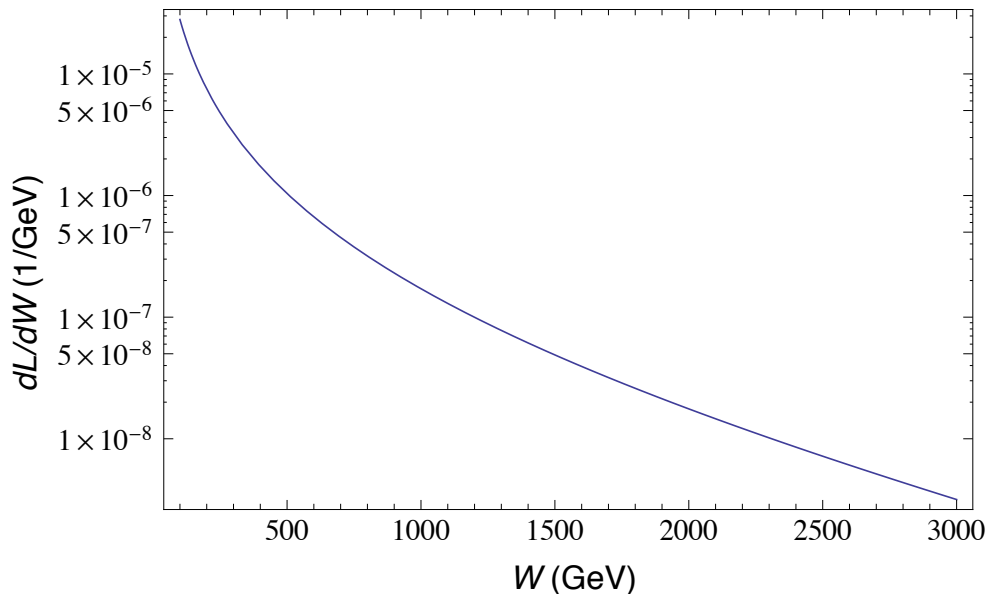
Figure 5.3: The Luminosity function dL/dW in Eq. (5.36) taking $q^2_{max} = 2$ GeV^2.

a relatively small difference in our final sensitivity results on Λ as the cross-section goes as $\sigma \sim \Lambda^{-8}$ ($\sigma \sim \Lambda^{-4}$) for the dimension 8 (dimension 6) operators in the light Higgs (higgsless) case.

5.5 The Equivalent Photon Approximation and the proton level cross-section for $pp(\gamma\gamma \to ZZ)pp$

Consider a general process $pp(\gamma\gamma \to X)pp$. To find the amplitude for this process we need to know the $pp\gamma$ vertex. From gauge invariance the most general form for this vertex is [113],

$$(5.32) \qquad -ie\left[F_1(q^2)\gamma^\mu + \frac{\mu_p - 1}{2m_p}F_2(q^2)i\sigma^{\mu\nu}q_\nu\right].$$

Here $e\mu_p/2m_p$ is the proton magnetic moment with $\mu_p^2 = 7.78$, q_i^2, the invariant mass of one of the photons is, as shown in Appendix C, always space-like in such a process and thus it is negative. The functions $F_1(q^2)$ and $F_2(q^2)$ in the vertex can be expressed in terms of the the empirically determined elastic electric and magnetic

form factors for the proton, $G_E(q^2)$ and $G_M(q^2)$ respectively, as follows,

$$F_1(q^2) = \frac{G_E + \tau G_M}{1 + \tau} \quad F_2(q^2) = \frac{G_M - G_E}{\kappa(1 + \tau)}$$

(5.33)
$$G_E = G_M/\mu_p = (1 - q^2/q_0^2)^{-2}.$$

Here $G_E(q^2)$ and $G_M(q^2)$ have been written in the dipole approximation with $q_0^2 = 0.71$ GeV^2 and $\tau = (-q^2)/4m_p^2$. By a change of variables the final phase space integration for the process $pp(\gamma\gamma \to X)pp$ can be done over $d(-q_1^2)d(-q_2^2)d\omega_1 d\omega_2$, instead of the usual variables [114], ω_i being the energy of the photons. The cross section thus obtained would receive most of the contribution from the region in phase space where the $|q_i^2|$ are small (this also corresponds to small scattreing angles for the proton) because of the $1/q_i^2$ factors from the photon propagator. Note that, there is a kinematic lower bound on $|q_i^2|$,

(5.34)
$$q_i^2 \lesssim -\frac{m^2\omega_i^2}{E(E - \omega_i)}$$

where E is the energy of the proton in the center of mass frame and m_p its mass (see Appendix C for the derivation).

The fact that most of the contribution to the cross section comes from the small $|q_i^2|$ region means that we can evaluate the contribution to the amplitude from the $\gamma\gamma \to X$ part of the diagram in the $|q_i^2| \to 0$ limit. This is the so-called Equivalent Photon Approximation (EPA). This amounts to treating the photons as real with only transverse polarizations while doing the the $\gamma\gamma \to X$ part of the calculation so that the total cross section can be written in the factorized form,

(5.35)
$$\sigma = S_{QED}^2 \int_{2m_Z}^{W_{max}} \frac{dL}{dW} \sigma_{\gamma\gamma} dW.$$

Here $W = \sqrt{\hat{s}}$ is the photon-photon center of mass energy and $\sigma_{\gamma\gamma}$ is the photon level cross section. S_{QED}^2, the survival probability for diffractive photon exchange

processes, is the probability that the proton remains intact and is not broken due to subsequent inelastic QCD interactions. We take $S^2_{QED} = 0.9$ following the theoretical calculation in Ref. [108]. The function dL/dW contains all the details of the proton electromagnetic form factors and also the integral over $1/q_i^2$ factors of the photon propagators. A detailed calculation of dL/dW using EPA leads to the following expressions (see Appendix D in Ref. [114]),

$$
\frac{dL}{dW} = \int_0^1 2W f(x) f\left(\frac{W^2}{xs}\right) \frac{dx}{xs}
$$

$$
f(x) = \frac{\alpha}{\pi} \frac{E}{\omega} \int_{q_{min}^2}^{q_{max}^2} \frac{d(-q^2)}{|q^2|} \left[\left(1 - \frac{\omega}{E}\right) \left(1 - \left|\frac{q_{min}^2}{q^2}\right|\right) D + \frac{\omega^2}{2E^2} C \right]
$$

$$
(5.36) \qquad C = G_M^2 \quad D = (4m_p^2 G_E^2 - q^2 G_M^2)/(4m_p^2 - q^2)
$$

Here $x = \frac{\omega}{E}$ and $s = 4E^2$. While the lower limit of the integration is set by kinematics (see Eq. (5.34)) we take the upper limit to be $q_{max}^2 = 2$ GeV. Beyond $q_{max}^2 = 2$ GeV, the form factors in Eq. (5.33) become very small so that the contribution to the integral is negligible.

To understand the physical meaning of dL/dW we can multiply both sides of Eq. (5.35) by $\mathcal{L}_p$, the proton luminosity. Then we find that the luminosity function is the ratio of the differential photon luminosity $d\mathcal{L}_\gamma/dW$ and the proton luminosity,

$$
(5.37) \qquad dL/dW = \frac{d\mathcal{L}_\gamma/dW}{\mathcal{L}_p}.
$$

Note that here L is unitless and $\mathcal{L}_{\gamma,p}$ has the usual units $m^{-2}s^{-1}$. We plot the photon luminosity function in Fig. 5.3. We find that,

$$
(5.38) \qquad S^2_{QED} \int_{2m_Z}^{2E} \frac{dL}{dW} dW \sim 1.3 \times 10^{-3}.
$$

For a particular process $\gamma\gamma \to X$ this number gives an upper bound on the ratio,

$$
\frac{\sigma_{\gamma\gamma}\,(pp(\gamma\gamma \to X)pp)}{\sigma(\gamma\gamma \to X)}
$$

Figure 5.4: The $pp(\gamma\gamma \to \gamma\gamma)pp$ cross section we obtain as a function of W_{max} with and without a form factor. For the form factor we use in Eq. (5.28) with $m = 2, n = 1$ and $\Lambda_f^{\gamma\gamma/ZZ} = \Lambda_{UB}^{\gamma\gamma/ZZ}$. We have taken $b_i/\Lambda^2 = 1$ TeV^{-2} and $c_i/\Lambda^4 = 1$ TeV^{-4} in Eq. (5.8), the Higgs mass $m_h = 120$ GeV and the proton-proton center of mass energy equal to 14 TeV.

if $\sigma_{\gamma\gamma}$ is a constant or decreasing function of W as is the case usually for SM processes. Thus from a knowledge of $\sigma_{\gamma\gamma}(\gamma\gamma \to X)$ one can estimate $\sigma\left(pp(\gamma\gamma \to X)pp\right)$ using Eq. (5.38)

5.6   Theoretical cross sections

In this section we present the cross section for $pp(\gamma\gamma \to \gamma\gamma)pp$ and $pp(\gamma\gamma \to ZZ)pp$ (see Fig. 5.1) with the proton-proton center of mass energy equal to 14 TeV. We will consider only the light higgs case in Section 5.2.1 taking all $b_i/\Lambda^2 = 1$ TeV^{-2} and all $c_i/\Lambda^4 = 1$ TeV^{-4} in Eqs. (5.9) and (5.2). With these values for the couplings and using Eq. (5.30) and (5.31) for $l = 0$, we get the unitarity bound $\Lambda_{UB}^{\gamma\gamma} = 1220$ GeV and $\Lambda_{UB}^{ZZ} = 1260$ GeV respectively.

We have evaluated the cross section with and without the form factor in Eq. (5.28).
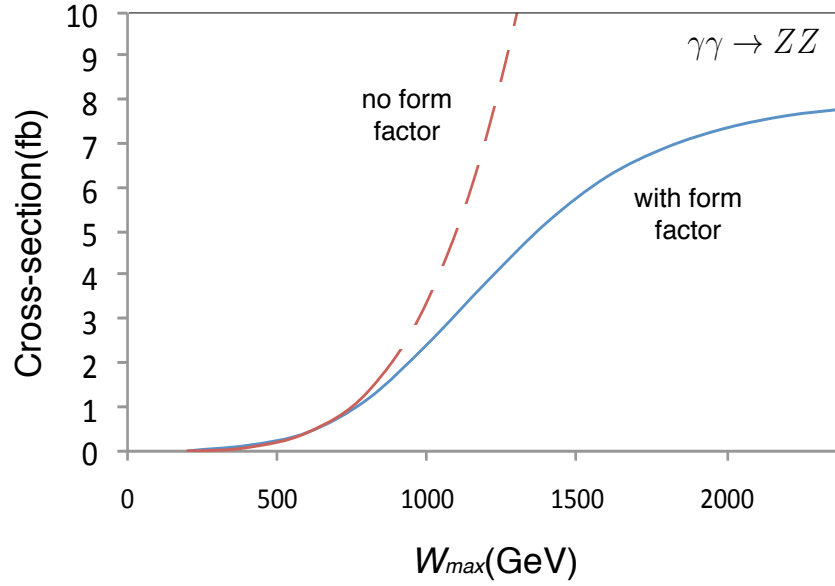
Figure 5.5: The $pp(\gamma\gamma \to ZZ)pp$ cross section we obtain as a function of W_{max} with and without a form factor. For the the form factor we use in Eq (5.28) with $m = 2, n = 1$ and $\Lambda_f^{\gamma\gamma/ZZ} = \Lambda_{UB}^{\gamma\gamma/ZZ}$. We have taken $b_i/\Lambda^2 = 1$ TeV^{-2} and $c_i/\Lambda^4 = 1$ TeV^{-4} in Eq. (5.8), the Higgs mass $m_h = 120$ GeV and the proton-proton center of mass energy equal to 14 TeV.

For the form factor we have taken $\Lambda_f^{\gamma\gamma/ZZ} = \Lambda_{UB}^{\gamma\gamma/ZZ}$, $m = 2$ and $n = 1$. We have taken the Higgs mass $m_h = 120$ GeV. We have evaluated the cross section with the cut $W < W_{max}$ and varied W_{max}. This cut is important as the ambiguities due to the choice of form factor become more important for large values of W_{max}. For the $pp(\gamma\gamma \to \gamma\gamma)pp$ process we show the results with and without the form factor in Fig. 5.4. We have checked that the contribution from the $\gamma\gamma \to H^* \to \gamma\gamma$ process due to the presence of the operator $\mathcal{O}_0$ is small compared to the total cross-section as is expected from the arguments in Section 5.4.

We show the results for the $pp(\gamma\gamma \to ZZ)pp$ process with and without the form factor in Fig. 5.5. In Fig. 5.6(left) we show the $\gamma\gamma \to ZZ$ cross section we obtain as a function of W_{max} without any form factor. We show separately in the same figure the contribution due to the operator $\mathcal{O}_0$ through the process $\gamma\gamma \to H^* \to$
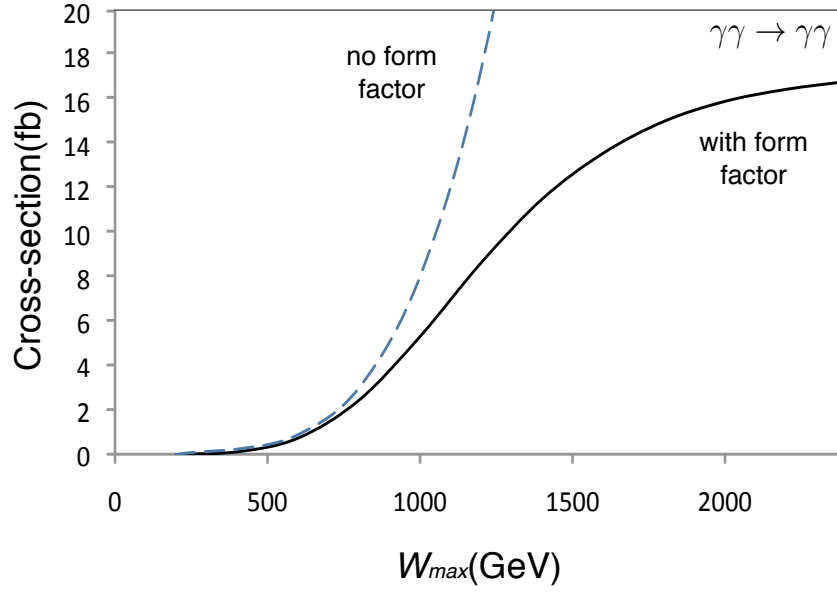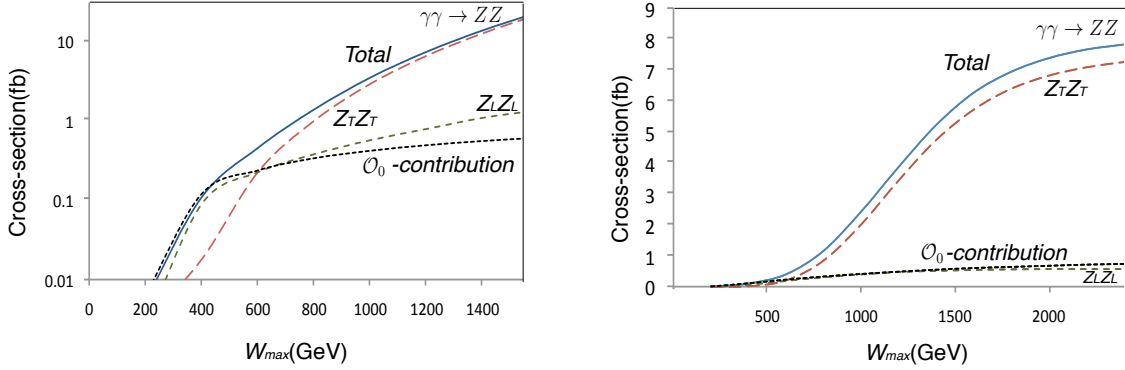
Figure 5.6: The $pp(\gamma\gamma \to ZZ)pp$ cross section we obtain as a function of W_{max} without any form factor. We have taken $b_i/\Lambda^2 = 1$ TeV^{-2} and $c_i/\Lambda^4 = 1$ TeV^{-4} in Eq. (5.8), the Higgs mass $m_h = 120$ GeV and the proton-proton center of mass energy equal to 14 TeV. We show the total cross section (solid), the $Z_T Z_T$ production cross section (big dashes), the $Z_L Z_L$ production cross section (small dashes) and the total cross section only due to the operator $\mathcal{O}_0$ (dotted) through the $\gamma\gamma \to h^* \to ZZ$ process.

ZZ. We see that the non-local contribution due to $\mathcal{O}_0$ dominates at low energies. The contribution to the cross section due to the other operators, however, grows more rapidly with $\hat{s}$ $\left(\text{as } \sigma_{\gamma\gamma} \sim \hat{s}^3\right)$ compared to the $\mathcal{O}_0$ contribution. At higher energies $\mathcal{O}_3^{ZZ}$ contributes most to the cross-section. As mentioned earlier the coupling a_0 can be accurately measured by measuring the $H \to \gamma\gamma$ partial width so any deviation would indicate the presence of higher dimensional operators. We also show in Fig. 5.6(left), the $\gamma\gamma \to Z_L Z_L$ and $\gamma\gamma \to Z_T Z_T$ contributions to the cross section. As explained before, for longitudinal Z production, the main contribution comes from the operators $\mathcal{O}_0, \mathcal{O}_{1,2}^{ZZ}$ with $\mathcal{O}_0$ contributing dominantly at low energies and $\mathcal{O}_1^{ZZ}$ contributing dominantly at higher energies. For transverse Z production only the operators $\mathcal{O}_0, \mathcal{O}_{3,4,5,6}^{ZZ}$ contribute significantly with the dominant contribution coming from $\mathcal{O}_3^{ZZ}$.

In Fig. 5.6(right) we have the signal cross section curves as in Fig. 5.6(right) but with form factors. The contribution due to $\mathcal{O}_0$ is shown without any form factor suppression. This is because we want to show the pure contribution of the operator

$\mathcal{O}_0$ so that any deviation can be interpreted as the presence of higher order effects in $\hat{s}/\Lambda^2$ (as explained in Section 5.4, using a form factor would amount to assuming such higher order corrections).

Finally let us state how the contributions of the different $\gamma\gamma ZZ$ operators in Eq. (5.7) can, in principle, be resolved. We have already seen how looking at the final polarization of the Zs can be used to distinguish the contribution of $\mathcal{O}_1^{ZZ}$ and $\mathcal{O}_2^{ZZ}$ from the other $\gamma\gamma ZZ$ operators. Another fact that can be used is that only for the operators $\mathcal{O}_1^{ZZ}$ and $\mathcal{O}_3^{ZZ}$ are the amplitudes spherically symmetric. Thus the $\gamma\gamma ZZ$ operators in Eq. (5.7) can be divided into four categories: those that contribute mainly to the $Z_L Z_L$ mode and give spherically symmetric amplitudes (only $\mathcal{O}_1^{ZZ}$), those that contribute mainly to the $Z_L Z_L$ mode but do not give spherically symmetric amplitudes (only $\mathcal{O}_2^{ZZ}$), those that contribute mainly to the $Z_T Z_T$ mode and give spherically symmetric amplitudes (only $\mathcal{O}_3^{ZZ}$), and those that contribute mainly to the $Z_T Z_T$ mode but do not give spherically symmetric amplitudes ($\mathcal{O}_4^{ZZ} - \mathcal{O}_6^{ZZ}$). Note that resolving the contributions of the different operators would require higher luminosity than just detecting the presence of QNGCs, but we will not go into the experimental feasibility of such studies.

5.7 LHC signal search strategy

As explained in Section 5.5 the final state protons in diffractive processes are scattered at small angles. To detect such protons very forward detectors have been proposed both for the ATLAS and CMS detectors (see Ref [99]). It has been proposed that such detectors should be placed at distances of 220 m and 420 m from the interaction point where the distance is along the circular beam line. To give an idea about these distances, at 220 m the beam line curves away from the tangential

direction at the interaction point by about 6 meters. The protons lose a small fraction of their energy in the diffractive process and experience a small deflection from the beam axis. As the deflection is very small, the LHC magnets continue to curve the protons along the beam pipe but they do move away form the beam axis and out of the beam envelope because of the deflection. Thus detectors close to the beam axis (a few millimeters away) would be able to detect the protons. It is also important to note that particles other than protons would never be detected in these detectors as they have a different cyclotron radius. Thus these detectors effectively use the LHC magnets as a spectrometer.

As the detectors need to be close to the beam axis radiation hardness is a requirement that the detector must fulfill. This along with resolution requirements makes 3D silicon detectors ideal as proton detectors. From the measurement of the position and track direction at the detectors the momentum four vector of the proton can be reconstructed by inverting the transport of the proton due to the LHC magnet optics. Thus it is possible to measure the fraction of energy lost by each proton, ξ_i and thus measure the invariant mass of the central system (also called the proton missing mass),

$$(5.39) \qquad\qquad W = \sqrt{\xi_1 \xi_2 s},$$

where $s = (14 \text{ TeV})^2$ for the 14 TeV LHC. The 220 m detectors detect protons with smaller deflection, and thus smaller ξ, than the 220 m detectors. As higher invariant masses would correspond to higher ξs, the 420 m detector is sensitive in the low mass region whereas the 220 m detector is sensitive in the high mass region. The 220 m detector is thus crucial for the kind of study we are doing in this work where most of the signal contribution comes from events with high W. Mass resolution between 2 GeV and 3 GeV for low energies and about 5-6 GeV for the highest photon energies

can be achieved by these detectors [115].

As only events with two intact protons are accepted, the only background processes can be those in which the proton emits a light particle with no electromagnetic or color charge and remains intact. Thus the proton can emit a photon or a pomeron. In pomeron fusion processes, also called 'Double Pomeron Exchange' (DPE) processes, the pomeron, in general, breaks into fragments. Thus whenever we would write down a process $pp(DPE \rightarrow X)pp$, X being a particular final state, it would be implicit that this is an inclusive process where other particles (pomeron fragments) are also present. These detectors can be used to test if an event is exclusive or inclusive, where by an exclusive event we mean an event where no other particle in addition to the final state particles is produced. This can be done by matching the invariant mass measured by the proton detectors (using Eq. (5.39)) with the invariant mass measured by the central detectors. Also, in exclusive events the p_T of all the final state particles excluding the protons (which carry very little p_T) must add up to nearly zero. Thus if only such exclusive events are accepted the underlying process can only be a an exclusive pomeron fusion process, usually called 'Central Exclusive Production' (CEP) and the inclusive DPE background can be reduced. Including both the 220 m and 420 m the acceptance range for ξ_i is [115],

$$0.0015 < \xi_i < 0.15 \tag{5.40}$$

Using Eq. (5.40) we see that only events with 21 GeV$< W < 2100$ GeV are accepted by the detector.

A potentially important background contribution is from overlap events. If the signal event is $pp \rightarrow pXp$, an overlap event would be defined as the coincidence of an event where the central system X is produced with one or more diffractive events in the same bunch crossing. Processes like $[p][Xp]$, where one of the protons

is produced in an interaction different from the central process (the square brackets grouping the final particles produced in the same scattering process) or processes like $[pp][X]$ and $[p][X][p]$ where both the protons are produced in an interaction different from the central system, can fake signal events. To reject such background events the forward detectors would be equipped with timing detectors which would have a resolution of the order of 10 ps [99] (note that the LHC bunch length is about 250 ps at 1-sigma). These detectors would be able to reconstruct the vertex position of the two protons assuming they are produced at the same interaction point. This vertex would not match the vertex for the central system, X, for the fake events and thus such background events can be rejected. Another way to reduce the overlap background is by matching the net invariant mass of the central system measured by the central detectors with the values obtained by the forward detectors. We have already discussed how this can be done in the context of testing whether an event is exclusive or not. Overlap backgrounds are of great importance when the inelastic production cross-section for the central system X is large as is the case for the dijet background to diffractive $H \rightarrow bb$ production [116](where the jets are misidentified as b-jets) but is of much lesser importance in our case. Let us now discuss the search strategy for the $pp(\gamma\gamma \rightarrow ZZ)pp$ and the $pp(\gamma\gamma \rightarrow \gamma\gamma)pp$ processes.

5.7.1 $pp(\gamma\gamma \rightarrow ZZ)pp$ process

As we do not perform a detailed detector simulation and wish to make only an estimate of the detector level cross-section, we will look at the $p + (ZZ \rightarrow 4l) + p$ final state ($l = e, \mu$) that is most free from experimental complications. Other final states involving hadronic Z decay modes may well turn out to be more sensitive to our observable but ascertaining this would require a more rigorous experimental analysis.

The most important background process is $pp(DPE \rightarrow ZZ)pp$ in the SM. As mentioned before this is an inclusive process where the final state has pomeron remnants in addition to the Z pair. The DPE background has been computed using the Forward Physics Monte Carlo (FPMC) [117] which uses the Ingelman-Schlein (IS) model [118] for inclusive diffraction. In this model the cross-section of a process like $pp(DPE \rightarrow X)pp$ is computed by convoluting the cross-section of the partonic hard process $ij \rightarrow X$ (i, j being the partons) with diffractive parton density functions (DPDF) measured at HERA. The DPDF describes the probability of extracting a certain parton with a given longitudinal momentum fraction from the proton. The DPDF itself can be expressed as a product of the pomeron flux, measured in other diffractive processes, and the probability of extraction of the parton from the pomeron which breaks into fragments. Whereas the IS model describes diffractive data at the Hadron-Electron Ring Accelerator (HERA) very well its theory prediction for diffractive dijet production at the Tevatron is larger by a factor of 10 [119]. This is usually attributed to the fact that there is some probability for the protons in a DPE process to have a subsequent inelastic interaction which breaks the proton. Thus the cross-section computed in this model must finally be multiplied by the survival probability, S^2_{DPE}, which is the probability that there is no further inelastic interaction between the protons. The maximum value of the survival probability reported in the literature is about $S^2_{DPE} = 0.06$ [120].

For the $pp(DPE \rightarrow ZZ)pp$ process that we are interested in, there are two possible partonic sub-processes, the $qq \rightarrow ZZ$ sub-process via t-channel quark exchange of a quark q and the $gg \rightarrow ZZ$ sub-process that is induced by fermion loops[4]. The quark component of the DPDF gives the dominant contribution in processes involving

---

[4]For the computaion of the partonic cross-section of the $gg \rightarrow ZZ$ sub-process, the $gg \rightarrow H^* \rightarrow ZZ$ process has not been included. This contribution is known to interfere negatively and decrease the total cross-section [121] so the background cross-section would have been lower had this contribution been incorporated.

diffractive vector boson production like the one we are interested in [122]. We apply the following cuts to the signal and background [115],

$$0.0015 < \xi_i < 0.15 \tag{5.41}$$

$$W > 300 \text{ GeV}. \tag{5.42}$$

The first cut above is just the ξ-acceptance cut for the forward detectors, and the second cut has been applied mainly to suppress the SM loop background discussed later. As explained in Section 5.6, most of the contribution to the signal cross-section comes from high energies so that the second cut hardly affects the signal. With these cuts the cross-section we thus obtain for $pp(DPE \to ZZ)pp$ from FPMC including all Z decay modes is 1.4 fb. Applying the above cut the signal cross-section (with form factor) is reduced from 8 fb to 3 fb in the light Higgs case for $b_i/\Lambda^2 = 1 \text{ TeV}^{-2}$ and $c_i/\Lambda^2 = 1 \text{ TeV}^{-4}$, where the ξ-acceptance cut is responsible for most of the reduction.

As the DPE background discussed above is inclusive unlike the signal it can be further reduced by testing if the events are exclusive. This can be done by matching the four-lepton invariant mass measured by the central detector with the invariant mass measured using Eq. (5.39). Also the net p_T of the four leptons must add up to nearly zero (as the protons carry hardly any transverse momentum) for exclusive events.

Now let us consider the background contribution from the SM loop process $pp(\gamma\gamma \to ZZ)pp$. The cross section $\sigma_{\gamma\gamma}(\gamma\gamma \to ZZ)$ has been evaluated in Ref. [123] to be roughly constant, around 300 fb in the range 300 GeV $< \tau <$ 2100 GeV, where the upper limit is equal to the upper limit obtained by applying the ξ-acceptance cut in

Eq. (5.46). Thus we find for the proton level cross section,

$$(5.43) \qquad \sigma \; = \; S_{QED}^2 \int_{2m_Z}^{2100} \frac{dL}{d\tau} \sigma_{\gamma\gamma} d\tau \approx 0.9 \times 300 \int_{2m_Z}^{2100} \frac{dL}{d\tau} d\tau \approx 0.1 \text{ fb,}$$

where we have imposed the cut $0.0015 < \xi_i < 0.15$. We find therefore that this background is negligible compared to the signal.

So far in all the instances where we have considered signal or background cross-sections we have not taken into account the branching ratio of the Z to leptons and detector efficiencies. Taking the lepton identification rate to be 90% [49] and the proton detection efficiency in the forward detectors to be 85% [99] we obtain for the effective cross-section we expect the detectors to measure,

$$(5.44) \qquad\qquad\qquad \sigma_{eff} = 0.56 \; B(Z \to ll)^2 \sigma_{th},$$

where σ_{th} is the theoretical cross-section including all Z decay modes.

Finally, let us mention a possible complication that may arise because of the fact that the high energy Zs we are considering would be boosted in the lab frame. This would cause the leptons to be collimated along the direction of motion of the parent Z. This may give rise to complications in detection of some electron pairs for which the two electrons are not well separated from each other (there is no such issue with muonic decays as muon separation is always efficient for the energies we are considering). We will not try to estimate this effect (see for example for a [124] more detailed discussion) but in our estimates of sensitivity in the next section, to give a conservative estimate, we will provide results considering only muonic decay of the Zs in addition to results considering decay of the Zs into both electrons and muons.

5.7.2 $pp(\gamma\gamma \to \gamma\gamma)pp$ **process**

For the $pp(\gamma\gamma \to \gamma\gamma)pp$ process we require the presence of two photons and two protons in the final state. Again the main background is from the $pp(DPE \to \gamma\gamma)pp$

process. The $pp(DPE \to \gamma\gamma)pp$ cross-section can be estimated from the $pp(DPE \to$

$ZZ)pp$ cross-section by using the fact that the t-channel quark exchange sub-process

$qq \to ZZ/\gamma\gamma$ is the dominant partonic sub-process [122]. As the diagrams for this

partonic sub-processes in both the cases are the same except for the two outgoing

vertices and external legs in the limit of massless quarks we get,

$$(5.45) \quad \frac{\sigma(pp(DPE \to \gamma\gamma)pp)}{\sigma(pp(DPE \to ZZ)pp)} = (1 - 4m_Z^2/\hat{s})^{-1/2} \frac{e^4}{(g/2c_w)^4} \left[\frac{\sum_{u,d,s} Q^4}{\sum_{u,d,s}(v_q^2 + a_q^2)^2} \right]$$

where v_q and a_q are the vector-like and axial vector-like couplings of the quarks to

the Z boson and Q is their electric charge. The sum is over the three light quarks

for which the probability of diffractive extraction from the proton is significant and

we assume that the diffractive PDFs for three light quarks are equal. The kinematic

factor on the RHS, which is almost unity at high energies, arises because the Z-boson

unlike the photon is massive. Taking $v_{d,s} = -0.35$, $v_u = 0.20$, $a_u = 1/2$, $a_d = -1/2$

and $\hat{s} = (500 \text{ GeV})^2$, we find this ratio to be 0.3. We apply the same cuts as in the

case of the $pp(\gamma\gamma \to ZZ)pp$ process, that is,

$$(5.46) \quad\quad\quad\quad\quad\quad 0.0015 < \xi_i < 0.15$$

$$(5.47) \quad\quad\quad\quad\quad\quad W > 300 \text{ GeV}$$

and using the above ratio we obtain this background cross-section to be 0.4 fb.

Again this inclusive DPE background can be further reduced by requiring the two

photon invariant mass to match the missing mass evaluated using Eq. (5.39) and by

demanding that $p_{T\gamma 1} = -p_{T\gamma 2}$ within experimental resolution.

The SM loop induced $pp(\gamma\gamma \to \gamma\gamma)$ process in this case has a cross-section that is

$\mathcal{O}(0.01)$ fb and can be ignored [125, 126]. An experimental background contribution

can come from mis-identification of jets as photons in the $pp(\gamma\gamma \to jj)pp$ process.

The total inclusive diffractive dijet cross-section at the LHC has been computed by

the diffractive Monte Carlo generator DPEMC [127] to be 4×10^7 fb [128] in the IS model with the cut $E_T > 25$ GeV for the jets. Taking the rejection factor of jets for photon identification to be 5000 [49] we get a background cross section of about 2 fb which is already smaller than the signal cross-section (with form factor) of 17 fb in the light higgs case for $b_i/\Lambda^2 = 1$ TeV^{-2} and $c_i/\Lambda^4 = 1$ TeV^{-4}. Further cuts like the W-cut in Eq. (5.47) and requiring $p_{T\gamma 1} = -p_{T\gamma 2}$ within experimental accuracy should completely remove this background.

The effective detector level cross-section is again smaller than the values mentioned so far. Taking the photon identification rate to be 90% [49] and proton detection efficiency in the forward detector to be 85% [99] we get,

$$(5.48) \qquad\qquad\qquad \sigma_{eff} = 0.69 \ \sigma_{th}$$

Note that for both the $pp(\gamma\gamma \rightarrow \gamma\gamma)pp$ and $pp(\gamma\gamma \rightarrow \gamma\gamma)ZZ$ processes we have ignored above the effects of the basic detector acceptance cuts $p_T > 10$ GeV and $\eta < 2.5$ for the leptons and photons. As the dominant contribution to the signal cross-section is central and from high energies, these cuts are expected to have a very small effect.

5.8 LHC sensitivity to QNGCs

Using the LHC search strategy for $pp(\gamma\gamma \rightarrow \gamma\gamma)pp$ and $pp(\gamma\gamma \rightarrow \gamma\gamma)ZZ$ signals outlined in the previous section we can now report the expected sensitivity of diffractive photon fusion at LHC to QNGCs. Table 5.1 shows the expected number of observed events N_{obs} and the signal significance for both the processes with different integrated luminosities. The expected number of signal, background and observed

Couplings	Process	Integrated Luminosity(fb^{-1})	N_{obs}	N_b	Confidence Level(sigma)
Case 1: $(850 \text{ GeV})^{-4}$	$\gamma\gamma \to \gamma\gamma$	1	12.1	0.3	>10
Case 1: $(1.8 \text{ TeV})^{-4}$	$\gamma\gamma \to \gamma\gamma$	300	133.1	82.8	5.2
Case 1: $(850 \text{ GeV})^{-4}$	$\gamma\gamma \to ZZ$	300	7.4(1.9)	1.1(0.3)	4.3(2.1)
Case 1: $(750 \text{ GeV})^{-4}$	$\gamma\gamma \to ZZ$	300	11.4(2.8)	1.1(0.3)	6.0(2.9)
Case 1:$(500 \text{ GeV})^{-4}$	$\gamma\gamma \to ZZ$	300	46.8(11.7)	1.1(0.3)	>10(8.1)
Case 2:$(700 \text{ GeV})^{-4}$	$\gamma\gamma \to ZZ$	300	14.8(3.7)	2.1(0.5)	5.8(3.1)
Case 2:$(500 \text{ GeV})^{-4}$	$\gamma\gamma \to ZZ$	300	51.3(12.8)	2.1(0.5)	8.2(7.7)
Case 3: $\Lambda_T = 1.0 \text{ TeV}$	$\gamma\gamma \to \gamma\gamma$	1	13.5	0.3	>10
Case 3: $\Lambda_T = 2.4 \text{ TeV}$	$\gamma\gamma \to \gamma\gamma$	300	118.2	82.8	3.9
Case 3: $\Lambda_T = 900 \text{ GeV}$	$\gamma\gamma \to ZZ$	300	12.6(3.2)	1.1(0.3)	6.4(3.6)
Case 3: $\Lambda_T = 700 \text{ GeV}$	$\gamma\gamma \to ZZ$	300	39.6(9.9)	1.1(0.3)	>10(7.1)
Case 4:$(1.9 \text{ TeV})^{-2}$	$\gamma\gamma \to ZZ$	300	5.3(1.3)	1.1(0.3)	3.3(2.1)
Case 4:$(2.2 \text{ TeV})^{-2}$	$\gamma\gamma \to ZZ$	300	3.9(1.0)	1.1(0.3)	2.2(1.1)

Table 5.1: The expected number of observed events N_{obs} and the signal significance for both the processes for different integrated luminosities. The expected number of observed events is evaluated using $N_{obs} = \sigma_{eff}^{signal} L$ where L is the integrated luminosity, and to evaluate the signal significance the background is assumed to follow a Poisson distribution with mean $N_b = \sigma_{eff}^{bgr} L$. The signal contribution has been evaluated with a form factor as in Eq. (5.28) taking $m = 2$, $n = 1$ and $\Lambda_f^{\gamma\gamma/ZZ} = \Lambda_{UB}^{\gamma\gamma/ZZ}$. For the $\gamma\gamma \to ZZ$ process the values in the parentheses show the results if only muonic decays of Z are considered.

events are evaluated using,

$$N_S = \sigma_{eff}^{signal} \mathcal{L}_{int}$$

$$N_B = \sigma_{eff}^{bgr} \mathcal{L}_{int}$$

(5.49) $$N_{obs} = N_S + N_B$$

where $\mathcal{L}_{int}$ is the integrated luminosity and σ_{eff} is the effective cross-section defined by Eq. (5.44) and Eq. (5.48), after taking into account detector efficiencies. The signal contribution has been evaluated with a form factor as in Eq. (5.28) taking $m = 2$, $n = 1$ and $\Lambda_f^{\gamma\gamma/ZZ} = \Lambda_{UB}^{\gamma\gamma/ZZ}$. We can simply add the signal and background events to get the total number of events expected to be observed in Eq. (5.49) because the interference with the background is very small. The interference with the DPE background is small because the interference between DPE and photon exchange diffractive processes is in general small and the interference with the SM

loop background is small because unlike the signal this background gets most of the contribution from the low-W region. In order to quantify the signal significance we evaluate the probability, α, that the background has not fluctuated to give a number of events greater than or equal to N_{obs} assuming that it follows a Poisson distribution with N_b as its mean. The confidence level expressed as a particular number of sigma deviations is given by $\sqrt{2}\ \mathrm{erf}^{-1}(\alpha)$ where erf() is the error function. We find the sensitivity for four different physically interesting ways of choosing the relative value of the QNGCs.

CASE I: $b_i/\Lambda^2 = 1/\Lambda^2$, $c_i/\Lambda^4 = 1/\Lambda^4$

We find that the $\gamma\gamma$ production process is by far the more promising of the two processes for probing QNGCs. As we can see from Table 5.1 even with integrated luminosities as low as $\mathcal{L}_{int} = 1$ fb^{-1},couplings as small as $1/(850$ GeV$)^4$ can be probed with large significance. With high integrated luminosity (300 fb^{-1}) couplings as small as $1/(1.8$ TeV$)^4$ can be detected with more than 5 sigma significance. There are possible cuts that can remove inclusive events as discussed in the previous section, which may substantially reduce the DPE background. If this is possible the $\gamma\gamma \rightarrow \gamma\gamma$ process can be sensitive to even smaller couplings. Note that a coupling with value $1/(1.8$ TeV$)^4$ does not necessarily mean that the energy scale of new physics is 1.8 TeV. If dimensionless couplings less than unity or loop factors are present, for instance, the scale of new physics would be lower.

The ZZ production process requires very high integrated luminosity. For this process we give in addition to the results assuming Z decays to both electrons and muons, the results considering only the muonic decays in parentheses. For $\mathcal{L}_{int} = 300$

fb^{-1} as one can see from Table 5.1 the smallest couplings that can be detected with more than 95 % confidence level are about $1/(850 \text{ GeV})^4$. If we require the detection of at least 10 signal events these values are $1/(750 \text{ GeV})^4$ and $1/(500 \text{ GeV})^4$ considering respectively decays to both electrons and muons and only muonic decays.

CASE 2: Resolving contribution to ZZ production from the contribution due to $\mathcal{O}_0$

As mentioned before the dimension-6 operator $\mathcal{O}_0$ contributes to the signal through the $\gamma\gamma \to H^* \to ZZ$ process. The value of this coupling can be obtained from the $H \to \gamma\gamma$ partial width measurement. For this case we consider this contribution to be part of the background and take all the $b_i/\Lambda^2 = 1/(850 \text{ GeV})^4$and all the c_i equal. We then try to find the smallest QNGC couplings c_i that can be detected. As we want to separate the $\mathcal{O}_0$ contribution from higher dimensional contributions, we do not use any form factor for the evaluation of the $\gamma\gamma \to H^* \to ZZ$ cross-section due to this operator as using the form factor is equivalent to including higher dimensional corrections (see Section 5.4). We find that the smallest couplings that can be detected for this case with 300 fb^{-1} data to be $1/(700 \text{ GeV})^4$ $(1/(500 \text{ GeV})^4)$ considering Z-decays to both electrons and muons (to only muons).

CASE 3: Graviton exchange in extra-dimensional model

For this case we assume that the QNGCs arise from the effective dimension-8 operator due to virtual graviton exchange in extra-dimensional theories described in Section 5.2.3. The relative couplings of the QNGCs are thus fixed by expanding the operator in Eq. (5.16) and the only adjustable parameter is Λ_T.

As one can see from Table 5.1 we find that the $\gamma\gamma \to \gamma\gamma$ process can detect this operator with only 1 fb^{-1} data for $\Lambda_T = 1.0$ TeV. For high luminosities (300 fb^{-1}) the maximum value of Λ_T that can be probed by this process in the DPE background is about $\Lambda_T = 2.4$ TeV. Note that our results differ from and are less optimistic than the results of Sahin et al [126] who do not consider the DPE background and more importantly use a far less restrictive ξ-acceptance cut. As explained after Eq. (5.40) because of the $\xi < 0.15$ acceptance cut only events with $W < 2.1$ TeV are accepted. In Ref. [126], on the other hand, events with ξ as high as 0.5 are accepted which corresponds to W as high as 7 TeV and most of the contribution to their signal comes from the high ξ events; protons with $\xi > 0.15$ can, however, not be detected by the forward detectors [115]. For the $\gamma\gamma \to ZZ$ process Λ_T as high as 900 GeV (700 GeV) can be probed with 300 fb^{-1} data considering Z-decays to both electrons and muons (to only muons). As already mentioned in Section 5.2.3 the $gg\gamma\gamma/ggZZ$ operators (g being a gluon) that arise from expanding the operator in Eq. (5.16) are expected to give a contribution to the exclusive $pp\gamma\gamma/ppZZ$ final states via central exclusive pomeron fusion but this contribution is expected to be negligible relative to the diffractive photon fusion contribution.

Establishing the presence of QNGCs would give very important complementary evidence for virtual graviton exchange because it is possible in this case to uniquely trace back to the underlying dimension 8 operator involved. Our final sensitivity results show, however, that for the particular diffractive processes we have studied for probing QNGCs the largest Λ_T that can possibly be probed (2.4 TeV) has already been ruled out by dijet constraints from the 36 pb^{-1} CMS data in Ref. [110] where the constraint $\Lambda_T > 3.8$ TeV has been derived. Thus diffractive photon fusion will not be able to probe Λ_T values still allowed by experimental data.

CASE 4: Higgsless case

As we discussed in Section 5.2.2 in the higgsless case we expect only the following two operators to be important,

$$(5.50) \qquad \mathcal{L}_{QNGC}^{Higgsless} = \frac{(g/2c_w)^2 a_1^{hl}}{\Lambda^2} F_{\mu\nu} F^{\mu\nu} Z_\rho Z^\rho + \frac{(g/2c_w)^2 a_2^{hl}}{\Lambda^2} F_{\mu\nu} F^{\mu\rho} Z_\rho Z^\nu.$$

We take $a_1^{hl} = a_2^{hl}$ in Eq. (5.15) and find that the $pp(\gamma\gamma \to ZZ)pp$ process is sensitive up to couplings as small as $1/(1.9\ \text{TeV})^2$ if we require more than 95% confidence level, a huge improvement over existing limits. Our sensitivity estimates agree well with those obtained by Chapon et al. in Ref. [103], once we translate to their convention for parametrization of these couplings.

Higgsless models are usually associated with strong electroweak symmetry breaking (EWSB) scenarios. The operator coefficients in such theories can be estimated by Naive Dimensional Analysis (NDA) (see Refs [129,130]). In our case, using NDA, we find $a_i^{hl}/\Lambda^2 = e^2/(16\pi^2\Lambda_s^2)$, Λ_s being the scale of the strongly coupled sector.[5] The above mentioned estimates tell us that our process is sensitive to $\Lambda_s < 100$ GeV. As a strong sector at such low energies is already ruled out by experiments, our process, unfortunately, cannot probe realistic scales for strong EWSB.

5.9 Conclusions

We have listed all possible operators contributing, at the lowest order, to Quartic Neutral Gauge Couplings, quartic gauge couplings involving only the photon and the Z boson and have studied the sensitivity of measurement of these couplings in diffractive photon fusion processes at the LHC. These couplings are interesting

---

[5]Note that the $ZZZZ$ coupling which appears at the dimension 4 level in the chiral lagrangian, from operators like $c\ (\text{Tr}[(D_\mu\Sigma)^\dagger D^\mu\Sigma])^2$, is less suppressed ($c \sim v^2/\Lambda_s^2 \approx 1/(16\pi^2)$) than other QNGCs.

because the lowest order contribution they receive is from dimension 8 operators in scenarios with a light Higgs and, in higgsless scenarios, from dimension 6 operators (with the exception of the $ZZZZ$ coupling which receives dimension 4 contributions in this scenario but we have not focussed on this coupling in this work in any case). Thus new physics processes which do not contribute through operators of the lowest possible dimension can be probed by measuring these couplings. One specific example that we have considered is virtual graviton exchange in extra dimensional theories where the lowest dimension operators generated are of dimension 8, and these include operators contributing to QNGCs.

Thus measurement of QNGCs in any experimental process would be interesting, but in this work we have studied their measurement in diffractive photon fusion processes like $pp(\gamma\gamma \to \gamma\gamma)pp$ and $pp(\gamma\gamma \to ZZ)pp$. The protons in these processes remain intact and scatter diffractively with very small scattering angles. These can be detected by very forward proton detectors that have been proposed for both the ATLAS and CMS experiments. As we argue the detection of the two γ/Zs in the central detectors along with the detection of the protons in these forward detectors would indicate the existence of QNGCs like the $\gamma\gamma\gamma\gamma$ and $\gamma\gamma ZZ$ couplings, as this is the only feasible new physics possibility that can lead to such a final state. The only other possibility is $pp(CEP \to ZZ)pp$, where CEP stands for Central Exclusive Production, is a process that takes place when pomerons fuse exclusively (that is without breaking into fragments) to give the $ZZ/\gamma\gamma$ final state. Such processes are, however, expected to have a much smaller cross-section when compared to photon fusion processes. To calculate the cross-section for the $pp(\gamma\gamma \to \gamma\gamma)pp$ and $pp(\gamma\gamma \to ZZ)pp$ processes we convolute the cross-section of the $\gamma\gamma \to \gamma\gamma/ZZ$ sub-process with the $\gamma\gamma$ luminosity function obtained using the Equivalent Photon Approximation.

The amplitude of the $\gamma\gamma \to \gamma\gamma/ZZ$ sub-process grows with energy because of the non-renormalizable couplings involved and we unitarize this using appropriate form factors. We have argued that our final sensitivity results for Λ will not change much for a different choice of form factor than ours.

Before we summarize our results on the sensitivities, note that QNGCs are very weakly constrained by existing data. Whereas no constraints exist on $\gamma\gamma\gamma\gamma$ couplings, the $\gamma\gamma ZZ$ couplings are constrained by direct search results from LEP to be smaller than about $1/(100 \ \text{GeV})^4$ ($1/(50 \ \text{GeV})^2$) and by precision measurements to be smaller than about $1/(270 \ \text{GeV})^4$ ($1/(420 \ \text{GeV})^2$) in the light Higgs (higgsless) case. We have found in this study that diffractive photon fusion at LHC can improve these sensitivities by many orders of magnitude for the $\gamma\gamma ZZ$ coupling, and can probe couplings as small as $1/(850 \ \text{GeV})^4$ ($1/(1.9 \ \text{TeV})^2$) with 300 fb^{-1} integrated luminosity for the light Higgs case (higgsless case). We find, however, using an NDA estimate, that the values in the higgsless case correspond to a scale lower than 100 GeV for the strong sector which is already excluded by experiments. The $\gamma\gamma\gamma\gamma$ coupling can be probed even more sensitively and values as small as $1/(1.8 \ \text{TeV})^4$ can be measured with the same integrated luminosity for the light Higgs case. For the specific case of virtual graviton exchange in theories with large extra dimensions we find that the highest scale that can be possibly probed (about $\Lambda_T = 2.4$ TeV by the $pp(\gamma\gamma \to \gamma\gamma)pp$ process with 300 fb^{-1} data) has, unfortunately, already been ruled out by the latest constraint from CMS dijet data which puts the bound $\Lambda_T > 3.8$ TeV.

APPENDICES

APPENDIX A

Transverse length of wave-packets forming a classicalon

We want to show in this Appendix that the wave-packets forming a classicalon have a transverse length equal to $\sqrt{N}r_*$, where N is the number of incoming wave-packets. We will show, first of all, that when all the incoming wave-packets reach the origin at $t = 0$ (see Fig. 2.2(right)), as described in Section 2.2.1, the field ϕ goes as $\phi \sim 1/r$ outside the classicalon radius r_*. To prove this, let us think for the moment, although as we will soon see this cannot be the case, that the wave-packets are infinitely extended in the transverse direction. If the number of these wave-packets is very large we can approximate the summation in the superposition of these wave-packets by an integral over a spherically symmetric distribution of these wave-packets with the direction of the momenta $\vec{k}$ varying continuously. Let θ be the angle the momentum of a particular wave-packet makes with the x-axis (see Fig. A.1). For a point P on the x-axis outside the sphere, at a distance r from the origin, only wave-packets with direction of momentum in a certain θ range, $-\cos^{-1}(r_*/r) < \theta < \cos^{-1}(r_*/r)$, contribute to the field ϕ (see Fig. A.1) if $r > r_*$. On the other hand, for a point inside the classicalon, there are contributions from all the wave-packets without a restriction on θ. The total contribution to the field ϕ at P, at a distance r from the origin, from wave-packets with energy $|\vec{k}|$ is,

$$\phi(r) \sim \int_{-\pi}^{\pi} \sin k(r\cos\theta + r_*)d\theta \text{ for } r < r_*,$$

(A.1) $\qquad \phi(r) \sim \int_{-\cos^{-1}(r_*/r)}^{\cos^{-1}(r_*/r)} \sin k(r\cos\theta + r_*)d\theta \sim \frac{1}{r} \text{ for } r \gg r_*,$

where we have used the functional form in Eq. (2.7) and substituted $l = r\cos\theta$. The exact form of the function inside the radius r_* is not important as it would change anyway in the presence of a classicalizing interaction. What is important is the $\phi \sim 1/r$ drop off outside the radius r_* which shows that most of the the energy does get localized inside r_* for these wave-packets (note that the energy density goes as $(\partial\phi)^2 \sim 1/r^4$). We can also obtain the normalization Q of the field, in $\phi \sim Q/r$, at the parametric level. For this note that our wavepackets must have the usual normalization $1/\sqrt{\omega V} \sim 1/\sqrt{\omega N r_*^3}$. Keeping in mind that the number of wave-packets giving a contribution in Eq. (A.1) in the interval between (θ, ϕ) and $(\theta + d\theta, \phi + d\phi)$ is $(N/4\pi)d\theta d\phi$ we get,

(A.2) $\qquad \phi(r) = \frac{N}{4\pi} \frac{1}{\sqrt{\omega N r_*^3}} \int_{-\cos^{-1}(r_*/r)}^{\cos^{-1}(r_*/r)} \sin k(r\cos\theta + r_*)d\theta \sim \frac{\sqrt{N}}{r} \text{ for } r \gg r_*.$

where we have used the typical value, $\omega = k = 1/r_*$. The numerator $\sqrt{N} = \sqrt{M r_*}$ is actually the correct charge in any classicalizing theory [18]. For instance in the special case of black holes it correctly reduces to the mass M of the black hole.

As we argued in Section 2.2.1, in order that they always overlap, our wave-packets must have a finite transverse length. Let us calculate this length for N incoming/outgoing particles. For N particles at a radius $L/2$ from the origin, each particle can be thought to occupy an area $\pi L^2/N$ where no other particle is present. Assuming this area occupied by the particle to be circular we find that on an average the angle between the momenta of two neighboring particles would be
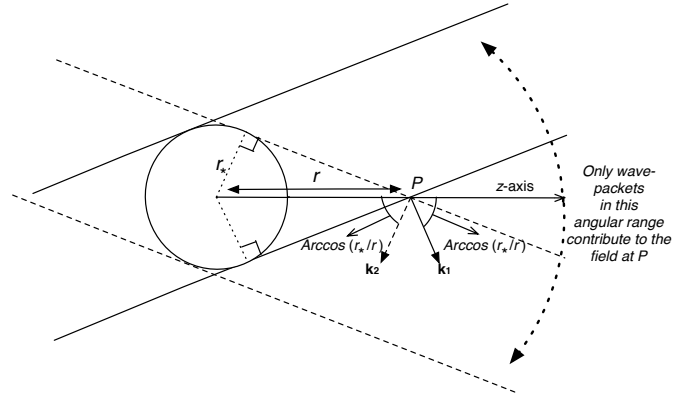
Figure A.1: Here we show that at $t = 0$ when all the wave-packets reach the origin, only wave-packets with direction of momentum in the θ range $-\cos^{-1}(r_*/r) < \theta < \cos^{-1}(r_*/r)$ contribute to the field at a point P on the x-axis at a distance r from the origin. Here $\vec{k}_1$ and $\vec{k}_2$ are the momentum vectors of the two wave-packets shown
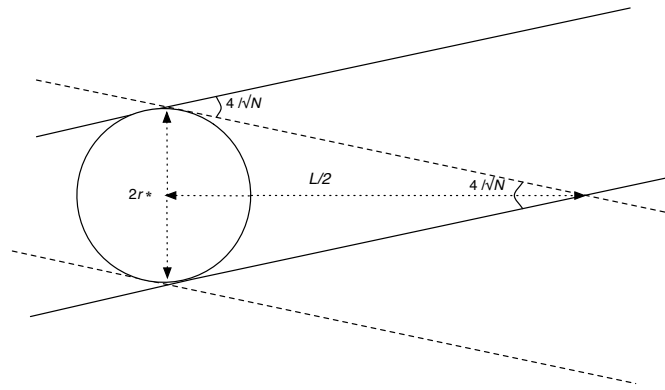
Figure A.2: The distance $L/2$ at which two neighboring wave-packets stop overlapping.

$(2L/\sqrt{N})/(L/2) = 4/\sqrt{N}$. As one can see from Fig. A.2 this would mean that two neighboring wave-packets would stop overlapping at a distance $L/2$ given by,

$$(A.3) \qquad \frac{L}{2} \times \frac{4}{\sqrt{N}} = 2r_* \Rightarrow L = \sqrt{N}r_*.$$

APPENDIX B

Derivation of the Bose-Einstein distribution function

In this Appendix we review the standard textbook derivation of the Bose-Einstein distribution function (for a more detailed treatment see, for instance, Sections 87-89 Ref. [131]). We want to find the distribution function N_ω that maximizes $\Omega(M)$ while respecting the energy conservation constraint,

$$\text{(B.1)} \qquad \int N_\omega g_\omega \omega \ d\omega = M.$$

Remember that N_ω is the number of particles in the energy state with energy ω, and g_ω is the degeneracy of this energy state. Let us represent an arbitrary configuration of a particular energy level as, $\times \times \mid \times \mid ... \times$ where the crosses represent the indistinguishable ϕ quanta and the space between two bars is a quantum state. Thus we should have N_ω crosses and $g_\omega - 1$ bars and the number of ways of arranging these crosses and bars would give us the number of ways of arranging the particles in a particular energy level. Considering all energy levels, this leads to the well known expression,

$$\text{(B.2)} \qquad \Omega(M) = \Pi_\omega \frac{(N_\omega + g_\omega)!}{N_\omega! g_\omega!}$$

where we have approximated $(N_\omega + g_\omega - 1)! \approx (N_\omega + g_\omega)!$ and $(g_\omega - 1)! \approx g_\omega!$. We want to maximize the entropy, $S = \log(\Omega(M))$, respecting the constraints in Eq. (B.1).

We must have,

$$\text{(B.3)} \qquad dS = \sum \log \frac{N_\omega + g_\omega}{g_\omega} dN_\omega = 0$$

$$\text{(B.4)} \qquad dM = \sum \omega dN_\omega = 0.$$

where we have used Stirling's approximation, $\log N! = N \log N - N$. Now we maximize S by using the method of Lagrange multipliers,

$$\text{(B.5)} \qquad dS - \beta dM = 0$$

$$\text{(B.6)} \qquad \Rightarrow \log\left(1 + \frac{g_\omega}{N_\omega}\right) - \beta\omega = 0,$$

where we have used Eqs. (B.3) and (B.4) and β is the Lagrange multiplier. This leads to the Bose-Einstein distribution,

$$\text{(B.7)} \qquad N(\omega)d\omega = \frac{g(\omega)d\omega}{e^{\beta\omega} - 1}.$$

APPENDIX C

Branching ratios in goldstone classicalization

In this Appendix we will provide formulae for the branching ratios of a classicalon to final states with varying number of leptons in the goldstone classicalization model. In the expressions below, w_l is the branching ratio of a W to leptons (e, μ and leptonically decaying τs), w_j is the branching ratio of a W to jets (including hadronically decaying τs), z_l is the branching ratio of a Z to two leptons and z_j is the branching ratio of a Z to two jets. In general we include invisible decays of the Z in z_j. This gives $w_l = 0.25$, $w_j = 0.75$, $z_l = 0.91$ and $z_j = 0.07$. To compute branching ratios to final states with maximum possible number of jets in association with a given number of leptons, we do not include Ws decaying to hadronically decaying τs in w_j and invisibly decaying Zs in z_j, which changes the values of w_j and z_j above to $w_j = 0.68$ and $z_j = 0.71$. The branching ratios depend on the electric charge, Q, of the classicalon. Let us first consider neutral classicalons, i.e. the $Q = 0$ case.

Classicalons with $Q = 0$

In a general configuration for a neutral classicalon there are k W^+W^- pairs and $(N_* - 2k)$ Z-bosons where $0 \leq k \leq [N_*/2]$, $[N_*/2]$ being the largest integer smaller than $N_*/2$. As explained in Section 2.3.1 the probability of having such a configura-

tion is given by,

$$
\begin{aligned}
P'_k &= \frac{N_*!}{(N_* - k)!(k!)^2}, \\
P_k &= \frac{P'_k}{\sum_{k=0}^n P'_k}.
\end{aligned}
$$

(C.1)

In order to obtain the single lepton final state one of the Ws needs to decay leptonically which gives the following branching ratio for a N_*-particle classicalon,

(C.2)
$$
BR(Cl \to l) = \sum_{k=1}^{[N_*/2]} \binom{2k}{1} w_l w_j^{2k-1} z_j^{N_*-2k} P_k.
$$

Similarly to obtain two(three) positive leptons, two (three) W^+s need to decay leptonically which leads to the expressions,

(C.3)
$$
BR(Cl \to l^+ l^+) = \sum_{k=2}^{[N_*/2]} \binom{k}{2} w_l^2 w_j^{2k-2} z_j^{N_*-2k} P_k,
$$

(C.4)
$$
BR(Cl \to 3l^+) = \sum_{k=3}^{[N_*/2]} \binom{k}{3} w_l^3 w_j^{2k-3} z_j^{N_*-2k} P_k.
$$

For the branching ratio to 3 leptons either 3 Ws need to decay leptonically or 2 Ws and a Z need to decay leptonically which gives us two terms in the branching ratio of a classicalon to 3 leptons,

(C.5)
$$
\begin{aligned}
BR(Cl \to 3l) &= \sum_{k=2}^{[N_*/2]} \binom{2k}{3} w_l^3 w_j^{2k-3} z_j^{N_*-2k} P_k \\
&+ \sum_{k=1}^{[N_*/2]} \binom{2k}{1} w_l w_j^{2k-1} \binom{N_* - 2k}{1} z_l z_j^{N_*-2k-1} P_k.
\end{aligned}
$$

Now let us generalize this to a classicalon decay to an arbitrary number of leptons, n_l where $0 \leq n_l \leq 2N_*$. For $n_l = 2p$, an even number, we can get n_l leptons from the decay of an even number, $2q$, of W decays and $(p - q)$, Z decays. This gives us,

(C.6)
$$
BR(Cl \to 2p\, l) = \sum_{q=0}^{p} \sum_{k=q}^{[N_*/2]} \binom{2k}{2q} w_l^{2q} w_j^{2k-2q} \binom{N_* - 2k}{p - q} z_l^{p-q} z_j^{N_*-2k-p+q} P_k.
$$

If $n_l = (2p + 1)$, is an odd number, we can get n_l leptons from the decay of an odd number, $(2q + 1)$, of W decays and $(p - q)$, Z decays. This gives us,

(C.7)
$$BR(Cl \to (2p+1)l) = \sum_{q=0}^{p} \sum_{k=q}^{[N_*/2]} \binom{2k}{2q+1} w_l^{2q+1} w_j^{2k-2q-1} \binom{N_* - 2k}{p - q} z_l^{p-q} z_j^{N_*-2k-p+q} P_k.$$

Classicalons with $Q = +2$

For classicalons with charge $Q = +2$, there are in general $(k + 2)$ W^+ bosons, k W^- bosons and $(N_* - 2k - 2)$ Z-bosons, where $0 \le k \le [(N_* - 2)/2]$, $[(N_* - 2)/2]$ being the largest integer smaller than $(N_* - 2)/2$. Proceeding as in the previous case we obtain the expressions,

$$P_k' = \frac{N_*!}{(N_* - 2k - 2)!k!(k + 2)!},$$

(C.8)
$$P_k = \frac{P_k'}{\sum_{k=0}^{[(N_*-2)/2]} P_k'},$$

(C.9)
$$BR(Cl \to l) = \sum_{k=0}^{[(N_*-2)/2]} \binom{2k + 2}{1} w_l w_j^{2k+1} z_j^{N_*-2k-2} P_k,$$

(C.10)
$$BR(Cl \to l^+ l^+) = \sum_{k=0}^{[(N_*-2)/2]} \binom{k + 2}{2} w_l^2 w_j^{2k} z_j^{N_*-2k-2} P_k,$$

(C.11)
$$BR(Cl \to 3l^+) = \sum_{k=1}^{[(N_*-2)/2]} \binom{k + 2}{3} w_l^3 w_j^{2k-1} z_j^{N_*-2k-2} P_k,$$

$$BR(Cl \to 3l) = \sum_{k=1}^{[(N_* -2)/2]} \binom{2k+2}{3} w_l^3 w_j^{2k-1} z_j^{N_*-2k-2} P_k$$

$$\text{(C.12)} \qquad + \sum_{k=0}^{[(N_* -2)/2]} \binom{2k+2}{1} w_l w_j^{2k+1} \binom{N_* - 2k - 2}{1} z_l z_j^{N_*-2k-3} P_k,$$

$$BR(Cl \to 2p\ ?l) = \sum_{q=0}^{p} \sum_{k=q-1}^{[(N_* -2)/2]} \binom{2k+2}{2q} w_l^{2q} w_j^{2k-2q+2} \times$$

$$\text{(C.13)} \qquad \binom{N_* - 2k - 2}{p - q} z_l^{p-q} z_j^{N_*-2k-2-p+q} P_k,$$

$$BR(Cl \to (2p+1)l) = \sum_{q=0}^{p} \sum_{k=q-1}^{[(N_* -2)/2]} \binom{2k+2}{2q+1} w_l^{2q+1} w_j^{2k-2q+1} \times$$

$$\text{(C.14)} \qquad \binom{N_* - 2k - 2}{p - q} z_l^{p-q} z_j^{N_*-2k-2-p+q} P_k.$$

Classicalons with $Q = -2$

For classicalons with charge $Q = +2$, there are in general $(k+2)$ W^- bosons, k W^+ bosons and $(N_* - 2k - 2)$ Z-bosons, where $0 \le k \le [(N_* - 2)/2]$, $[(N_* - 2)/2]$ being the largest integer smaller than $(N_* - 2)/2$. In this case we obtain,

$$P_k' = \frac{N_*!}{(N_* - 2k - 2)! k! (k+2)!},$$

$$\text{(C.15)} \qquad P_k = \frac{P_k'}{\sum_{k=0}^{[(N_*-2)/2]} P_k'},$$

$$\text{(C.16)} \qquad BR(Cl \to l) = \sum_{k=0}^{[(N_*-2)/2]} \binom{2k+2}{1} w_l w_j^{2k+1} z_j^{N_*-2k-2} P_k,$$

$$\text{(C.17)} \qquad BR(Cl \to l^+ l^+) = \sum_{k=2}^{[(N_*-2)/2]} \binom{k}{2} w_l^2 w_j^{2k} z_j^{N_*-2k-2} P_k,$$

$$\text{(C.18)} \qquad BR(Cl \to 3l^+) = \sum_{k=3}^{[(N_*-2)/2]} \binom{k}{3} w_l^3 w_j^{2k-1} z_j^{N_*-2k-2} P_k,$$

$$BR(Cl \to 3l) = \sum_{k=1}^{[(N_*-2)/2]} \binom{2k+2}{3} w_l^3 w_j^{2k-1} z_j^{N_*-2k-2} P_k$$

$$(C.19) \qquad + \sum_{k=0}^{[(N_*-2)/2]} \binom{2k+2}{1} w_l w_j^{2k+1} \binom{N_* - 2k - 2}{1} z_l z_j^{N_*-2k-3} P_k,$$

$$BR(Cl \to 2p\ ?l) = \sum_{q=0}^{p} \sum_{k=q-1}^{[(N_*-2)/2]} \binom{2k+2}{2q} w_l^{2q} w_j^{2k-2q+2} \times$$

$$(C.20) \qquad \binom{N_* - 2k - 2}{p - q} z_l^{p-q} z_j^{N_*-2k-2-p+q} P_k,$$

$$BR(Cl \to (2p+1)l) = \sum_{q=0}^{p} \sum_{k=q-1}^{[(N_*-2)/2]} \binom{2k+2}{2q+1} w_l^{2q+1} w_j^{2k-2q+1} \times$$

$$(C.21) \qquad \binom{N_* - 2k - 2}{p - q} z_l^{p-q} z_j^{N_*-2k-2-p+q} P_k.$$

APPENDIX D

Statistical definitions for $H \rightarrow WW \rightarrow 2l2\nu$ searches

In this Appendix we review the procedure for evaluating exclusion confidence levels and discovery significances assuming a Gaussian distribution for the expected number of events. For exclusion of a particular value of the mean expected signal S, the hypothesis being tested is the signal plus background hypothesis so that expected number of events, N_{exp}, has the mean value $\bar{N}_{exp} = S + B$. We assume a Poisson distribution for N_{exp} with mean value $S + B$ and standard deviation $\sqrt{S + B}$. If the number of events finally observed in the experiment is $N_{obs} < S + B$ the signal plus background hypothesis is said to be excluded at 95% confidence level if the probability that N_{exp} can fluctuate downward form its mean value $S + B$ to a value less than or equal to N_{obs} is less than 5%. For $S + B \gg 1$ the Poisson distribution we have assumed for N_{exp} tends to a Gaussian distribution and the statement above implies that signal values S, still allowed after setting the 95% CL [1] bound would satisfy,

$$(D.1) \qquad \frac{S + B - N_{obs}}{\sqrt{S + B}} \leq 1.64.$$

To find the median 95 % exclusion potential we take $N_{obs} = B$ to obtain,

$$(D.2) \qquad \frac{S}{\sqrt{S + B}} \leq 1.64.$$

---

[1] Note that 95% CL corresponds to 1.96 standard deviations if both upward and downward fluctuations are considered and 1.64 standard deviations if only downward fluctuations are considered as is the case here.

The upper limit on the allowed signal is the maximum value of S for which this condition holds.

The significance of a discovery, on the other hand, is defined as the significance for rejecting the background-only hypothesis if an excess is seen over the background. We assume a Poisson distribution with mean B and standard deviation $\sqrt{B}$ for the background. The median discovery significance, Z_0 is then the number of standard deviations by which the background must fluctuate upward from its mean value to give an excess equal to the mean expected signal S, that is,

$$(D.3) \qquad Z_0 = \frac{S}{\sqrt{B}}.$$

For a 5σ discovery, for instance, we would have $Z_0 = 5$. The above expression, however, overestimates the significance if the statistics is low. A better approximation for the significance is given by the expression (defined as S_{c12} in [92]),

$$(D.4) \qquad Z_0 = 2(\sqrt{S+B} - \sqrt{B}).$$

This is the definition of significance we will use here.

Systematic uncertainties also play a very important role especially in the $h \to WW \to l\nu l\nu$ channel. The standard way to incorporate systematic effects is by convoluting the Poisson distribution for N_{exp} (which is a Gaussian distribution in the large statistics limit) with the probability density function for the systematic uncertainty. Numerical convolution of the Poisson distribution with a systematic uncertainty having a Gaussian shape with standard deviation ΔB leads to the modification of Eq. (D.2) and Eq. (D.4) to [92],

$$(D.5) \qquad \frac{S}{\sqrt{S + B + (\Delta B)^2}} \leq 1.64 \text{ and,}$$

$$(D.6) \qquad Z_0 = 2(\sqrt{S+B} - \sqrt{B})\sqrt{\frac{B}{B + (\Delta B)^2}}.$$

respectively.

APPENDIX E

$\gamma\gamma\gamma Z,\ \gamma ZZZ$ and $ZZZZ$ couplings

We first consider the operators in the light higgs case in Eq. (5.2) when written in terms of the fields A and Z give rise to $\gamma\gamma\gamma\gamma$, $\gamma\gamma ZZ$, $\gamma\gamma\gamma Z$, γZZZ and $ZZZZ$ couplings. We already wrote the Lagrangian for the $\gamma\gamma\gamma\gamma$ and $\gamma\gamma ZZ$ couplings in Eq. (5.7). In this Appendix we will present the $\gamma\gamma\gamma Z$, γZZZ and $ZZZZ$ couplings. Using Eq. (5.6) we get from Eq. (5.2),

$$
\begin{aligned}
\mathcal{L}_{QNGC}^{\gamma\gamma\gamma Z} &= \frac{a_1^{\gamma\gamma\gamma Z}}{\Lambda^4}F_{\mu\nu}F^{\mu\nu}F_{\rho\sigma}Z^{\rho\sigma} + \frac{a_2^{\gamma\gamma\gamma Z}}{\Lambda^4}F_{\mu\nu}F^{\mu\rho}F_{\rho\sigma}Z^{\sigma\nu} \\
\mathcal{L}_{QNGC}^{\gamma ZZZ} &= \frac{a_1^{\gamma ZZZ}}{\Lambda^4}\frac{m_Z^2}{2}F_{\mu\nu}Z^{\mu\nu}Z_\rho Z^\rho + \frac{a_2^{\gamma ZZZ}}{\Lambda^4}\frac{m_Z^2}{2}F_{\mu\nu}Z^{\mu\rho}Z_\rho Z^\nu \\
&\quad + \frac{a_3^{\gamma ZZZ}}{\Lambda^4}F_{\mu\nu}Z^{\mu\nu}Z_{\rho\sigma}Z^{\rho\sigma} + \frac{a_4^{\gamma ZZZ}}{\Lambda^4}F_{\mu\nu}Z^{\mu\rho}Z_{\rho\sigma}Z^{\sigma\nu} \\
\mathcal{L}_{QNGC}^{ZZZZ} &= \frac{a_1^{ZZZZ}}{\Lambda^4}\frac{m_Z^4}{4}Z_\mu Z^\mu Z_\rho Z^\rho + \frac{a_2^{ZZZZ}}{\Lambda^4}\frac{m_Z^2}{2}Z_{\mu\nu}Z^{\mu\nu}Z_\rho Z^\rho \\
&\quad + \frac{a_4^{ZZZZ}}{\Lambda^4}Z_{\mu\nu}Z^{\mu\nu}Z_{\rho\sigma}Z^{\rho\sigma} + \frac{a_5^{ZZZZ}}{\Lambda^4}Z_{\mu\nu}Z^{\mu\rho}Z_{\rho\sigma}Z^{\sigma\nu}
\end{aligned}
$$

(E.1)

where for the $\gamma\gamma\gamma Z$ couplings we get,

$$
a_1^{\gamma\gamma\gamma Z} = -4s_w c_w^3 c_8 + 4s_w^3 c_w(c_9 + c_{10}) + (2s_w c_w^3 - 2s_w^3 c_w)(c_{11} + c_{12})
$$

(E.2) $\quad a_2^{\gamma\gamma\gamma Z} = -4s_w c_w^3 c_{13} + 4s_w^3 c_w(c_{14} + c_{15}) + (2s_w c_w^3 - 2s_w^3 c_w)(c_{16} + c_{17}),$

for the γZZZ couplings we get,

$$a_1^{\gamma ZZZ} = -2s_w c_w c_3 + 2s_w c_w c_4 - (c_w^2 - s_w^2)c_5$$

$$a_2^{\gamma ZZZ} = -2s_w c_w c_6 + 2s_w c_w c_7$$

$$a_3^{\gamma ZZZ} = -4s_w^3 c_w c_8 + 4s_w c_w^3 (c_9 + c_{10}) + (2s_w^3 c_w - 2s_w c_w^3)(c_{11} + c_{12})$$

$$\text{(E.3)} \quad a_4^{\gamma ZZZ} = -4s_w^3 c_w c_{13} + 4s_w c_w^3 (c_{14} + c_{15}) + (2s_w^3 c_w - 2s_w c_w^3)(c_{16} + c_{17}).$$

and for the $ZZZZ$ couplings we get,

$$a_1^{ZZZZ} = c_1 + c_2$$

$$a_2^{ZZZZ} = s_w^2 c_3 + c_w^2 c_4 + c_w s_w c_5$$

$$a_3^{ZZZZ} = s_w^2 c_6 + c_w^2 c_7$$

$$a_4^{ZZZZ} = s_w^4 c_8 + c_w^4 (c_9 + c_{10}) + c_w^2 s_w^2 (c_{11} + c_{12})$$

$$\text{(E.4)} \quad a_5^{ZZZZ} = s_w^4 c_{13} + c_w^4 (c_{14} + c_{15}) + c_w^2 s_w^2 (c_{16} + c_{17}).$$

As explained in Section 5.2.2, any $U(1)_{em}$ invariant operator, constructed using Z_μ and $F_{\mu\nu}$ fields, is an allowed operator in the higgsless case. Thus, for the higgsless case we will get the same operators as above but now $\mathcal{O}_1^{ZZZZ}$ would arise from dimension 4 operators while $\mathcal{O}_1^{\gamma ZZZ}$, $\mathcal{O}_2^{\gamma ZZZ}$, $\mathcal{O}_2^{ZZZZ}$ and $\mathcal{O}_3^{ZZZZ}$ would arise from dimension 6 operators.

APPENDIX F

Derivation of unitarity relation for the $\gamma\gamma \to \gamma\gamma$ and $\gamma\gamma \to ZZ$ processes

In this Appendix we derive the expression for the unitarity bound for the processes $\gamma\gamma \to \gamma\gamma$ and $\gamma\gamma \to ZZ$. Applying the optical theorem to the $\gamma\gamma \to \gamma\gamma$ process tells us,

$$
\begin{aligned}
\frac{\text{Im}(\mathcal{M}(\gamma_1\gamma_2 \to \gamma_1\gamma_2))}{s} &= \sigma(\gamma_1\gamma_2 \to \text{everything}) \\
&= \sigma(\gamma_1\gamma_2 \to \gamma(\epsilon_1)\gamma(\epsilon_2)) + \sum_{\epsilon_3,\epsilon_4} \sigma(\gamma_1\gamma_2 \to Z(\epsilon_3)Z(\epsilon_4)) \\
&\quad + \Delta
\end{aligned}
$$
(F.1)

where γ_i denotes $\gamma(k_i, \epsilon_i)$ and Δ is a positive number that accounts for all the other contributions to the RHS of Eq.. (F.1) and the cross section for the $\gamma\gamma \to VV$ process is given by,

$$
\sigma = \frac{\beta_W}{64\pi^2 s} \int d\Omega_{\text{CM}} \, |\mathcal{M}(\gamma_1\gamma_2 \to VV)|^2.
$$
(F.2)

The amplitude can be expanded into partial waves as follows,

$$
\begin{aligned}
\mathcal{M}(\gamma_1\gamma_2 \to \gamma_1\gamma_2) &= 16\pi \sum_J (2J+1)b_J P_J(\cos\theta) \\
\mathcal{M}(\gamma_1\gamma_2 \to ZZ) &= 16\pi \sum_J (2J+1)a_J P_J(\cos\theta).
\end{aligned}
$$
(F.3)

where $\beta_V = \sqrt{1 - \frac{4M_V^2}{s}}$. For the forward scattering in the LHS of Eq. (F.1), we must put $\theta = 0$. Using Eqs. (F.1-F.3) and the following property of Legendre polynomials,

$$(F.4) \qquad \int_{-1}^{1} P_m(x) P_n(x) = \frac{2}{2n+1} \delta_{mn},$$

gives,

$$(F.5) \qquad (\,\mathrm{Im}(b_l))^2 - \mathrm{Im}(b_l) + \sum_{\epsilon_3, \epsilon_4} (\mathrm{Re}(b_l))^2 + \beta_W \sum_{\epsilon_3, \epsilon_4} |a_l|^2 + \delta_l = 0.$$

The first two terms in Eq. (F.5) should be evaluated taking the initial polarizations to be exactly same as the final polarizations, and δ_l is the positive contribution from every other source. Eq. (F.5) is a quadratic equation for $\mathrm{Im}(b_l)$. The equation must have real roots and thus must have a positive discriminant. This gives the condition,

$$(F.6) \qquad (\mathrm{Re}(b_l))^2 + \beta \sum_{\epsilon_3, \epsilon_4} |a_l|^2 + \delta_l < \frac{1}{4}.$$

APPENDIX G

Kinematic bound on photon virtuality

First let us derive the kinematical limits on q_i^2. From conservation laws we must have $q = (E - E_i', \vec{p} - \vec{p_i})$. Substituting $|\vec{p_i'}| = \sqrt{E_i^2 - m^2}$, m being the mass of the particle emitting the photon, we obtain for $m \ll E_i'$,

$$\text{(G.1)} \qquad q_i^2 = -4EE_i' \sin^2 \frac{\theta_i}{2} - \frac{m^2 \omega_i^2}{EE_i} \cos \theta_i.$$

Here θ_i is the angle between $\vec{p}$ and $\vec{p_i'}$. In the expression above the first term dominates. As most of the contribution to the amplitude comes from the small $|q_i^2|$ region, ignoring the second term above we see that we must have small θ. We thus obtain the following kinematical bound on q_i^2,

$$\text{(G.2)} \qquad q_i^2 < -\frac{m^2 \omega_i^2}{E(E - \omega_i)}.$$

BIBLIOGRAPHY

BIBLIOGRAPHY

[1] ATLAS Collaboration, ATL-PHYS-PUB-2010-015 (November 2010).

[2] ALEPH Collaboration, DELPHI Collaboration, L3 Collaboration, OPAL Collaborations, LEP Working Group for Higgs Boson Searches, S. Schael *et al.*, Eur.Phys.J. **C47**, 547 (2006), hep-ex/0602042.

[3] E. Lunghi and A. Soni, JHEP **0709**, 053 (2007), 0707.0212.

[4] B. W. Lee, C. Quigg, and H. Thacker, Phys.Rev. **D16**, 1519 (1977).

[5] A. Falkowski, C. Grojean, A. Kaminska, S. Pokorski, and A. Weiler, JHEP **1111**, 028 (2011), 1108.1183.

[6] R. Contino, (2010), 1005.4269.

[7] M. S. Chanowitz and M. K. Gaillard, Nucl.Phys. **B261**, 379 (1985).

[8] J. F. Gunion, H. E. Haber, G. L. Kane, and S. Dawson, Front.Phys. **80**, 1 (2000).

[9] J. D. Wells, (2009), 0909.4541.

[10] C. Grojean, Phys.Usp. **50**, 1 (2007).

[11] LEP Working Group for Higgs boson searches, ALEPH Collaboration, DELPHI Collaboration, L3 Collaboration, OPAL Collaboration, R. Barate *et al.*, Phys.Lett. **B565**, 61 (2003), hep-ex/0306033.

[12] TEVNPH (Tevatron New Phenomina and Higgs Working Group), CDF Collaboration, D0 Collaboration, (2012), 1203.3774, Preliminary results prepared for the Winter 2012 Conferences.

[13] ATLAS Collaboration, ATLAS-CONF-2012-019 (2012).

[14] CMS Collaboration, CMS-PAS-HIG-12-008 (2012).

[15] See the website http://gfitter.desy.de.

[16] M. E. Peskin and J. D. Wells, Phys.Rev. **D64**, 093003 (2001), hep-ph/0101342.

[17] A. J. Barr, B. Gripaios, and C. G. Lester, JHEP **0907**, 072 (2009), 0902.4864.

[18] G. Dvali, G. F. Giudice, C. Gomez, and A. Kehagias, JHEP **1108**, 108 (2011), 1010.1415.

[19] C. Grojean and R. S. Gupta, (2011), 1110.5317.

[20] R. S. Gupta and J. D. Wells, Phys.Rev. **D81**, 055012 (2010), 0912.0267.

[21] R. S. Gupta and J. D. Wells, (2011), 1110.0824.

[22] R. S. Gupta, Phys.Rev. **D85**, 014006 (2012), 1111.3354, 37 pages, 6 figures.

[23] G. Dvali and D. Pirtskhalava, Phys.Lett. **B699**, 78 (2011), 1011.0114.

[24] G. Dvali, (2011), 1101.2661.

[25] G. Dvali, C. Gomez, and A. Kehagias, JHEP **1111**, 070 (2011), 1103.5963.

[26] B. Bajc, A. Momen, and G. Senjanovic, (2011), 1102.3679.

[27] R. Akhoury, S. Mukohyama, and R. Saotome, (2011), 1109.3820.

[28] N. Brouzakis, J. Rizos, and N. Tetradis, Phys.Lett. **B708**, 170 (2012), 1109.6174.

[29] W. Greiner, L. Neise, and H. Stocker, p. 153 (1997), Thermodynamics and Statistical Mechanics.

[30] I. Antoniadis, N. Arkani-Hamed, S. Dimopoulos, and G. Dvali, Phys.Lett. **B436**, 257 (1998), hep-ph/9804398.

[31] G. Dvali, G. Gabadadze, M. Kolanovic, and F. Nitti, Phys.Rev. **D65**, 024031 (2002), hep-th/0106058.

[32] S. B. Giddings and S. D. Thomas, Phys.Rev. **D65**, 056010 (2002), hep-ph/0106219.

[33] S. Dimopoulos and G. L. Landsberg, Phys.Rev.Lett. **87**, 161602 (2001), hep-ph/0106295.

[34] G. F. Giudice, R. Rattazzi, and J. D. Wells, Nucl.Phys. **B630**, 293 (2002), hep-ph/0112161.

[35] W. Stirling, E. Vryonidou, and J. Wells, Eur.Phys.J. **C71**, 1642 (2011), 1102.3844.

[36] P. Meade and L. Randall, JHEP **0805**, 003 (2008), 0708.3017.

[37] G. Dvali, C. Gomez, and S. Mukhanov, (2011), 1106.5894.

[38] R. Barbieri, A. Pomarol, R. Rattazzi, and A. Strumia, Nucl.Phys. **B703**, 127 (2004), hep-ph/0405040.

[39] S. Dutta, K. Hagiwara, Q.-S. Yan, and K. Yoshida, Nucl.Phys. **B790**, 111 (2008), 0705.2277.

[40] CMS collaboration,CMS-PAS-EXO-11-071 (2011).

[41] Particle Data Group, K. Nakamura *et al.*, J.Phys.G **G37**, 075021 (2010).

[42] S. Dawson, Nucl.Phys. **B249**, 42 (1985).

[43] A. Martin, W. Stirling, R. Thorne, and G. Watt, Eur.Phys.J. **C63**, 189 (2009), 0901.0002.

[44] J. A. Evans and M. A. Luty, Phys.Rev.Lett. **103**, 101801 (2009), 0904.2182.

[45] B. Mukhopadhyaya and S. Mukhopadhyay, Phys.Rev. **D82**, 031501 (2010), 1005.3051.

[46] M. Lisanti, P. Schuster, M. Strassler, and N. Toro, (2011), 1107.5055.

[47] R. Contino and G. Servant, JHEP **0806**, 026 (2008), 0801.1679.

[48] G. Dissertori, E. Furlan, F. Moortgat, and P. Nef, JHEP **1009**, 019 (2010), 1005.4414.

[49] ATLAS Collaboration, G. Aad *et al.*, (2009), 0901.0512.

[50] A. Pukhov, (2004), hep-ph/0412191.

[51] M. Ambroso, V. Braun, and B. A. Ovrut, JHEP **0810**, 046 (2008), 0807.3319.

[52] S. Abel and C. Munoz, JHEP **0302**, 010 (2003), hep-ph/0212258.

[53] A. Aranda and M. Sher, Phys.Rev. **D62**, 092002 (2000), hep-ph/0005113.

[54] D. Atwood, L. Reina, and A. Soni, Phys.Rev. **D55**, 3156 (1997), hep-ph/9609279.

[55] C. Amsler *et al.*, Phys. Lett. B **1**, 667.

[56] V. Lubicz *et al.*, Nucl.Phys. Proc. Suppl. **43**, 163.

[57] T. Cheng and M. Sher, Phys.Rev. **D35**, 3484 (1987).

[58] P. Ball and R. Fleischer, Eur.Phys.J. **C48**, 413 (2006), hep-ph/0604249.

[59] A. S. Joshipura and B. P. Kodrani, Phys.Rev. **D81**, 035013 (2010), 0909.0863.

[60] CDF Collaboration, T. Aaltonen *et al.*, Phys.Rev.Lett. **100**, 101802 (2008), 0712.1708.

[61] LHCb Collaboration, M.-O. Bettler, PoS **FPCP2009**, 056 (2009), 0908.4066.

[62] F. Mahmoudi and O. Stal, Phys.Rev. **D81**, 035016 (2010), 0907.1791.

[63] S. L. Glashow and S. Weinberg, Phys.Rev. **D15**, 1958 (1977).

[64] S. Su and B. Thomas, Phys.Rev. **D79**, 095014 (2009), 0903.0667.

[65] K. Babu and C. F. Kolda, Phys.Rev.Lett. **84**, 228 (2000), hep-ph/9909476.

[66] L. Brucher and R. Santos, Eur.Phys.J. **C12**, 87 (2000), hep-ph/9907434.

[67] P. Ferreira, R. Santos, and A. Barroso, Phys.Lett. **B603**, 219 (2004), hep-ph/0406231.

[68] J. F. Gunion and H. E. Haber, Phys.Rev. **D67**, 075019 (2003), hep-ph/0207010.

[69] J. Diaz-Cruz and A. Mendez, Nucl.Phys. **B380**, 39 (1992).

[70] A. Barroso, P. Ferreira, and R. Santos, Phys.Lett. **B652**, 181 (2007), hep-ph/0702098.

[71] V. D. Barger, J. Hewett, and R. Phillips, Phys.Rev. **D41**, 3421 (1990).

[72] Heavy Flavor Averaging Group (HFAG) Collaboration, E. Barberio *et al.*, (2007), 0704.3575.

[73] M. Misiak *et al.*, Phys.Rev.Lett. **98**, 022002 (2007), hep-ph/0609232.

[74] S. de Visscher, J.-M. Gerard, M. Herquet, V. Lemaitre, and F. Maltoni, JHEP **0908**, 042 (2009), 0904.0705.

[75] S. Bertolini, Nucl.Phys. **B272**, 77 (1986).

[76] DELPHI Collaboration, J. Abdallah *et al.*, Eur.Phys.J. **C38**, 1 (2004), hep-ex/0410017.

[77] DELPHI Collaboration, J. Abdallah *et al.*, Eur.Phys.J. **C34**, 399 (2004), hep-ex/0404012.

[78] CDF Collaboration, CDF Note 9322 (2008).

[79] V. D. Barger, M. Berger, and P. Ohmann, Phys.Rev. **D47**, 1093 (1993), hep-ph/9209232.

[80] W. Grimus and L. Lavoura, Eur.Phys.J. **C39**, 219 (2005), hep-ph/0409231.

[81] C. F. Kolda, (1995), Ph.D. Thesis.

[82] H. Baer, J. Ferrandis, K. Melnikov, and X. Tata, Phys.Rev. **D66**, 074007 (2002), hep-ph/0207126.

[83] A. Barroso, L. Brucher, and R. Santos, Phys.Rev. **D60**, 035005 (1999), hep-ph/9901293.

[84] J. Alwall *et al.*, JHEP **0709**, 028 (2007), 0706.2334.

[85] E. Richter-Was, Acta Phys.Polon. **B31**, 1973 (2000).

[86] K. Cheung, J. Song, and Q.-S. Yan, Phys.Rev.Lett. **99**, 031801 (2007), hep-ph/0703149.

[87] M. Carena, T. Han, G.-Y. Huang, and C. E. Wagner, JHEP **0804**, 092 (2008), 0712.2466.

[88] M. J. Strassler and K. M. Zurek, Phys.Lett. **B651**, 374 (2007), hep-ph/0604261.

[89] R. Schabinger and J. D. Wells, Phys.Rev. **D72**, 093007 (2005), hep-ph/0509209.

[90] M. Bowen, Y. Cui, and J. D. Wells, JHEP **0703**, 036 (2007), hep-ph/0701035.

[91] ATLAS Collaboration, ATL-PHYS-PUB-2010-005 (June 2010).

[92] CMS Collaboration, G. Bayatian *et al.*, J.Phys.G **G34**, 995 (2007).

[93] See talk given by Aaron Armbuster at Higgs Hunting 2011 (http://is.gd/bSq8Hz).

[94] ATLAS Collaboration, G. Aad *et al.*, Eur.Phys.J. **C71**, 1728 (2011), 1106.2748.

[95] ATLAS Collaboration, G. Aad *et al.*, (2011), 1112.2577.

[96] A. J. Barr, B. Gripaios, and C. G. Lester, Phys.Rev.Lett. **108**, 041803 (2012), 1108.3468.

[97] CMS Collaboration, CMS-PAS-HIG-11-014. 2011.

[98] W. Buchmuller and D. Wyler, Nucl.Phys. **B268**, 621 (1986).

[99] FP420 R and D Collaboration, M. Albrow *et al.*, JINST **4**, T10001 (2009), 0806.0302.

[100] P. Dervan, A. Signer, W. Stirling, and A. Werthenbach, J.Phys.G **G26**, 607 (2000), hep-ph/0002175.

[101] O. J. Eboli, M. Gonzalez-Garcia, S. Lietti, and S. Novaes, Phys.Rev. **D63**, 075008 (2001), hep-ph/0009262.

[102] T. Pierzchala and K. Piotrzkowski, Nucl.Phys.Proc.Suppl. **179-180**, 257 (2008), 0807.1121.

[103] E. Chapon, C. Royon, and O. Kepka, Phys.Rev. **D81**, 074003 (2010), 0912.5161.

[104] E. Chapon, C. Royon, and O. Kepka, (2009), 0908.1061.

[105] C. Burgess and D. London, Phys.Rev. **D48**, 4337 (1993), hep-ph/9203216.

[106] G. F. Giudice, R. Rattazzi, and J. D. Wells, Nucl.Phys. **B544**, 3 (1999), hep-ph/9811291.

[107] G. F. Giudice and A. Strumia, Nucl.Phys. **B663**, 377 (2003), hep-ph/0301232.

[108] V. Khoze, A. Martin, and M. Ryskin, Eur.Phys.J. **C23**, 311 (2002), hep-ph/0111078.

[109] OPAL Collaboration, G. Abbiendi *et al.*, Phys.Rev. **D70**, 032005 (2004), hep-ex/0402021.

[110] R. Franceschini, P. P. Giardino, G. F. Giudice, P. Lodone, and A. Strumia, JHEP **1105**, 092 (2011), 1101.4919.

[111] CMS collaboration,CMS PAS EXO-11-038 (August 2011).

[112] Z. Han and W. Skiba, Phys.Rev. **D71**, 075009 (2005), hep-ph/0412166.

[113] F. Close, S. Donnachie, and G. Shaw, (2007), Electromagnetic interactions and hadronic structure.

[114] V. Budnev, I. Ginzburg, G. Meledin, and V. Serbo, Phys.Rept. **15**, 181 (1975).

[115] J. de Favereau, X. Rouby, and K. Piotrzkowski, JINST **2**, P09005 (2007), 0707.1198.

[116] B. Cox, F. Loebinger, and A. Pilkington, JHEP **0710**, 090 (2007), 0709.3035.

[117] M. Boonekamp *et al.*, (2011), 1102.2531.

[118] G. Ingelman and P. Schlein, Phys.Lett. **B152**, 256 (1985).

[119] M. Albrow, T. Coughlin, and J. Forshaw, Prog.Part.Nucl.Phys. **65**, 149 (2010), 1006.1289.

[120] V. Khoze, A. Martin, and M. Ryskin, Phys.Lett. **B650**, 41 (2007), hep-ph/0702213.

[121] E. Glover and J. van der Bij, Phys.Lett. **B219**, 488 (1989).

[122] E. Gotsman, E. Levin, U. Maor, and J. Miller, (2009), 0903.0247.

[123] G. Jikia, Phys.Lett. **B298**, 224 (1993).

[124] I. Antoniadis, A. Boyarsky, S. Espahbodi, O. Ruchayskiy, and J. D. Wells, Nucl.Phys. **B824**, 296 (2010), 0901.0639.

[125] G. Jikia and A. Tkabladze, Phys.Lett. **B323**, 453 (1994), hep-ph/9312228.

[126] S. Atag, S. Inan, and I. Sahin, JHEP **1009**, 042 (2010), 1005.4792.

[127] M. Boonekamp and T. Kucs, Comput.Phys.Commun. **167**, 217 (2005), hep-ph/0312273.

[128] See http://boonekam.home.cern.ch/boonekam/dpemc.htm.

[129] A. Manohar and H. Georgi, Nucl.Phys. **B234**, 189 (1984).

[130] G. Giudice, C. Grojean, A. Pomarol, and R. Rattazzi, JHEP **0706**, 045 (2007), hep-ph/0703164.

[131] R. C. Tolman, (1979), The Principles of Statistical Mechanics.